DEVELOPMENT AND TESTING OF A LAB-IN-A-TUBE BIOSENSOR

DEVELOPMENT AND TESTING OF A LAB-IN-A-TUBE BIOSENSOR

By JONATHAN L'HEUREUX-HACHÉ, B.Eng.

A Thesis Submitted to the School of Graduate Studies in Partial Fulfilment of the Requirements for the degree Master of Applied Science in Biomedical Engineering

McMaster University © Copyright by Jonathan L'Heureux-Haché, April 2023

McMaster University MASTER OF SCIENCE (2023) Hamilton, Ontario (Biomedical Engineering)

TITLE: Development and Testing of a Lab-In-A-Tube Biosensor

AUTHOR: Jonathan L'Heureux-Haché, B. Eng (University of Victoria)

SUPERVISOR: Professor Leyla Soleymani

NUMBER OF PAGES: xv, 96

Lay abstract

Early detection is critical for timely treatment and better patient outcomes. Point-of-care (POC) biosensors allow for disease diagnosis and real-time monitoring of a patient's health status directly at the patient's bedside without the need for expensive equipment or specialized personnel. A lab-in-a-tube biosensor was developed using sensing surfaces on low-cost plastic that is rolled and heat-shrunk into miniaturized tubing for analysis of liquid samples. The wrinkled sensing surface that results from heat-shrinking dramatically increase surface area and interaction with the sample, enabling sensitive detection that is fast and quantitative. These devices are capable of capturing samples at high flow rates, allowing for rapid analysis of large samples. Overall, this work demonstrates the successful creation of a biosensor platform that could be incorporated with existing medical tubing for POC diagnostics.

Abstract

Early detection is crucial in delivering timely treatment and improving patient outcomes. Point-of-care (POC) biosensors play an essential role in early detection, allowing for rapid and accurate diagnosis of diseases at the patient's bedside without the need for expensive equipment or specialized personnel. By performing the analysis on-site, POC diagnostics can offer continuous monitoring and real-time data acquisition of a patient's health status. Thus, there is strong incentive in creating POC biosensors to provide healthcare professionals with greater access to diagnostic information, ultimately improving outcomes and reducing healthcare costs.

Herein, the development of a POC lab-in-a-tube biosensor that utilizes simple and scalable fabrication techniques is presented. Electrodes are patterned on low-cost plastic substrates, which can be subsequently rolled and heat-shrunk into miniaturized tubing for flow-through analysis of liquid samples. Heat-shrinking of the device results in 3-dimensional, hierarchically wrinkled electrodes with morphological feature that span several orders of magnitude in size. These wrinkled electrodes demonstrate dramatically increased surface area in a given footprint compared to traditional planar electrodes. Incorporation of modified gold and silver wires allows for sensitive and stable electrochemical detection, enabling fast and quantitative results. These devices are capable of millilitre-per-minute flow rates to allow for rapid sample processing and for increased mass-transport to the electrode surface. The ability to capture analytes was characterized with nucleic acid sequences using pump-driven and blood-collection tube induced flow for rapid and accurate detection.

Overall, this work demonstrates the successful development of an electrochemical platform integrated into a plastic tubing capable of rapid detection of flowing analytes. With its ease-of-use and compatibility with a wide range of flow rates, the device has the potential to be incorporated with existing medical tubing and procedures to achieve POC diagnostics.

Acknowledgements

I would like to express my deep gratitude to my supervisor Dr. Leyla Soleymani for her guidance, support, and patience throughout my studies. Her encouragement, insightful comments, and constructive criticism were invaluable in shaping my research.

I would like to thank the members of my supervisory committee, Dr. Ali Ashkar, and Dr. Boyang Zhang for their valuable feedback and suggestions.

Additionally, I am grateful for the faculty members and administrative staff of the McMaster School of Biomedical Engineering for providing support throughout my academic journey. I also thank the Centre of Emerging Device Technologies for their facilities and expertise. I am thankful for the financial support provided to me by McMaster University that enabled me to pursue my graduate studies.

I wholeheartedly thank the fellow members of the Soleymani lab, past and present, for their incredible support and the many lasting memories shared together. Additional praise must be given to Roderick MacLachlan for his influence on nearly all aspects of the project.

I want to thank my family and friends for their unwavering support, and encouragement throughout my master's studies. And lastly to my partner, Ana Portillo, my deepest gratitude for always believing in me, being the source of constant encouragement, keeping my sanity and being the driving force behind my success.

Table of Contents

List of Figures

List of Tables

List of Abbreviations

Ag/AgCl	Silver-Silver Chloride (reference electrode)
Au	Gold
CE	Counter Electrode
DI	Deionized (water)
DNA	Deoxyribonucleic Acid
Fc	Ferrocene
H_2SO_4	Sulfuric Acid
KCl	Potassium Chloride
LIT	Lab-In-a-Tube
MCH	6-Mercapto-1-Hexanol
MB	Methylene Blue
NaCl	Sodium Chloride
PB	Phosphate Buffer
PBS	Phosphate Buffered Saline
PDMS	Polydimethylsiloxane
PO	Polyolefin
POC	Point-Of-Care
Pt	Platinum
RE	Reference Electrode
RSD	Relative Standard Deviation
SCE	Saturated Calomel Electrode
SEM	Scanning Electron Microscopy
SHE	Standard Hydrogen Electrode
ssDNA	Single-Stranded Deoxyribonucleic Acid
SWV	Square Wave Voltammetry
WE	Working Electrode

Declaration of Academic Achievement

The work described in this thesis has consisted solely of my own contributions, with guidance from Dr. Leyla Soleymani, other than the following exception:

Roderick MacLachlan provided scanning electron microscopy images and led the acquisition and analysis of contact angle measurements.

1 Introduction

1.1 Context

1.1.1 Biosensors

The medical field has experienced significant improvements owing to advances in technology and a deeper understanding of the biological mechanisms that control health and disease. One such area aiming to revolutionize medical care is the development of biosensors by combining these facets into standalone detection devices.

Without reliable diagnostic tests that correctly identify a disease or illness, medical decisions lack critical information needed for optimal patient care. Such cases could lead to misdiagnosis or inappropriate treatments, ultimately putting the patient's health and life at risk [1]. Medical diagnostic tests have traditionally been carried out in laboratories or other dedicated healthcare settings, where patient samples such as blood or urine can be analyzed by trained personnel. Many of these laboratory-based tests rely on labour-intensive techniques such as microscopy, immunoassays, and cell or bacterial cultures which can take multiple days for a result [2].

Biosensors are devices that integrate biorecognition elements with a signal transducer to generate a signal proportional to a biological or chemical reactions of interest [3]. These devices can be used to assess various health conditions, such as blood glucose levels in diabetic patients, or cardiac markers and heart activity in individuals with cardiovascular disease [4]. The range of their applications within healthcare is continually expanding to encompass areas such as diagnostics, therapy, and monitoring. Furthermore, their use in other settings such as in drug development, food-safety, and environmental monitoring is expanding [5].

One of the primary advantages of biosensors over traditional, laboratory-based methods is the ability to reduce the need for skilled operators and the use of sophisticated laboratory equipment and reduce the sample-to-result time [6]. Efforts in miniaturization and cost and time reduction allow the sensors to be employed directly at the patient's bedside to produce Point-Of-Care (POC) biosensors.

1.1.2 Point-Of-Care diagnostics

Development of POC biosensors is particularly attractive for improving clinical outcomes as it drastically improves the amount of information available at the time needed to make healthcare decisions. These devices allow for rapid and simple detection, improved monitoring potential, cost savings, and improved access to healthcare [7].

POC biosensors aim to provide the rapid and convenient diagnosis of a wide variety of medical conditions through efforts in being user-friendly, portable, and producing results within minutes [8]. These factors allow for healthcare decisions to be made on-location and can remove the need for the patient or the collected sample to travel to a healthcare facility or centralized lab. POC biosensors can enable the real-time monitoring of patients, providing early warning of deteriorating conditions and allowing immediate intervention – crucial for improving clinical outcome [9].

1.1.3 Microfluidics & Lab-on-a-chip

The use of microfluidics – systems that interact with fluids at the micrometer scale – is of huge interest to researchers wanting to create the next generation of POC biosensors [10]. The benefits of microfluidics range from the ability to analyze sub microliter sample volumes, reducing sample preparation steps through automation, to shortening the time required to obtain a diagnosis [11]. Combination of microfluidics with biosensors also allows for multiplexed sample analysis, improved portability, and can facilitate the creation of low-cost, single-use devices for POC diagnostics [11]. Utilizing the physics of liquids at the small scale can improve sensitivity and specificity of POC biosensors [12]. For example, the use of flow confinement and controlled mixing can reduce the size of the diffusion layer, increasing the binding rate of molecules of interest to the capture surfaces, resulting in improved detection limits and better response times [13], [14].

1.1.4 Challenges

Despite the great advantages offered by POC biosensors, comparatively few have been used in practise thus far [4]. Certain POC devices such as the pregnancy test and glucose meter have seen

widescale success, however many biosensors reported in literature face difficulties in translating academic results into a commercially available device [3][15].

In order to address to hurdles faced in POC biosensor development, the World Health Organization (WHO) has established the ASSURED acronym [6], [16]. The acronym stands for: **A**ffordable, **S**ensitive, **S**pecific, **U**ser-friendly, **R**apid & robust, **E**quipment-free, **D**elivered. The ASSURED acronym provides a useful framework for the design of diagnostic tests, and by ensuring that these criteria are met, the effectiveness and accessibility of POC testing is greatly improved. An important consideration of the ASSURED acronym is that diagnostic requirements vary with the testing location and shape the technical approaches that can be used [6]. A biosensor that is to be used by an individual at home will face different design challenges than one destined to be used in a healthcare setting [17]. Each of these environments vary in available resources and personnel that ultimately permit different biosensor design criteria and sophistication.

Newly developed POC biosensors must be sufficiently affordable to be utilized in a healthcare setting as single use devices or feature disposable components [18]. Device performance criteria such as sensitivity or ease-of-use are only some facets of POC device development, and monetary aspects such as manufacturing costs, price of reagents, and long-term storage conditions must be considered to allow for widescale adoption [19]. A successful biosensor is one that achieves sufficient performance for the task while remaining economical, such that it becomes the clear choice when reaching for a diagnostic test [20].

A frequent hurdle faced when developing diagnostic tools is achieving appropriate sensitivity while ensuring that assay complexity and test duration are not significantly impacted [1]. Generally, a diagnostic techniques' sensitivity is inversely proportional to its cost, time to obtain a result, and complexity as a function of equipment required [21]. A test must be able to provide results at a clinically relevant level for the target concentration. Furthermore, repeatability of the system must be sufficient to allow for confidence in the result.

Sample processing remains a serious roadblock to achieving POC biosensors, particularly when using clinically relevant samples [22]. Complex solutions derived from patients such as blood,

urine and saliva are frequently used for analysis; however, contain many complex molecules that can interfere with detection. These samples contain unwanted proteins and cells that can negatively interact with device surfaces such as through non-specific adsorption preventing binding of the target analyte or the generation of non-specific signals [23], [24]. Separation of media using filters or centrifugation, addition of reagents to control the viscosity or pH, and many other sample processing steps are commonly employed by trained personnel prior to further analysis [25]. Additional challenges are faced when eliminating intermediate manipulation steps of traditional assays. Tasks like mixing, reagent addition, and sample separation can introduce variation dependent on the user [26]. It is therefore paramount to minimize manual sample processing to achieve true POC biosensors.

Despite current limitations, improvements in the development POC biosensors can enable their adoption and complement traditional laboratory-based diagnostic methods. Ultimately, POC biosensors have the potential to greatly improve healthcare delivery and patient outcomes through personalized, near real-time data about their health status and helping clinicians in making informed decisions about diagnosis and treatment.

1.2 Motivation and approach

The motivation for this research is to increase the amount of information available when making healthcare decisions by developing a rapid, accurate, convenient, and cost-effective biosensing technology that can be used in a variety of diagnostic applications in the future. Focus was placed on developing a simple device that could easily be incorporated into existing medical procedures. We believe that by utilizing flow, manual interactions and the use of additional reagents could be reduced, and combined with a method of providing quantifiable results, a versatile platform for POC diagnostics and monitoring can be achieved.

Our overarching goal was to develop a flow-through electrochemical platform with the following characteristics:

1. Simple fabrication of a scalable tubular device, capable of interfacing with existing medical tubing
2. Sensing capabilities integrated directly into the flow area

3. Real-time electrical readout compatible with multiplexed signal acquisition and continuous monitoring

In brief, fabrication of the devices would be achieved using low-cost materials and techniques that can be scaled up for commercial production. The platform would be primarily tested and characterized using a model system based on nucleic acids as sample and recognition elements as they are inexpensive and have a wide range of applications. Electrochemistry would provide the means of converting biochemical events into electrical signals to obtain quantitative results, while flow would be achieved using pumps to precisely control the rate at which the solution flows through the system.

1.3 Research Objectives

The main objective of this research is to design and assess the performance of a scalable, low-cost fluidic transport system for electrochemical detection of biological markers. To accomplish this, the following sub-objectives were identified:

1. Design and fabricate electrodes within a flow-capable platform
2. Study the effects of key functional parameters such flow rate and electrode positioning on the resultant electrochemical signal
3. Optimize the system for the detection of nucleic acid sequences as a preliminary biological marker

1.4 Thesis organization

The thesis was separated into 6 chapters:

Chapter 2 provides the background information relevant to the conducted research and provides a brief review of the state of the art.

Chapter 3 describes the methods used to design and fabricate the tube platform.

Chapter 4 examines the iterative steps taken for the optimization and initial testing of the device.

Chapter 5 discusses the device properties and behaviour of the system under flow conditions.

Chapter 6 concludes the thesis with a summary of the key findings and a discussion of future work.

2 Background

This section provides a brief overview of the fundamentals of electrochemistry, biosensing, and microfluidics related to the design of a flow-capable electrochemical biosensor. Relevant information includes basic electrochemical theory and setup, common immobilization and detection strategies, and the governing principles of flow at micrometer scales. A brief state of the art is also provided.

2.1 Electrochemistry

2.1.1 Electrochemical systems

Electrochemistry is the study of electricity and its effects on chemical reactions, particularly at electrode/electrolyte interfaces [27]. Electrochemical measurements often employ a three-electrode system consisting of a working electrode (WE), a counter electrode (CE), and a reference electrode (RE) connected to a potentiostat to control and measure system parameters (Figure 2-1).

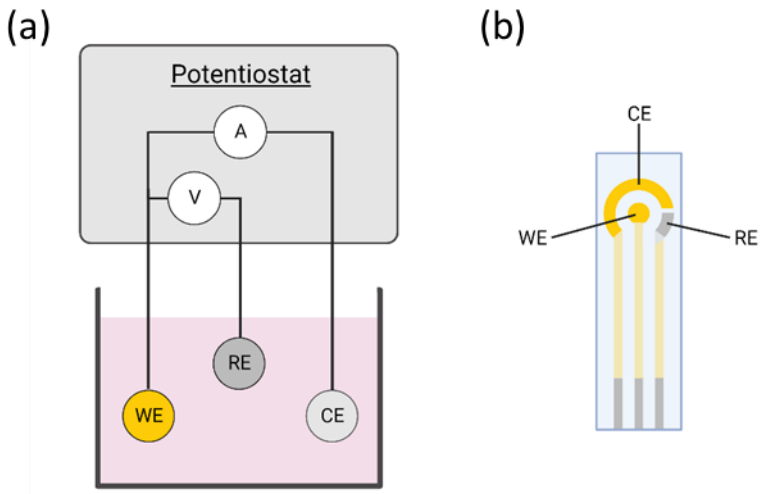

Figure 2-1. Three-electrode electrochemical systems utilizing a working electrode (WE), counter electrode (CE), and reference electrode (RE). *(a) Schematic representing a typical measurement configuration with accompanying potentiostat for monitoring of potential (V) and current (A) (b) Conventional commercially-available screen-printed-electrode used for analysis.*

The biochemical reaction of interest occurs at the surface of the working electrode [28]. Materials such as gold (Au) and platinum (Pt) are used for electrochemical biosensors as they are

conductive yet inert as to not influence or interact with the reaction. A second electrode, the counter electrode, completes the circuit and acts as the sink or source of electrons. The ideal counter electrode typically has a high surface area (relative to the working electrode) as to not limit reactions and should similarly be made of inert materials to avoid undesirable side-reactions [29].

The third electrode consists of a reference electrode to maintain a stable potential within the system. Reference electrodes should hold a constant potential to assess the potential of the reaction occurring at the working electrode. Additionally, they should exhibit high impedance which minimizes current flow as to not affect the potential. Many different types of reference electrodes are used in electrochemistry depending on the requirements of the system, with some of the most common examples including the standard hydrogen electrode (SHE), saturated calomel electrode (SCE), and silver/silver-chloride electrodes (Ag/AgCl) [10].

Less commonly, a single electrode may be used as both the counter and reference within the system. The two-electrode setup necessitates current to pass through the counter/reference combination, polarizing the electrode. In such a system, the current is influenced by the unstable potential, ultimately affecting the measured signal [29].

2.1.2 Reduction and oxidation reactions

Reduction and oxidation reactions are fundamental processes in electrochemistry and are used to describe the interaction between electrons or ions in solution and the electrode, commonly referred to as redox reactions [27]. The reduction reaction takes place at the cathode, where electrons are gained, while the oxidation reaction takes place at the anode, where electrons are lost. The redox reaction can be represented as:

$$\mathrm{Ox} + \boldsymbol{ne}^{-} \rightleftharpoons \mathrm{Red} \qquad \textbf{\textit{(1)}}$$

Where n is the number of electrons, e^{-}, and Ox and Red are the oxidized and reduced forms of the redox couple, respectively [27].

The direction and magnitude of electron transfer during a redox reaction can calculated using the Nernst equation [30]. The relationship between the working electrode potential and the concentration of the redox species is given by:

$$\boldsymbol{E = E^0 + \frac{RT}{nF} ln \frac{a_{\mathrm{Ox}}}{a_{Red}}} \qquad \textbf{(2)}$$

Where E is the resultant potential, E^0 is the standard potential of the reduction half-reaction at the electrode for the activity of the redox species a_{Ox} and a_{Red}. The remaining variables include the universal gas constant, R, the temperature, T, and Faraday's constant, F [30].

2.1.3 Electrochemical analysis techniques

Electrochemical detection methods can be categorized depending on the system properties being measured. Among the most commonly used techniques for biosensing include those measuring current (amperometric) such as chronoamperometry (CA), cyclic voltammetry (CV), and square wave voltammetry (SWV), or evaluating changes in the system's impedance (impedimetric) such as using electrochemical impedance spectroscopy (EIS) [31], [32]. These techniques can either involve the transfer of electrons and are considered Faradaic processes, or describe processes without charge transfer (similar to charging a capacitor) such as through the adsorption and desorption of a species, and are categorized as non-Faradaic processes [33], [34]. The waveforms of commonly used electrochemical techniques are shown in Figure 2-2.

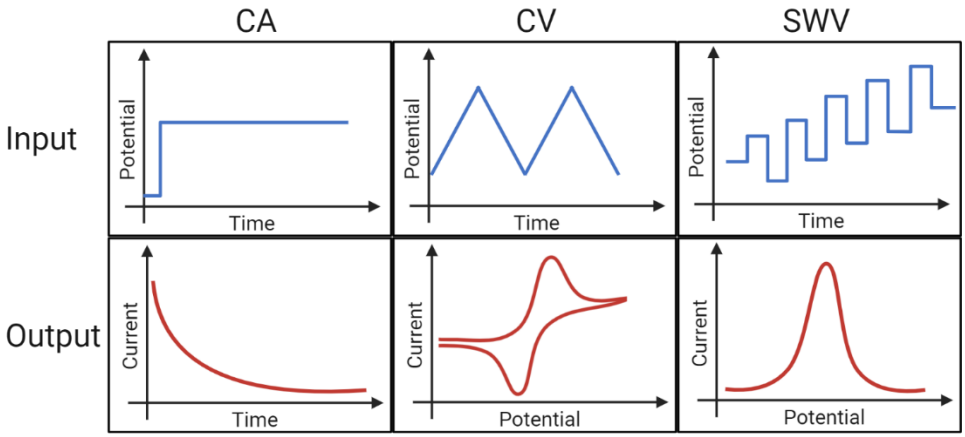

Figure 2-2. Input and output waveforms for common electrochemical measurement techniques. *Abbreviations – CA: Chronoamperometry, CV: Cyclic Voltammetry, SWV: Square Wave Voltammetry*

Chronoamperometry consists of applying a potential to the working electrode and recording the current response over time [29]. Generally, a starting potential is chosen such that the species of interest are either fully reduced or oxidized, and the potential is switched to one past the redox potential. Sudden polarization of the working electrode causes the analytes to either reduce or oxidize, resulting in a measurable increase in current, proportional to the concentration of the electroactive species [31]. As the reactive species is consumed near to the electrode surface, a concentration gradient known as the diffusion layer is created. As the diffusion layer grows, the measured current decreases with time [35].

In Cyclic Voltammetry, potential is swept between two set values typically chosen to induce repeated redox reactions. In situations where system redox properties are to be determined, CV can be used to determine the oxidation-reduction potentials. CV also provides valuable information on electron-transfer reactions is useful in characterizing surface modifications [36]. The technique is limited by the presence of significant non-Faradaic background current and the assumption of a fully-reversible reaction [30].

Square Wave Voltammetry reduces the effect of background current by applying potential in a square-wave pulse superimposed on staircase waveform [37]. The waveform consists of a series of voltage steps, with each step lasting for a fixed amount of time, followed by an immediate reversal of the potential to its initial value. The periodic nature of the square wave potential

allows for detection of both anodic and cathodic currents, providing information about the redox reaction at the electrode surface. As sampling occurs at the end of each step, the impact of non-Faradaic background current is negligible, allowing for more sensitive Faradaic analysis [38].

2.2 Biosensing

2.2.1 Biorecognition techniques

Electrochemical biosensor performance depends highly on the choice of biorecognition elements employed to interact with analytes. Biorecognition elements are biomolecules that selectively bind to the target analyte and initiate a biological response that can be transduced into a measurable signal [39]. The choice of biorecognition element depends on the nature of the target analyte, the required sensitivity and selectivity of the biosensor, and the compatibility with the electrochemical transducer [40].

Among the most commonly used biorecognition elements in electrochemical biosensors are nucleic acids [41]–[44], aptamers [45]–[48], enzymes [49], [50] and antibodies [51]–[54]. For the purposes of device characterization, nucleic acids were used as biorecognition elements primarily due to their ease-of-use, low cost, and well defined hybridization properties [55].

2.2.2 DNA biosensors

DNA (deoxyribonucleic acid) is a long polymeric molecule that encodes the genetic instructions of living organisms. It takes the shape of a double-stranded, helically coiled molecule consisting of a repeating series of nucleotides. Each nucleotide consists of either cytosine (C), guanine (G), adenine (A), or thymine (T) as bases, as well as a sugar-phosphate backbone. Nucleotides are joined together through the sugar and phosphate groups to form long chains, while the bases face inward. Hydrogen bonding allows complementary bases – A with T, C with G – to come together and form highly specific and stable pairs. The act of two complementary ssDNA strands joining is known as hybridization. Strands are commonly described in the direction of the 5'-end to 3'-end, with the 5'-end having the exposed phosphate group and the 3'-end having the deoxyribose sugar [56].

Biorecognition using electrode-bound DNA can be achieved using a variety of sensing principles [57]–[59]. The innate electrochemical properties of DNA causes hybridization to increase the

negative charge at the electrode due the negatively charged DNA backbone, and transitioning from a single-stranded configuration to a double-stranded coil conformation increases the conductivity allowing for increased electron mobility along the strand [58]. Furthermore, DNA hybridization changes the properties of the electrode-solution interface resulting in a measurable change in capacitance [60] and impedance [61].

2.2.3 Redox reporters

Measurement sensitivity of electrochemical DNA biosensors can be improved through the addition of redox species to enhance electron transfer. This can be achieved by methods such as adding redox reagents to the bulk solution or by direct labelling of DNA [57], [58].

Solution based redox reagents can be added to enhance signal change of events on the electrode surface, useful for interfacial characterization [58]. When biorecognition elements such as DNA are present on the electrode surface, the electron transfer kinetics of redox-capable species such as the commonly employed Ferrocyanide/Ferricyanide ($[Fe(CN)_6]^{4-/3-}$) couple are decreased [62]. Further changes in the electrode surface such as through hybridization reduce the available sites for redox reactions, leading to measurable signal attenuation [63].

DNA can be directly modified with redox labels for reagentless signal enhancement. Redox reporters such as Methylene Blue (MB) and Ferrocene (Fc) are widely used in electrochemical biosensors as electron mediators [64], [65]. Signal gain is attributed to increased electron transfer kinetics from the proximity of the redox label to the electrode as well as conduction along the double-strand [66]. For use in biosensors, covalent modification of DNA allows for sensitive analysis at well-defined potentials even in complex clinical samples [64]. These attributes combined with the versatility of redox labelled DNA has allowed for a variety of assay designs including competitive binding, sandwich-like labelling, and structure switching modes [67].

2.2.4 Surface preparation

Immobilization of DNA to the electrode surface is a crucial step in successful electrochemical biosensor fabrication [68]. Deposition is often achieved through the creation of a Self-Assembled Monolayer (SAM), where a monolayer of densely packed DNA is oriented perpendicular to the surface [69]. Several functionalization techniques have been employed such as the covalent bond

between carboxylated surfaces and amine-modified DNA, the high-affinity between biotin and (strept)avidin, and using the spontaneous bond formation between thiol-groups and certain noble metals [70]–[73]. Due to the simple and reproducible preparation steps, functionalization of the electrode surface used in this work was achieved using the thiol-gold bond.

SAM formation ultimately controls the steric and electrostatic properties of the DNA monolayer, impacting stability and hybridization efficiency [74]. Biosensor performance is sensitive to the molecular packing density on the electrode surface and can be improved by the filling of any bare, unreacted sites on the electrode through a second deposition step [75]. Blocking using 6-Mercapto-1-Hexanol (MCH) – a small, 6 carbon chain consisting of a thiol group on one end and a hydroxyl group on the other – has been shown to improve SAM formation and reduce non-specific binding [76]. The MCH displaces unbound DNA, resulting in a more orderly biosensing surface layer [61]. Additional passivation techniques have been employed to help biosensor performance against complex media by backfilling with Polyethylene Glycol (PEG), Bovine Serum Albumin (BSA), or zwitterionic species [2], [77], [78].

2.3 Microfluidics and flow phenomena

The flow of liquids at small scales operates differently than is expected from conventional experience. Forces that are often negligible at the macroscopic scale, such as surface tension or capillary forces, are of great importance for microfluidics whereas, others such as gravity and inertia have little effect [13]. Understanding these behaviors at the micro-scale can enhance the performance of biosensors by enabling efficient handling, manipulation, and analysis of biological samples.

2.3.1 Reynolds number

Reynolds number (Re) is a dimensionless number consisting of the ratio of the inertial forces to the viscous forces and is used to determine if a fluidic system is behaving in a laminar or turbulent regime. Typically, a value of less than 2300 is considered predictable, laminar flow. Values greater than 2300 indicate a turbulent system where exact fluid motion cannot be predicted [79], as shown in Figure 2-3.

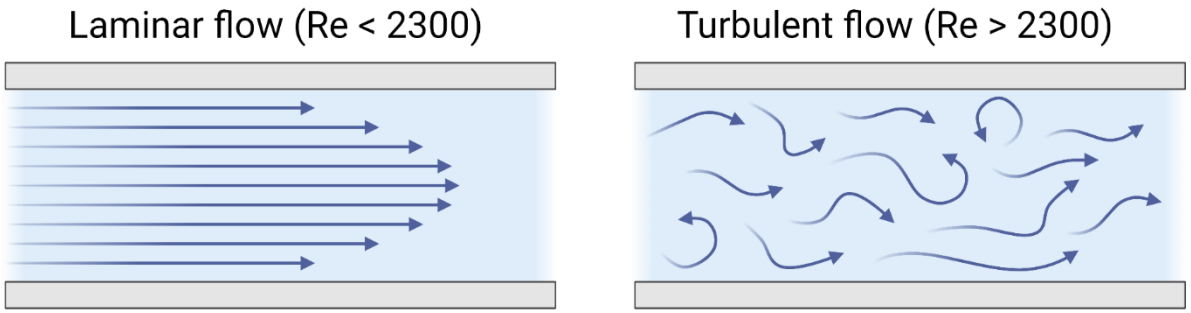

Figure 2-3. Comparison of laminar and turbulent flow regimes. *At low Reynold's number (Re), fluid travels in smooth, continuous layers with minimal mixing. High Re results in unpredictable, turbulent flow with poorly defined local pressures and velocities.*

Reynolds number can be calculated as:

$$\boldsymbol{Re} = \frac{\text{inertial forces}}{\text{viscous forces}} = \frac{\boldsymbol{\rho v D_H}}{\boldsymbol{\mu}} \quad \textbf{(3)}$$

Where ρ is the fluid density, v is the fluid velocity, D_H is the hydraulic diameter, and μ is the fluid viscosity [79]. Hydraulic diameter can be calculated as:

$$\boldsymbol{D_H = 4\frac{A}{P}} \quad \textbf{(4)}$$

Where A is the cross-sectional area, and P is the perimeter of the channel [13], [80]. For circular cross sections, the equation simplifies to be equal to the diameter of the channel.

2.3.2 Navier-Stokes equation and Poiseuille flow

Derived from Newton's laws, the Navier-Stokes equation provides a framework to understand how forces impact fluid behavior and can be applied to microfluidic devices. The Navier-Stokes equation for incompressible fluids is given as:

$$\boldsymbol{\rho(\partial_t v + v \cdot \nabla v) = -\nabla p + \mu \nabla^2 v} \quad \textbf{(5)}$$

Where ∂_t is the partial derivative with respect to time and ∇ is the gradient operator [13]. The effect of pressure is described in the term $-\nabla p$ and the contribution from viscosity is $\eta\nabla^2 v$. Applying a continuity equation ($\nabla \cdot v = 0$, fluid does not spontaneously appear or disappear), a no-slip wall condition (fluid infinitesimally close to interfaces have zero velocity), and assuming Poiseuille flow (pressure-driven flow that is not influenced by inlet/outlet conditions), a solution known as the Hagen–Poiseuille equation can be obtained:

$$\Delta \boldsymbol{P} = \frac{\boldsymbol{8\mu L Q}}{\boldsymbol{\pi r_{max}^4}} \tag{6}$$

Where ΔP is the change in pressure drop along the length of the channel L, Q is the volumetric flow rate, and r_{max} is the channel radius [13].

As a result of the no-slip condition, the velocity has a parabolic profile that depends on the distance from a wall:

$$\boldsymbol{v(r)} = \frac{\boldsymbol{\Delta P}}{\boldsymbol{4\mu L}}(\boldsymbol{r_{max}^2 - r^2}) \tag{7}$$

Where r is the position such that $r = r_{max}$ at the wall and $r = 0$ at the center of the channel [13], [80]. It can be seen that flow velocity is maximal (v_{max}) when $r = 0$ at the middle of the channel. A schematic of the parabolic velocity profile obtained during Poiseuille flow can be seen in Figure 2-4.

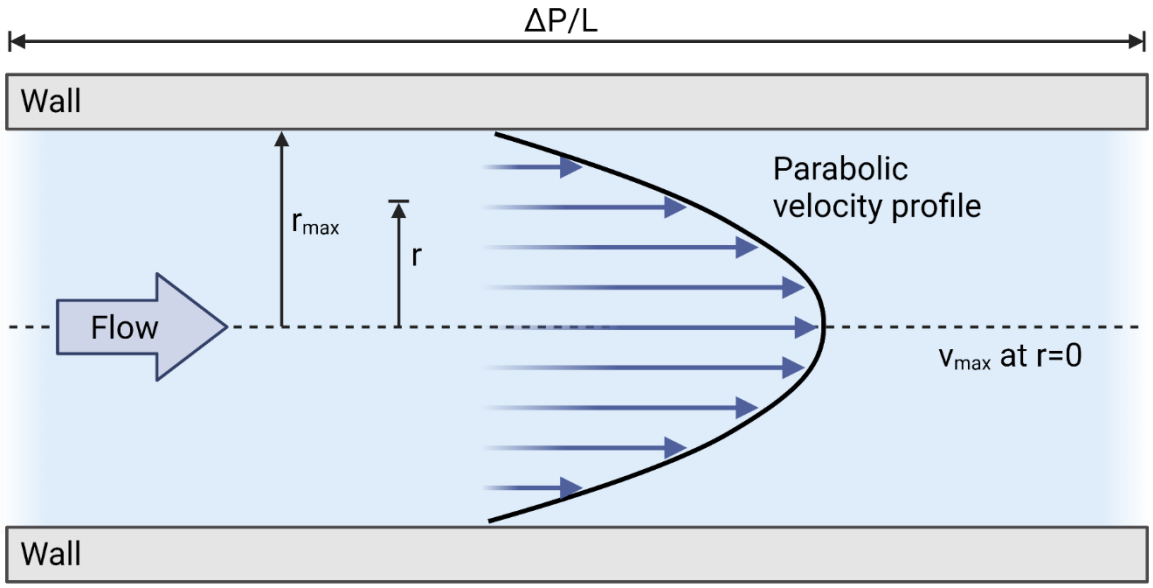

Figure 2-4. Schematic of 2-D Poiseuille flow. *Pressure-driven flow in a circular pipe can be approximated as having a parabolic velocity profile with zero velocity at the walls. ΔP is the change in pressure along the length of the channel L with radius r, with a fluid having volumetric flow rate Q.*

2.3.3 Mass-transport and reaction limited regimes

There exist several useful equations to gain an intuitive understanding of the transport of the analyte to the electrode surface. Here, the theoretical limits of flow phenomena are examined to help guide biosensor development using the simplified channel shown in Figure 2-5. The concepts described in this section are from the resources by Squires et al. [81] and Pereiro et al. [82] unless otherwise stated.

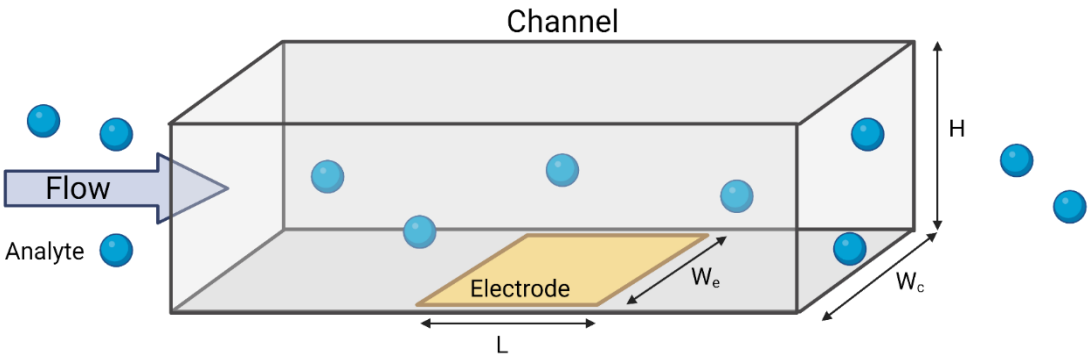

Figure 2-5. Simplified channel geometry used for analysis of flowing analyte behaviour. *The channel consists of a rectangular cross section of height H and width W_c containing an electrode with length L and width W_e.*

Analytes in solution are brought to the electrode surface primarily through two modes of transport: convection (advection) and diffusion. Convection is the motion of a particle due to the fluid's bulk motion in a particular direction, while diffusion is the probabilistic motion of a particle that moves in a random direction until an external force is applied, often from the interaction with another particle. This random movement of diffusion can be described in 1-dimension with the equation:

$$\boldsymbol{x = \sqrt{2Dt}} \tag{8}$$

Where x is the average distance travelled in time, t, of a molecule with diffusion coefficient D. The diffusion coefficient depends on the size, shape, and properties of the molecule of interest and the surrounding environment.

The Peclet number ($\mathrm{Pe_C}$) is used to relate the time needed for diffusive mass-transport to the time for convective mass-transport:

$$\mathrm{Pe_C} = \frac{\text{Diffusive time}}{\text{Convective time}} = \frac{2Q}{W_c D} \tag{9}$$

Where Q is the volumetric flow rate, W_c is the channel width, and D is the diffusion coefficient. For no flow or flow with small Peclet numbers (ie. $\mathrm{Pe_C} \ll 1$), mass transport due to the

movement of the fluid is low and analytes are brought close to the surface of the electrode primarily through diffusion. This results in a region of low concentration known as the depletion zone. Under low flow conditions, analyte is depleted upstream from the electrode due to diffusion and all of the target analytes are captured before passing the sensor. High Peclet numbers (ie. $\mathrm{Pe_C} \gg 1$) indicate that the movement of fluid is greater than the analyte's ability to diffuse to the surface of the electrode, resulting in uncaptured analyte flowing past the sensor. Only a thin region above the electrode has the chance to diffuse sufficiently close to the surface and be captured, as shown in Figure 2-6.

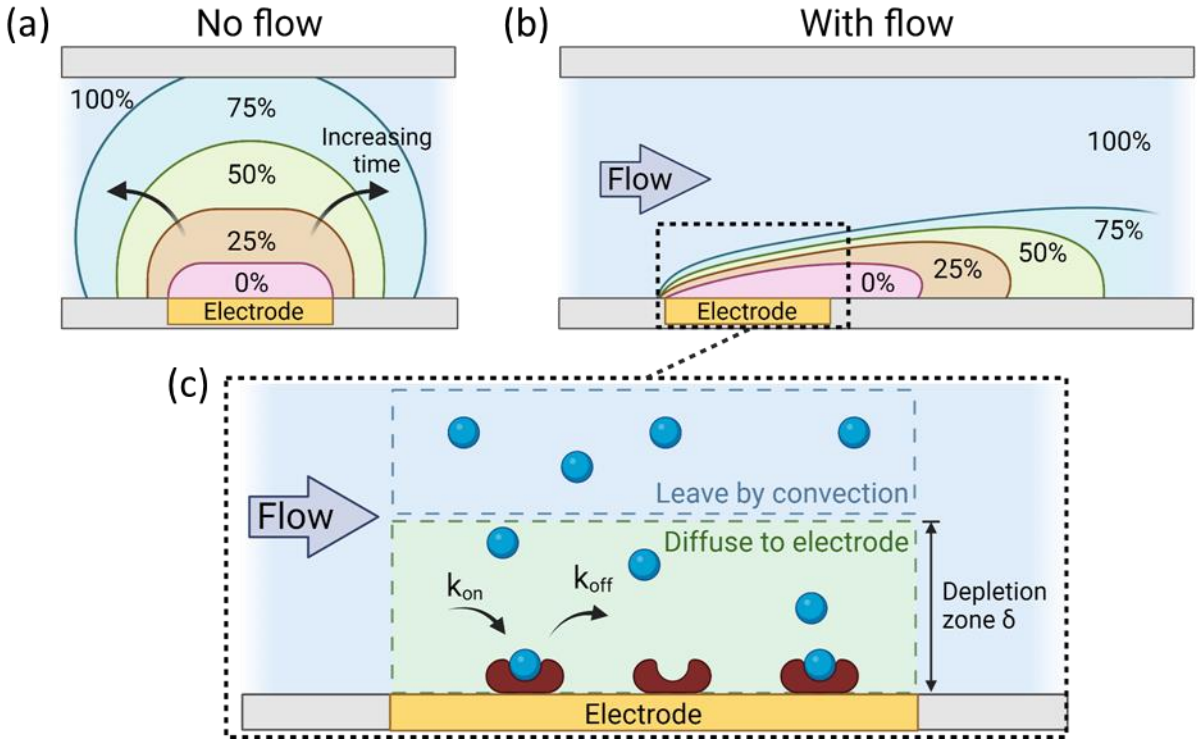

Figure 2-6. Effect of mass transport on the depletion zone, as indicated by remaining analyte percentage. *(a) No flow (diffusion only) produces a depletion zone that starts at the electrode and grows with time, filling the entire height of the channel and capturing all analyte. (b) Flow (diffusion and convection) produces a flattened depletion zone and loss of analyte at sufficiently high flow rates ($\boldsymbol{Pe_C \gg 1}$). (c) The height of the depletion zone produced under flow is governed by the balance of time taken to traverse past the electrode to the time taken to diffuse to the surface. Analyte outside of the depletion zone will not interact with the electrode surface. Note: is assumed that electrode never reaches a saturation state.*

The height of the depletion zone δ can be approximated by:

$$\boldsymbol{\delta \sim \left(\frac{1}{Pe_S}\right)^{\frac{1}{3}}}$$

(10)

Where $\mathrm{Pe_S}$ is the shear Peclet number given by

$$\boldsymbol{Pe_S = 6\left(\frac{L}{H}\right)^2 Pe_C}$$

(11)

Where L and H are the electrode length and channel height, respectively. The depletion zone equation is only valid for sufficiently high flow rates to create a depletion zone that does not extend the height of the channel.

The rate at which analyte is captured at the electrode surface is governed by both the inflow from mass transport as well as the reaction rate between the analyte and binding site. The collection rate due to mass transport, J_D, is approximated by:

$$\boldsymbol{J_D \approx Dc_0 W_e \mathcal{F}}$$

(12)

Where D is the diffusion coefficient, c_0 is the initial concentration of the target analyte, and W_e is the width of the electrode. $\mathcal{F}$ is a dimensionless flux approximated by

$$\mathcal{F} \approx 0.81\mathrm{Pe_S}^{1/3} + 0.71\mathrm{Pe_S}^{1/3} - 0.2\mathrm{Pe_S}^{1/3} \cdots$$

(13)

The reaction rate, J_R, can be approximated as:

$$J_R \approx k_{on} b_m c_0 L W_e$$

(14)

Where k_{on} is the association constant, b_m is the binding site density, c_0 is the initial analyte concentration, L is the length of the electrode and W_e is the electrode width.

When the collection rate is equal to the reaction rate, a useful value known as the Damkohler number (Da) can be obtained, which represents the ratio of analyte flux due to binding to that of diffusion:

$$\mathrm{Da} = \frac{k_{on} b_m L}{D\mathcal{F}}$$

(15)

Where k_{on} is the association constant, b_m is the density of the binding sites, L is the electrode length, D is the diffusion coefficient, and $\mathcal{F}$ is the previously calculated dimensionless flux.

The Damkohler number provides information on the relative kinetics of the surface reactions. If $\mathrm{Da} \gg 1$, the binding is faster than what can be provided by mass transport and a depletion zone is formed. For $\mathrm{Da} \ll 1$, the kinetics of the reaction are limiting the system.

The Damkohler number is particularly relevant for the task of designing flow-based biosensors. Flow properties can be modified such that the system reaches a reaction-limited regime (when $\mathrm{Da} \ll 1$), indicating that increases in mass transport will not significantly improve binding rates. As such, the reaction will proceed at the maximal rate dictated by the chemistry between analyte and binding site. However, the increased rate comes at the cost of decreased collection efficiency and loss of sample/reagents under high flow. For cases where sufficient sample volume is possible such as during blood collection or with urine samples, it is therefore beneficial to target a reaction-limited regime.

2.4 State of the art

Flow-based biosensors are rapidly emerging as a promising technology for the detection of biological analytes. In this section, a sample of flow-based biosensors capable of POC diagnostics is discussed, focussing on designs that use novel fabrication processes or unconventional methods to induce flow. Thorough examinations of more conventional techniques such as paper based devices and the use of intricate microfluidic channels has been previously reported ([13], [22], [83]) and are not included in reviewed work.

2.4.1 Single-channel Lab-on-a-chip designs

A common use of Lab-on-a-chip devices (Figure 2-7) is to automate the analysis of samples as they pass through the system.

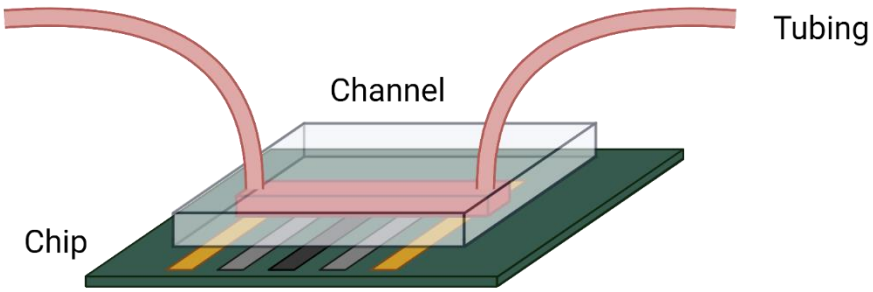

Figure 2-7. Basic single-channel lab-on-a-chip design, featuring a chip substrate, microchannel, and tubing connections.

Authors Uludag et al. have developed an all-in-one lab-on-a-chip biosensor for the detection of prostate-specific antigen where an electro-mechanical carousel-like system device automates several assay using steps before samples are automatically loaded into a 7 µL flow cell for electrochemical detection [84]. Flow in the range of 30-50 µL/min is used to achieve optimal antibody immobilization as well as rinsing of the sensing surface between sample injections. Similarly, automation is achieved by Moser et al. [85] and later Pontius et al. [86] using a flow-through cell with a total internal volume of only 0.15-0.3 µL for analysis of small volumes. The device consists of an array of electrodes integrated on a polyimide wafer sheet with a single-channel for use with flowing solution at rates ranging from 0.1 µL/min to over 10 mL/min. The researchers focussed on scalable manufacturing techniques and calibration of each device using to produce a commercially available product. An alternative approach to automation using microfluidic flow is described by Tan et al. [87]. Their system consists of immobilized enzyme integrated inside of a flow cell and a series of reagents loaded in a cartridge separated by airgaps. A series of 100 µL/min and stopped-flow segments allow for automated fluid handling, maximizing enzymatic activity and allowing for a 'one-click' operation scheme.

Authors Martinez-Cisneros et al. present an electrochemical, chip-based alternative to conventional optical detection methods [88]. A tubular impedimetric sensor was designed

consisting of electrodes on strained multilayer nanomembranes that, upon etching of a sacrificial layer, rolls into a compact microtube with a 30 µm outer diameter. The device was shown to detect various ionic species at low concentration and is capable of detecting the presence of single cells suspended in flowing solution. Similarly, Lab-on-a-chip technology was used to create a flowing alternative to a traditional enzyme-linked immunosorbent assay (ELISA) [89]. Liu et al. utilize continuous reciprocating flow to achieve sufficient immunobinding for detection of COVID-19 within 60 seconds instead of hour-long time scales of conventional ELISAs. Flow was achieved by modulating the pressure within the chip's microchannel to cause the sample fluid to repeatedly pass through the detection site, increasing the contact between antibodies and the antigens. Reciprocating flow also decreased sample consumption compared to purely flow-based enhancement techniques.

2.4.2 Needle and catheter-based tubes

An increasingly popular design for flow-through biosensors is the creation of needle or catheter-like devices with integrated electrodes using Kapton/polyimide films such as shown in Figure 2-8.

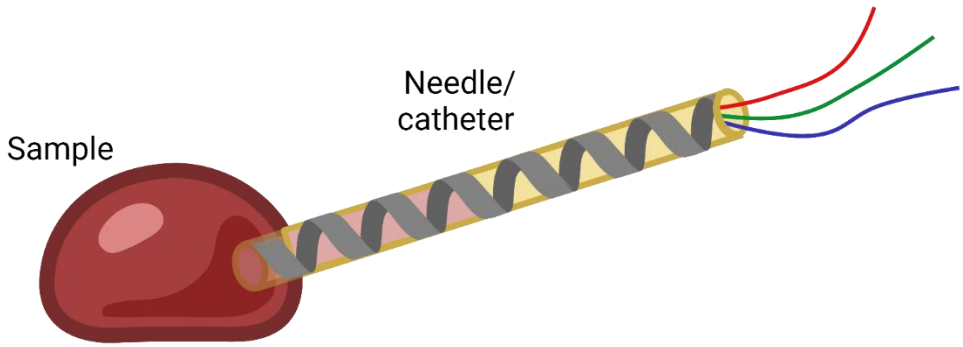

Figure 2-8. Common needle/catheter biosensor design capable of flow-through sensing.

Li et al. fabricate microsensors on the surface of Kapton film which is then spirally rolled into a tube for use as a cardiovascular catheter [90]. Unlike many other sensors, the catheter is capable of measuring both metabolic data as well as physiological data in the form of temperature and flow rate. The authors note that due to the fabrication technique, electrodes can be made on both the inside and outside of the film allowing for a wide range of applications. The same group led by Li et al. adapted their device to target in-vitro uses [91]. Instead of being used as a catheter,

the system uses either passive capillary forces to induce flow or is coupled to a transfer pipette for active flow. In doing so, transport of a variety of samples to the electrode area is achieved without the use of pumps.

Similarly, Park et al. have developed a 'Lab-on-a-needle' biosensor on rolled polyimide film [92]. Unlike Li et al. however, the film with patterned electrodes is rolled along the long axis of the film and is immobilized using heat-shrink tubing. The platform is slid inside a 1.2mm diameter needle for insertion into the body and subsequent detection of physiological concentrations. The authors focused on fabrication techniques that would yield low device-to-device variability and characterisation of electrode performance. Authors Kagie et al. describe their work consisting of a flexible screen-printed sensor for electrochemical analysis of tear fluid [93]. The device is created on polyimide substrate using a combination of screen printing and copper lithography and is rolled into a 0.7mm tube. The device can then be inserted directly into the tear canal for minimally invasive monitoring of biomarkers with the added benefits that tear fluid is a relatively clean bodily fluid that flows continually and thus required no externally induced flow techniques.

2.4.3 Wire electrodes in flowing samples

Other groups exploit the natural flow properties of the body and forego the tube-like design entirely and instead use implantable wire electrode systems similar to the device shown in Figure 2-9.

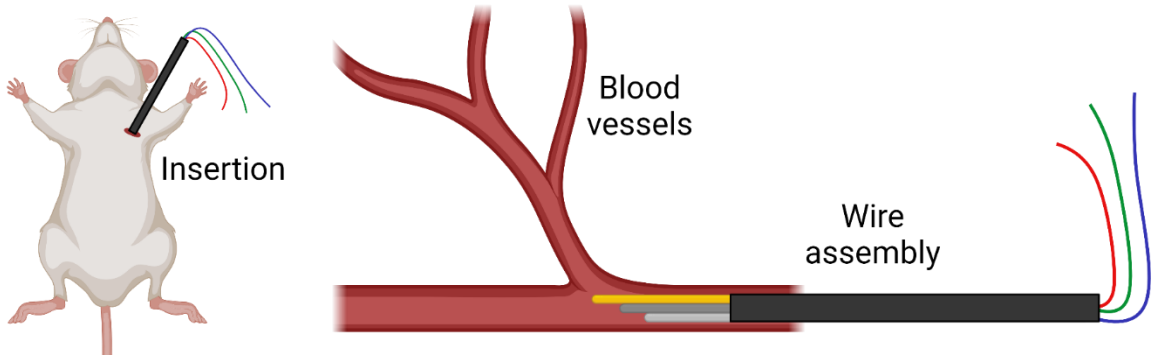

Figure 2-9. Example of an insertable 3-wire assembly for in-vivo sensing of flowing analyte.

Arroyo-Currás et. al utilize a combination of gold, silver, and platinum wires functionalized with aptamer that can be directly inserted into a vein for in-vivo monitoring [94]. The confined

operating space necessitates small sensor size however this is easily achieved using <200 µm wire. Due to the miniaturized electrode dimensions however, poor signal to noise ratio is obtained. The authors describe a roughening technique to increase the surface area of gold electrodes, doubling the signal to noise ratio of the un-enhanced wires. Dauphin-Ducharme et al. build on the system by incorporating closed-loop feedback of drug levels for not only monitoring but active intervention [95]. The system was adapted for real-time, seconds resolved measurements by Chamorro-Garcia et al. [96]. Detection was performed in undiluted whole blood to monitor administration of chemotherapy drug, necessitating tight tolerances for the controlled delivery to ensure patient safety.

Use of a similar 3-wire system for was performed by Leung et al. [97]. The group conducted a systematic exploration and characterization of the details pertaining to electrode placement in an effort to decrease capacitive background current. This work challenges the conventional wisdom that counter electrode geometry should be larger than working electrode for optimal performance. As a result of their efforts, a significantly enhanced signal-to-noise ratio during intravenous measurements was achieved. The work by Jin et al. uses a theoretical approach to sensor optimization, describing the equations governing mass transport to planar and wire biosensor surfaces under flow [98]. The authors examine the effect of planar versus radial diffusion and report that sensor length in the direction of flow is a critical parameter to consider when designing wire-based biosensors.

Relevant summary information for the systems discussed is given in Table 1.

Table 1. Summary of reviewed work

Sensor design	Materials	Target analyte	Readout method	Concentration	Flow rate (µL/min)	Flow method	Ref.
LoC	SiO_2 wafer, PMMA	PSA	CA (PSA antibody & HRP Au NP)	0.2 ng/mL (LOD)	30-50	Pump	[84]
LoC	Polyimide wafer, hydrogel	Lactate, glucose	CA (enzyme)	0.02 mM lactate, 0.05 mM glucose (LOD)	0.1-10000	Pump	[85], [86]

LoC	Silicone tubing, PDMS	Glucose & Ag^+	CA (enzyme)	-	~100	Pump	[87]
LoC	Ge/TiO_2/Cr/Au, PDMS	KCl, cells	EIS	0.1 nM KCl, single cell detection (LOD)	2-20	Pump	[88]
LoC	Glass, PDMS	COVID-19	Colorimetry (ELISA)	4.14 pg/mL (LoQ)	-	Manual pressure	[89]
Needle / catheter	Kapton film	Glucose	CA (enzyme)	20-150 mg/dl (linear)	1000-10000	Pump	[90]
Needle / catheter	Kapton film	Glucose, lactate, oxygen	CA (enzyme)	30 µM glucose, 50 µM lactate, 1 mmHg oxygen (LOD)	-	Pipette & capillary	[91]
Needle / catheter	Polyimide film, heat shrink tube	Glucose, lactate, pH	CA (enzyme)	-	-	Manual	[92]
Needle / catheter	Polyimide film	Glucose, norepinephrine, dopamine	CA (enzyme)	8 µM glucose, 165 nM norepinephrine, 530nM dopamine (LOD)	167	Pump, in-vivo	[93]
Wire	Au, Ag, Pt	Tobramycin	SWV (aptamer)	-	In-vivo	In-vivo	[94]
Wire	Au, Ag, Pt	Vancomycin	SWV (aptamer)	Maintain ±2 µM of desired	In-vivo	In-vivo	[95]
Wire	Au, Ag, Pt	Methotrexate	SWV (aptamer)	-	In-vivo	In-vivo	[96]
Wire	Au, Ag, Pt	Vancomycin	SWV (aptamer)	-	In-vivo	In-vivo	[97]

Abbreviations – Ag: Silver, Au: Gold, CA: Chronoamperometry, Cr: Chromium, EIS: Electrochemical impedance spectroscopy, ELISA: enzyme-linked immunoassay, Ge: Germanium, HRP: Horseradish peroxidase, KCl: Potassium chloride, LoC: Lab on a chip, LoQ: Limit of quantification, NP: Nanoparticle, PDMS: polydimethylsiloxane, PMMA: poly(methyl methacrylate), PSA: Prostate-specific antigen, Pt: Platinum, SiO_2: Silicon dioxide, SPE: Screen-printed electrode, SWV: Square wave voltammetry, TiO_2: Titanium dioxide.

3 Device fabrication and experimental methods

In this section, the required resources, fabrication processes and experimental methods used are described in detail.

3.1 Materials

3.1.1 Reagents

All DNA sequences (Table 2) were purchased from Keck Biotechnology Resource Laboratory (New Haven, United States). Gold(III) chloride solution ($HAuCl_4$, 99.99% trace metals basis, 30 wt. % in dilute HCl), phosphate buffer solution (PB, 1.0 M, pH 7.4), sodium chloride (NaCl, ≥99.0%), magnesium chloride ($MgCl_2$, ≥99.0%), potassium chloride (KCl), 6-mercapto-1-hexanol (MCH, 99%), tris(2-carboxyethyl)phosphine hydrochloride (TCEP), potassium hexacyanoferrate(ii) trihydrate ([Fe(CN)6]4−, ≥99.95%), and TWEEN 20 were purchased from Sigma-Aldrich (Oakville, Canada). Hydrochloric acid (HCl; 37% w/w) was purchased from Labchem (Zelienople, United States). Sulfuric acid (H2SO4, 98%) was purchased from Caledon Laboratories (Georgetown, Canada). Ethanol (ethyl alcohol anhydrous) was purchased from Commercial Alcohols (Brampton, Canada). All water used in experiments was purified using a Milli-Q Reference A+ Water Purification System (DI water).

Table 2. ssDNA sequences used for tube analysis.

ssDNA	Sequence (5`-3`)
Capture	TAG CTA GGA AGA GTC ACA CA **Z** **Z** = 3′-Thiol mod C6 S-S
Reporter	**M** TTT TTT GTG TGA CTC TTC CTA GCT A **M** = 5′ methylene blue
polyT	**M** TTT TTT TTT TTT TTT TTT TTT TTT T **M** = 5′ methylene blue

3.1.2 Electrochemical equipment

Unless otherwise state, electrochemical measurements were performed using an Emstat3 potentiostat (Palmsens BV, Houten, Netherlands).

3.2 Fabrication

3.2.1 Lab-In-a-Tube device

Tubes were fabricated on polyolefin shrink film (D-955 – 100 gauge, Sealed Air, Charlotte, United States) and overview of the fabrication steps is provided in Figure 3-1. The polyolefin was rinsed with 100% ethanol, followed by DI water. A mixture of water and soap (SoftCIDE-NA, VWR International, Radnor, United States) at approximately 100:1 ratio was sprayed onto the cleaned film. Adhesive vinyl (FDC Lumina 4304, FDC Graphic Films, South Bend, United States) with backing removed was applied to the film, starting in the centre, and applying force radially towards the edges to force the water and trapped air out from between the two layers.

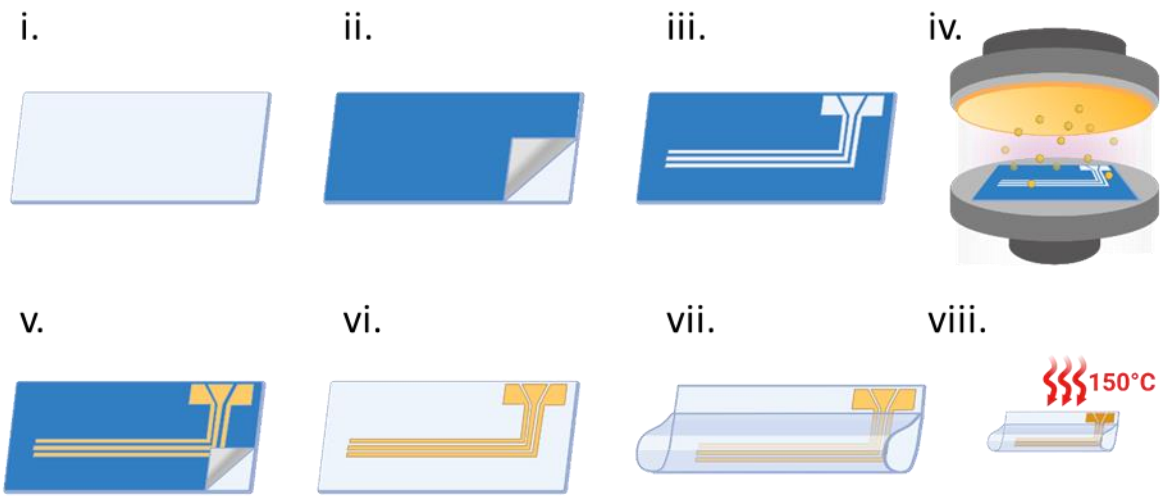

Figure 3-1. Lab-In-a-Tube fabrication schematic. *i.) Polyolefin film, ii.) addition of adhesive vinyl mask layer, iii.) electrode mask patterning, iv.) sputter deposition, v.) removal of vinyl mask, vi.) resultant electrodes on polyolefin, vii.) rolled and heat-sealed tube, viii.) shrinking at 150°C.*

The desired electrode geometry was designed in vector-graphic software and cut into the vinyl using a Robo Pro CE5000-40-CRP cutter and CB09UA blade (Graphtec America, Irvine, United States), with settings of cut force, quality and speed set to 12, 1, and 1 respectively. Cut regions of the vinyl were removed using tweezers to reveal underlying polyolefin film while the remaining vinyl acted as a protective mask.

A 40 nm gold layer from a 2-inch, 99.9990% gold target (Materion Corp., Mayfield Heights, United States) was sputter deposited using a magnetron sputtering system (CRC-600, Torr International Services LLC, New Windsor, United States) at a deposition rate of 0.6 Å/s. After removing the vinyl mask, the polyolefin film was folded to create the tube-like shape and held in place with double-sided tape for sealing with an Impulse Heat Sealer (PFS-200, iHotools). The sealed tubes were shrunk in a glass petri-dish placed into an oven at 150°C for 10 minutes.

After functionalization of the working electrodes, a 26-gauge needle (McMaster-Carr, Elmhurst, United States) is used to pierce a hole perpendicular to the tube. The reference wire is inserted into the perpendicular hole, and the counter electrode wire is inserted through the tube opening, parallel to the flow. Microfluidic tubing (Transfer Tubing, Microbore PTFE, 0.012" ID x 0.030" OD, Masterflex, Gelsenkirchen, Germany) or polypropylene dispensing needle (1-1/2" Long, 25 Gauge, with Luer Lock Connection, McMaster-Carr, Elmhurst, United States) is added to both sides of the tube to act as fluidic inlet and outlet connections. The system is sealed by applying an acrylic adhesive (Loctite AA 3035, Henkel AG, Aachen, Germany) to the inlet, outlet, and wire insertion areas.

3.2.2 Reference and counter wire

The counter electrode was made using gold wire (0.1 mm diameter, 99.998%, Thermofisher Scientific, Waltham, United States), cut into 3 cm sections. The wire was rinsed with 100% ethanol, followed by DI water. Nail polish was applied to the wire in areas to passivate where the wire would be in contact with the in-tube electrodes. Gold nanostructures were electrodeposited in a 10 mM $HAuCl_4$ and 0.5 M HCl solution, by applying a -0.2 V potential for 10 minutes with Ag/AgCl reference and platinum wire counter electrodes (CHI111 and CHI115, CH Instruments, Austin, United States).

The quasi-reference electrode was made using silver wire (0.203 mm diameter, 99.95%, Thermofisher Scientific, Waltham, United States), cut into 2cm sections. The wire was rinsed with 100% ethanol, followed by DI water. Nail polish was applied to the wire in areas to passivate the surface. The silver wire was chlorinated in a 1 M KCl solution, by applying 25 µA per centimeter of exposed wire, for 30 minutes using a Reference 600 potentiostat (Gamry Instruments,

Warminster, United States) with a platinum wire acting as both counter and reference electrodes (CHI115, CH Instruments).

3.3 Protocol

3.3.1 Scanning electron microscopy

The electrode surfaces were characterized by Scanning Electron Microscopy (SEM) (JEOL 7000F, JEOL, Peabody, United States). The gold working electrodes were prepared according to Section 3.2 without heat-sealing into a tube shape for easier imaging, using an accelerating voltage of 3 kV and a working distance of 6.9 mm. The nanostructured gold counter electrode was imaged using an accelerating voltage of 5 kV and a working distance of 6.9 mm, and the silver/silver-chloride reference electrode was imaged using an accelerating voltage of 5kV and a working distance of 7.5 mm. The gold working electrode samples were coated with 5 nm of platinum to reduce charging on the nearby polymer substrate.

3.3.2 Contact angle measurements

Bare gold samples were thoroughly cleaned using ethanol and DI water and subsequently dried. A 5uL droplet of water was deposited on the surface using a micropipette and high-resolution image data was obtained using a KRUSS DSA30S Drop Shape Analyzer (Hamburg, Germany). Droplet deposition and image acquisition was repeated for subsequent samples.

3.3.3 Surface area measurements

The tubes were rinsed with 100% ethanol followed by DI water to ensure a fully wetted surface. The electrodes were electrochemically cleaned using cyclic voltammetry (0-1.5 V vs. Ag/AgCl, 100 mV/s, 20 cycles) in 0.1 M H_2SO_4. Charge was obtained by integrating the area under the gold oxide reduction peaks, and the electroactive surface area was calculated using the surface charge density of a monolayer of gold of 386 $\mu C \cdot cm^{-2}$ [29].

3.3.4 Electrochemical detection of dopamine

A LIT device was rinsed with 100% ethanol, followed by DI water to fully wet the electrode surface. The electrodes were electrochemically cleaned using cyclic voltammetry (1 – 1.5 V vs. Ag/AgCl, 100 mV/s, 20 cycles) in 0.1 M H_2SO_4. Next, chronoamperometry was used to keep the electrode at a constant potential of 0.3 V vs. Ag/AgCl wire (using the wire as both the reference

and counter electrodes) in a 0.1 M PB solution until a stable current was obtained (approximately 2 minutes). At this stage, the device is ready for dopamine detection using a continuous chronoamperometry scan at 0.3 V. Sequential volumes of 50 µL of target solution were injected using a pipette, waiting 50 s between injections. Current value after 50 s (immediately prior to the next injection) were used as the measurement.

3.3.5 Recirculatory flow studies

A peristaltic pump (Ismatec Reglo Digital pump, 4-channel, 6-roller, Ismatec, Gelsenkirchen, Germany) with 0.38 mm inner diameter pump tubing (Puri-Clear™ LL, 3-Stop, Ismatec, Gelsenkirchen, Germany) was used for all recirculatory experiments, and the pump flow rate was calibrated prior to running the first sample. Each sample consisted of 500 µL of the target solution placed in a 1.5 mL microcentrifuge tube. Both the inlet of the peristaltic pump tubing and the outlet tubing of the tube were inserted into the microcentrifuge tube, creating a closed-loop system with fixed volume. Air was purged from the tubing when introducing the sample, bubbling out of the target solution as the microcentrifuge tube was exposed to atmosphere. A schematic of the setup is shown in Figure 3-2.

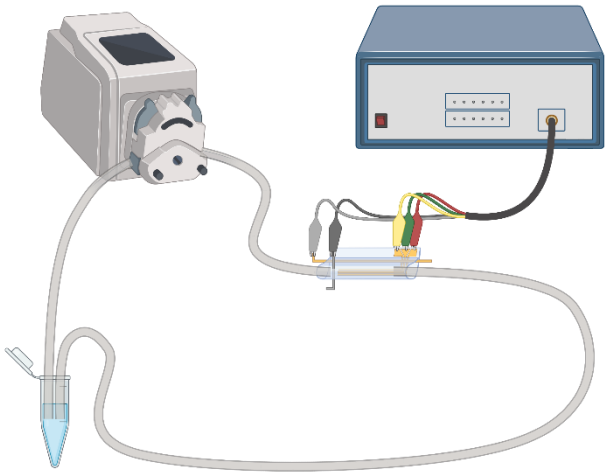

Figure 3-2. Recirculatory flow study schematic. *A fixed volume of target solution is made to recirculate through the Lab-In-a-Tube device using a peristaltic pump. A potentiostat can be used to perform measurements in real-time during flow or connected at the end of the flow duration to assess device performance.*

3.3.6 Use with blood collection tubes

A vacuum blood collection tube and holder (6 mL BD Vacutainer Serum Tubes, Becton, Dickinson and Company, Franklin Lakes, United States) was used as a low-cost, pump-less method to aspirate target sample through the LIT device (Figure 3-3). Luer connections enabled leak-proof method of attaching the device. As flow rate was influenced by the resistance of the connected tubing, all tests were performed using 10 cm of microfluidic tubing (Transfer Tubing, Microbore PTFE, 0.012" ID x 0.030" OD, Masterflex, Gelsenkirchen, Germany). The inlet end of the tubing was placed in the target solution and upon introduction of the blood collection tube to the holder, the solution was aspirated through the device. The combination of the specified blood collection tube and microfluidic tubing resulted full aspiration in approximately 3 minutes. SWV measurements were conducted in 25 mM NaCl and 25 mM PB solution as described in Section 3.3.9 immediately before and after blood collection tube operation, resulting in a total analysis time of less than 5 minutes. All steps were carried out at room temperature.

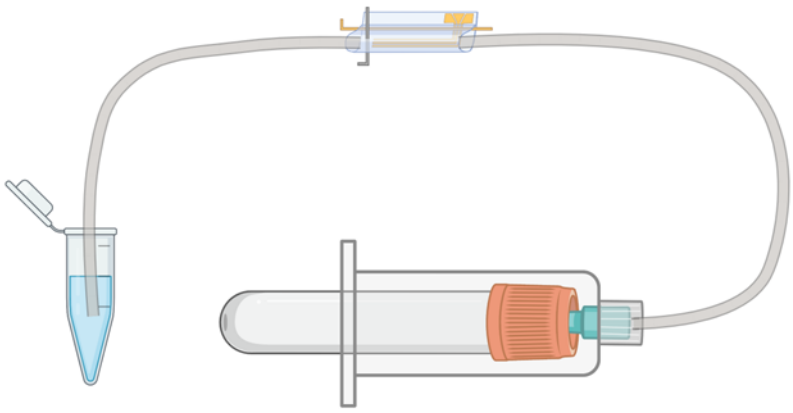

Figure 3-3. Lab-In-a-Tube device with blood collection tube for pump-less operation. *The low-pressure inside the blood collection tube causes the sample to be aspirated through the device until pressure is equalized.*

3.3.7 ssDNA probe deposition

The tubes were rinsed with 100% ethanol followed by DI water to ensure a fully wetted surface. The electrodes were electrochemically cleaned using cyclic voltammetry (0-1.5 V vs. Ag/AgCl, 100 mV/s, 20 cycles) in 0.1 M H_2SO_4.

The tubes were then filled with approximately 12 µL of 4.5 µM of thiol-terminated ssDNA capture probe (reduced with 1:100 ssDNA:TCEP ratio for 2 hours) and allowed to sit for 18 hours at room temperature in a dark, sealed container with a water-saturated disposable wipe to maintain a moist environment. The ssDNA solution was wicked out using a disposable wipe, rinsed with a solution containing 25 mM PB and 25 mM NaCl and filled with 100 mM MCH for 20 minutes to backfill the surface. The MCH solution was wicked out and replaced with aforementioned buffer solution until ready to proceed with the experiment. A schematic of the deposition and passivation process is shown in Figure 3-4.

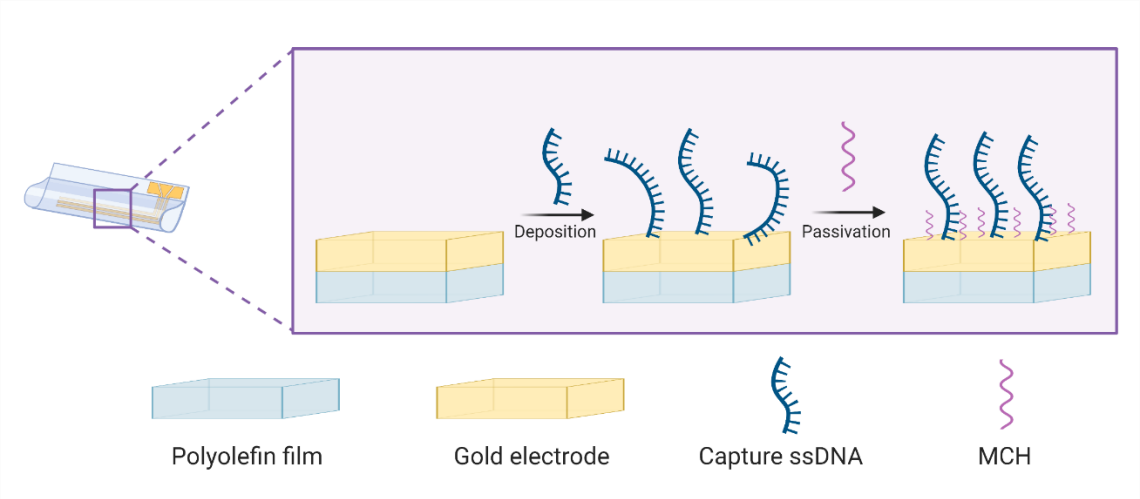

Figure 3-4. Tube electrode functionalization schematic. *The gold electrode is functionalized by deposition of capture ssDNA, forming a disorderly self assembled monolayer. Passivation with MCH helps orient the ssDNA to increase hybridization and blocks the remaining bare gold to decrease non-specific adsorbtion.*

3.3.8 Electrochemical characterization of ssDNA deposition

Deposition of ssDNA was evaluated using cyclic voltammetry by scanning from -0.3 V to 0.5 V (vs. Ag/AgCl) at a scan rate of 50 mV/s in a solution containing 2 mM potassium hexacyanoferrate(II), 25 mM PB and 25 mM NaCl.

3.3.9 Evaluation of ssDNA capture performance

After tube fabrication and functionalization, reporter ssDNA was diluted in a buffer containing 25 mM phosphate buffered solution, 25 mM NaCl, 100 mM $MgCl_2$, 0.001% Tween 20 to the desired concentration. Solution was flowed through the devices at room temperature. Hybridization of

complementary DNA was evaluated using square wave voltammetry over a voltage range of 0 V to -0.6 V (vs. internal Ag/AgCl quasi reference electrode), at a scan rate of 60 Hz, potential step of 1 mV, and with amplitude of 25 mV.

3.4 Analysis

3.4.1 SWV signal processing and analysis

Following data acquisition, the obtained SWV measurement data were subjected to following steps within the PSTrace software (Palmsens BV, Houten, Netherlands):

1. Smoothing using a Savitzky-Golay filter with window of 9
2. Baseline subtraction using a moving average baseline with window of 6 points
3. Automated peak detection between -0.2 V and -0.4 V

Reported values are provided as either peak magnitude, current density (peak magnitude divited by electroactive surface area), or by signal enhancement (percentage) as calculated by

$$Signal\ enhancement = \frac{I_2 - I_1}{I_1} \times 100\% \quad \textbf{(16)}$$

Where I_1 is the current obtained before sample incubation and I_2 is the current obtained after sample incubation.

3.4.2 Calculating the Limit-Of-Detection

The Limit-Of-Detection (LOD) was determined using the expression:

$$\mathrm{LOD} = \frac{3.3\sigma_{\mathrm{low\_conc.}}}{m} \quad \textbf{(17)}$$

Where $\sigma_{\mathrm{low\_conc.}}$ is the standard deviation of the sample with low levels of analyte concentration and m is the slope of the linear regression line [99].

4 Design considerations and rationale

In this section, the design considerations and rationale that informed the development of the proposed solution are described. First, factors that influenced the overall shape of the device such as the substrate, geometry of the electrode, and addition of microfluidic connections are discussed. The use of insertable wires is evaluated, including their composition and placement. Finally, preliminary flow testing is conducted to verify enhancement of biosensor function under flow.

4.1 System geometry

4.1.1 Device substrate

Heat shrink polyolefin film was used as a simple and cost-effective method to create the tubular shape for a flow-through electrochemical system. Due to the pre-stressed nature of the polymer, a phenomenon known as the 'memory effect' occurs when heating the material above the glass-transition temperature where the film is able to relax and change confirmation [100]. The polyolefin film used in this study exhibits an approximately 80% shrink in both the longitudinal and transverse directions when exposed to temperatures greater than 127°C as shown in Figure 4-1 (a). While the film shrinks along the direction of the plane, its thickness increases by a factor of 20 from 0.0254 mm to 0.50-0.53 mm. This shrinking property allows for both the miniaturization of the tube and increases its stiffness, as well as induces wrinkling of the gold electrode layer (discussed in detail in Section 5.1). The now rigid tubing allowed for the incorporation of inlet/outlet connections and prevented unwanted collapse of the channel.

Sealing of the tube as described in Section 3.2.1 results in a tear-drop like shape of the inner channel (Figure 4-1 (c)). Alternative sealing patterns such as shown in Figure 4-1 (d) can be used but are limited by the material properties of the film as excessive curvature from small channel radii causes the seal to fail upon shrinking, whereas the tear-drop like shape minimizes the stress the on seal and allows for smaller channel sizes. Ultimately, the tear-drop like shape was used in this study due to its consistent reliability, ability to make smaller-diameter channels, and ease of fabrication.

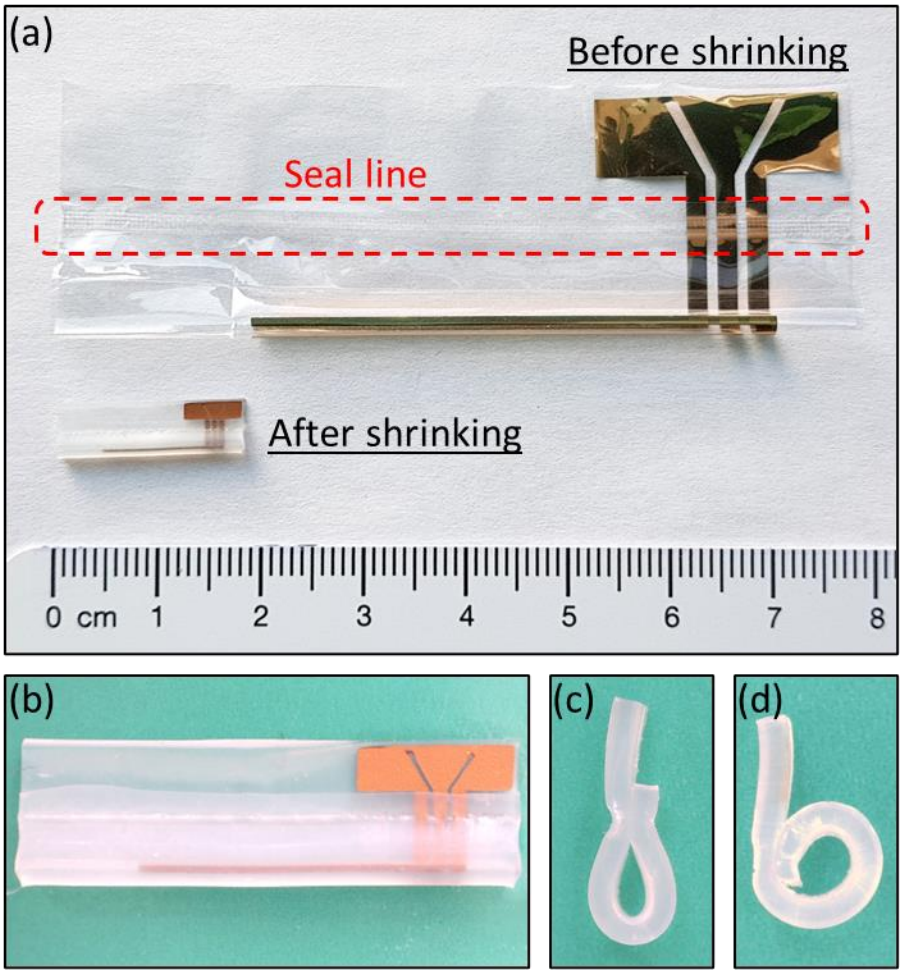

Figure 4-1. Tubular device with electrodes on polyolefin. *(a) The device before and after shrinking for 10 minutes at 150 °C, displaying an 80% decrease in size. (b) Close-up of the shrunk device with three longitudinal working electrodes. External contact pads are connected through the seal line, allow for electrochemical detection with the portion of the electrodes inside the tube. (c) Device cross-section displaying the 'tear-drop' shape due to sealing, allowing the smallest channel size tested. (d) Device cross-section displaying an alternate sealing method that allows for increased circularity at the cost of increased strain on the sealed area.*

4.1.2 Electrode geometry

The electrode geometry consists of rectangular sections along the inner length of the tube acting as working electrodes. The electrodes are connected to contact pads accessible on the exterior of the tube via rectangular strips that cross the heat-sealed section. As a portion of the connection between the working electrode and the contact pad resides inside of the tube, it is beneficial to minimize their surface area and therefore their impact on the functionalization/performance of the system. However, it was found that reducing the size of the

connecting sections smaller than approximately 0.2 mm resulted in consistent breaks of the electrodes during the heat-sealing process.

Both longitudinal and circumferential electrode designs with equal surface area were tested, and the longitudinal design was chosen due to its improved performance and ease of manufacturing compared to the circumferential design. In particular, the circumferential electrode arrangement caused issues with electrode functionalization as a result of the hydrophobic region created by the wrinkles acting as a barrier. The longitudinal electrodes created a hydrophobic region spanning only a small arc of the total perimeter and thus facilitated the insertion of fluid into the device.

Furthermore, 2- and 3- electrode versions were tested, as shown in Figure 4-2. The 3-electrode version allowed for triplicate measurements within a single device. Due to the fixed volume of the tube, a 50% increase in the concentration of the functionalization solution was added to account for the 50% increase in electroactive surface area from the additional electrode.

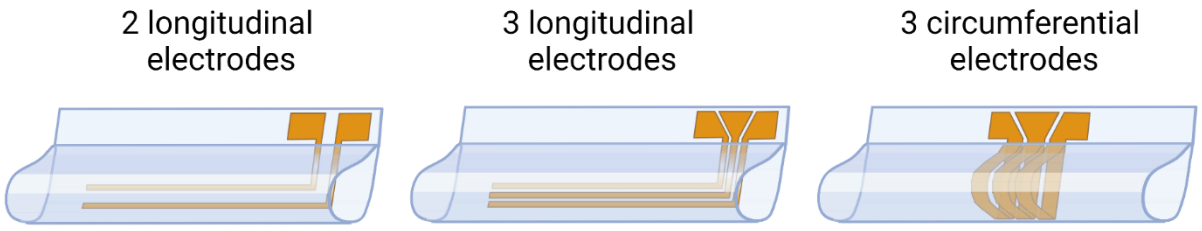

Figure 4-2. Overview of working electrode designs with 2 and 3 longitudinal electrodes or 3 circumferential electrodes.

Additional exploration of the electrode geometry beyond the simple rectangular shape would be beneficial. Electrode geometries could be optimized for maximal analyte capture or be designed for specific applications such as the production or release of one species at a first electrode and subsequent detection at a second, downstream electrode [101], [102]. The number of electrodes could also be increased; however the geometry and placement of the electrodes would need to account for the increased hydrophobic effects within the tube (further discussed in Section 5.1).

4.1.3 Tubing connection

Without adequate sealing, the solution in the system preferentially exits near the inlet or outlet connections instead of flowing through the outlet tubing, necessitating a sealant for proper use. The chosen adhesive would need to overcome two main problems: 1) Polyolefins have low surface energy and excellent chemical resistance which prevents bonding with many traditional adhesives [103], and 2) Surface tension and interaction with the tube geometry causes low viscosity adhesives to wick into the tubing, inhibiting sensing.

Common adhesives such as cyanoacrylate ('super glue') have low viscosity and spread over the electrodes before curing and fail to properly bond without additional surface treatment. Flexible materials such as of polydimethylsiloxane (PDMS) and other silicone polymers exhibit higher viscosity and could act as a gasket to prevent leaks, however the relatively long cure time prevented localized application and would not adhere to polyolefin. Standard two-part, UV-cure resins exhibit higher viscosity and faster cure time, however still fail to adequately adhere to the polyolefin or tubing.

It was found that specially formulated methacrylate adhesive gels designed for bonding low energy plastics (such as Loctite AA 3035) satisfied both conditions. Upon testing, the adhesive successfully prevented leaks at the pressures experienced at high flow rates of several millilitres per minute. A more thorough review of adhesives and surface modification is needed to ensure biocompatibility and improve manufacturability [104].

4.2 Inserted wire

Addition of wire was used to create 2-electrode and 3-electrode cells for electrochemical detection. Figure 4-3 demonstrates the main variations used when inserting wire, however exact wire placement and materials used varied with the experiment and is discussed below.

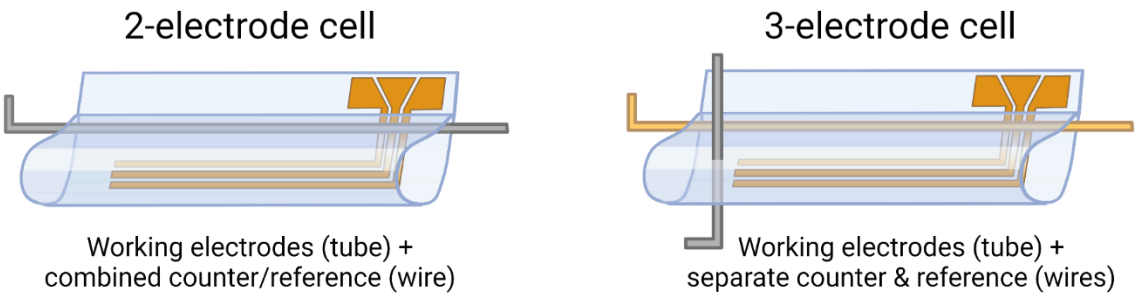

Figure 4-3. Schematic of 2- and 3- electrode electrochemical cells with inserted wire(s) for analysis. *Left: 2-electrode cell consisting of one of the working electrodes and a single wire acting as both counter and reference. Right: 3-electrode cell consisting of a wire acting as counter and a separate wire acting as reference.*

4.2.1 Effect of inserted reference/counter electrode wire material

To complete the electrochemical circuit, a minimum of two electrodes are required to act as the source and sink of the current being measured. Within the geometry of the tube however, there is insufficient space to accommodate commercial reference/counter electrodes commonly employed in electrochemical cells. Two solutions were considered:

The first option would be to include a dedicated reference/counter electrode(s) in the fabrication process. Screen-printed-electrodes can easily achieve this through swapping of screens to create the different electrode geometries and utilizing different conductive inks (such as Ag/AgCl for a reference electrode) to tailor the electrode properties based on their desired application. A similar technique could theoretically be achieved in a sputter deposition system; however this would necessitate specialized equipment not available at the time of this research. Manual mask and sputter material exchange is possible but would greatly increase device fabrication time. A system capable of changing masks to dictate electrode geometry/location and possessing multiple material deposition targets would greatly facilitate the fabrication process. Creating the reference/counter electrodes internally however poses an additional problem when introducing the biorecognition element during electrode functionalization. Due to the confined space within the tube, the capillary action causes the solution to be deposited to indiscriminately cover all electrodes. Only slight control of solution positioning longitudinally within the tube can be achieved by varying the volume of solution introduced into the system.

The second option is to functionalize the working electrodes inside of the tube before addition of the reference/counter electrodes to prevent unwanted binding on these surfaces. Commercially available wires are offered in sizes that can be inserted into the tubing (12.7 - 250 µm) and can be obtained relatively inexpensively to make single-use electrodes. Various materials were tested as counter/reference electrodes in a 2-electrode system. The results are shown in Figure 4-4.

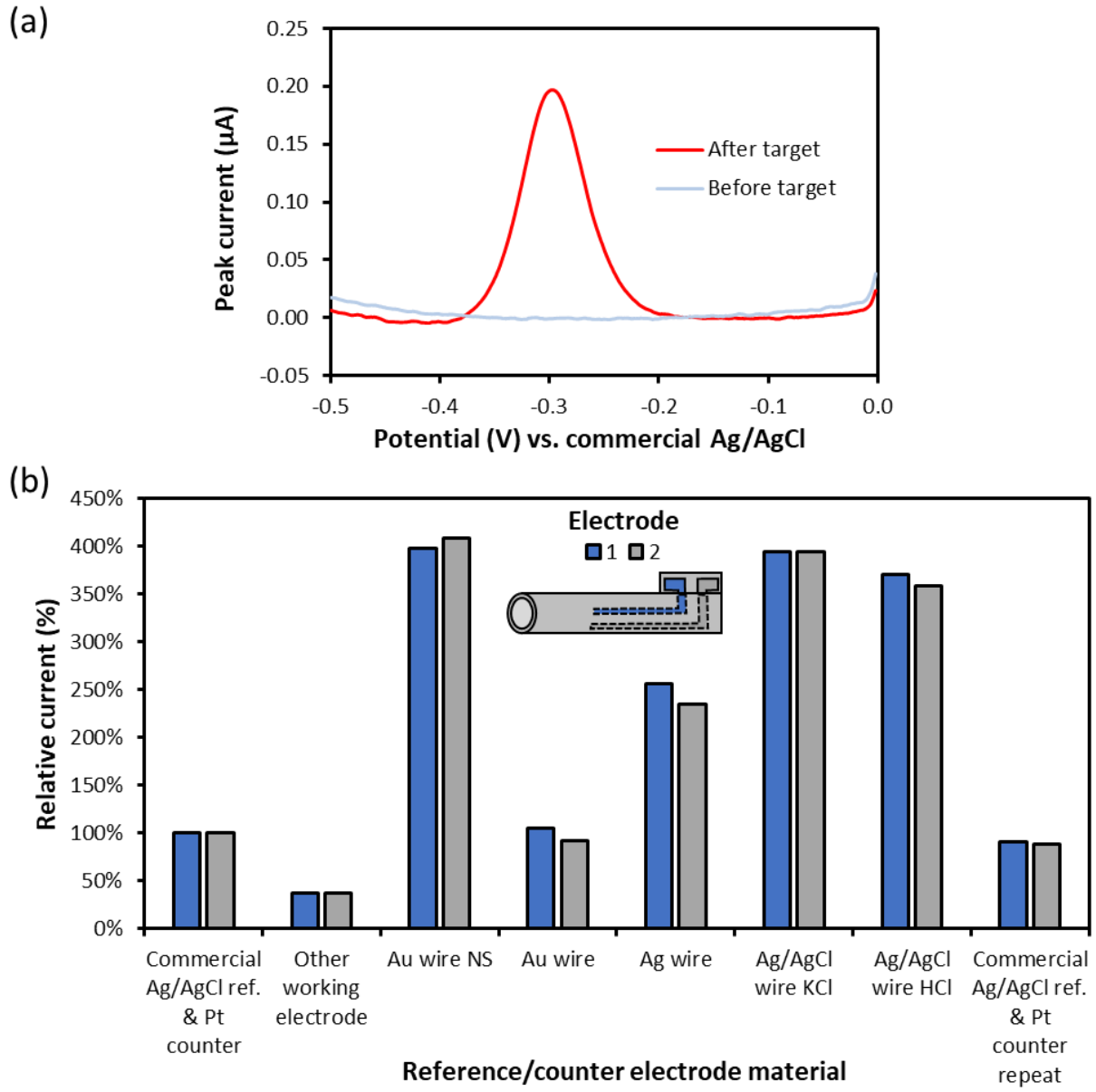

Figure 4-4. Comparison of reference/counter electrode materials on measured current. *A tube containing 2 working electrodes functionalized with capture ssDNA (3 µM overnight, followed by*

10 mM MCH for 10 minutes) was incubated for 20 minutes with 10 µL of 100 nM reporter ssDNA under no-flow conditions for hybridization. (a) Representative electrochemical response of the electrode upon measurement with SWV versus the commercial Ag/AgCl reference electrode. Before addition of the reporter ssDNA, no peak is observed. After hybridization, a clear methylene blue peak can be seen. (b) Peak signals were obtained by sequentially varying the reference/counter electrode in the order shown (left-to-right). Plotted current was normalized to the values obtained with the external commercial Ag/AgCl reference and platinum counter. All SWV measurements were done in a solution containing 25 mM phosphate buffer solution with 25 mM NaCl at room temperature. Abbreviations – Ag/AgCl: Silver/Silver-Chloride, Au: Gold, Ag: Silver, HCl: Hydrogen Chloride, KCl: Potassium Chloride, NS: Nanostructured, Pt: Platinum.

The investigation consisted of measuring the peak SWV current of a single 2-electrode tube following target hybridization according to a variation of the protocol described in Section 3.3.9, with the exception that the reporter was allowed to hybridize under static conditions. The tube was first dipped in a solution with a standard Ag/AgCl reference electrode and platinum wire counter electrode. A measurement was obtained as a baseline to identify if any signal decrease was observed throughout testing. After obtaining the baseline, a total of 6 reference/counter options were tested. Wire placement was kept as consistent as possible between measurements to avoid any impacts related to wire positioning. Excluding the baseline signals, all measurements were carried out as a 2-electrode cell with the working electrode inside the tube and the additional electrode under investigation acting as both the reference and counter electrodes.

First, the 'other working electrode' configuration was evaluated by connecting one of the tube electrodes as the working electrode and the other was connected as the reference/counter. The resultant peak current was considerably lower than the first measurement, approximately 38% of the signal that was obtained using commercial Ag/AgCl reference electrode and platinum wire counter electrode, and a similar value was obtained by swapping the electrodes. The low signal is likely attributed to the polarization of the reference/counter electrode leading to inaccurate characterization of the system [29].

Next, both nanostructured (described in Section 3.2.2) and unmodified gold wire were evaluated. The nanostructured gold wire resulted in 397% and 408% increased signal over the commercial Ag/AgCl reference and platinum counter, whereas the bare gold wire exhibited no significant effect with values of 105% and 92% that of the commercial setup. The surface area of the wires

may explain the large discrepancy. The relatively low surface area of the smooth, bare gold wire may have limited the system compared to the high-surface area nanostructured gold wire. A significantly negative potential shift was observed, believed to be due to the gold shifting the reference potential [105].

Different variations of silver wire were subsequently tested. Unmodified silver wire resulted in a 256% and 235% increase over the commercial Ag/AgCl reference and platinum counter. A possible reason for the increase in signal compared to the bare gold wire could be related to the surface area effect described previously, due to the larger diameter of the silver wire, but the cause was not further investigated. A reference/counter made from a silver wire that was chlorinated in a 1 M potassium chloride solution (as described in Section 3.2.2) produced 394% and 395% signal over the commercial Ag/AgCl reference and platinum counter, while a silver electrode chlorinated in a 1 M hydrogen chloride solution following a similar protocol yielded a 370% and 359% signal response. Similar to the nanostructured gold wire, the chlorinated silver wires exhibit high surface area due to the rough surface texture.

The final measurements with the commercial reference and counters resulted in 91% and 89% signal magnitude compared to the average of the initial measurements, suggesting that a slight loss of signal occurred throughout the measurements. As this difference is relatively small and the differences in signal magnitude between reference/counter configurations was quite large, the information gained is still useful for consideration.

The results suggest that high surface area nanostructured gold and both Ag/AgCl electrodes would be viable reference/counter electrodes capable of being inserted after working electrode functionalization. The Ag/AgCl made in a potassium chloride solution was of particular interest due to the ease of handling compared to hydrogen chloride. The nanostructured gold wire yielded good results, however was more expensive to produce. The unmodified gold and silver wires offered few benefits (namely ease of fabrication) that were overshadowed by the performance enhancement of the modified wires. Finally, connecting one electrode inside the tube as the reference/counter, while commonly used with IDEs, was not well suited to Faradaic current measurements. Such an arrangement would be particularly useful for impedance and

capacitive measurements and would warrant further investigation if the biosensor was designed with these attributes as the main detection mechanism [106].

4.2.2 Effect of wire position on readout signal

The influence of the wire location in relation to the working electrode was investigated. A 2-electrode system was constructed using a Ag/AgCl wire and a tube with circumferential working electrodes to better control the relative distance of the wire and to highlight any effect observed. SWV measurements were recorded following target hybridization according to the protocol described in Section 3.3.9. The wire was positioned first by insertion from the left side of the tube and held approximately 1mm from the left-most working electrode. After measurements were obtained on all three electrodes, the wire was positioned from the right side and the measurements were repeated. The resultant data is plotted in Figure 4-5.

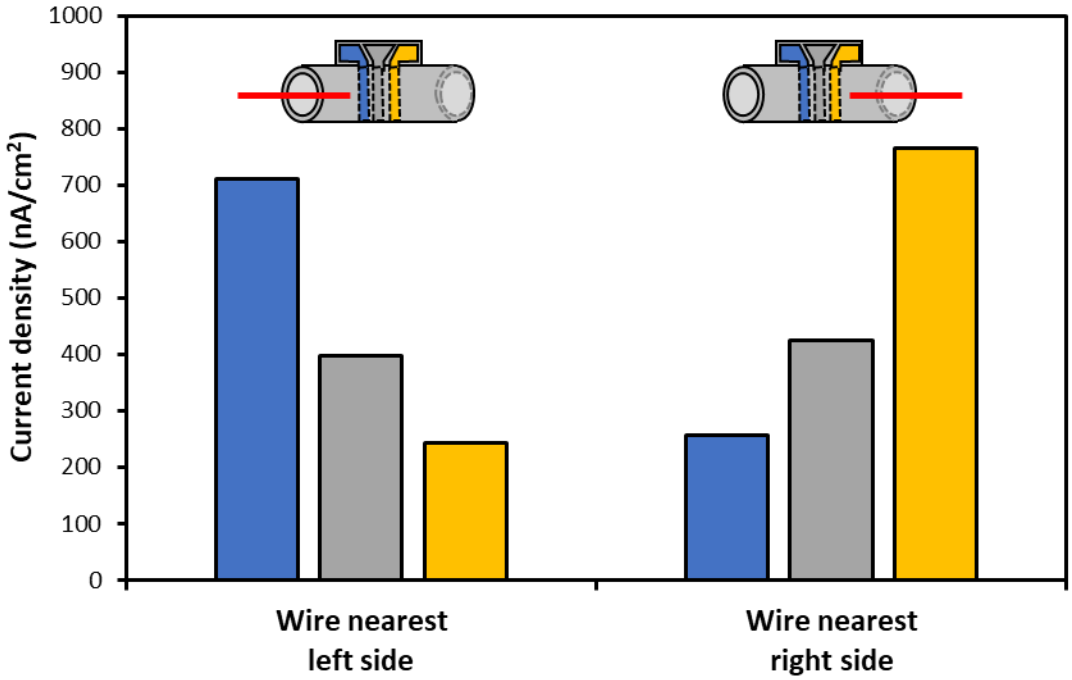

Figure 4-5. Effect of reference/counter wire positioning on measured current. *A tube containing 3 circumferential working electrodes functionalized with capture ssDNA (4.5 µM overnight followed by 100 mM MCH for 10 min) was incubated for 20 minutes with 500 µL of 100 nM reporter ssDNA recirculating at 50 µL/min for hybridization. Square-wave voltammetry was performed in a solution containing 25 mM phosphate buffer solution with 25 mM NaCl while varying the position of a Ag/AgCl wire acting as both reference and counter. All measurements and hybridization steps were conducted at room temperature.*

The influence of wire positioning on the obtained signal was significant: the electrode closest to the wire resulted in the highest current, followed by the middle electrode, and finally the furthest electrode. This result is consistent with the phenomenon of ohmic resistance due to the electrolyte solution [107]. Therefore, consideration had to be taken to properly position the system's electrodes to minimize factors such as ohmic drop.

Next, optimal wire positioning of a 3-electrode system was evaluated within the LIT device. Possible wire positions consisted of either being placed along the tube's length or perpendicular by piercing through the tube. The wires could then be connected as either the reference, the counter, or a reference/counter combination. The SWV current for each of the 4 combinations possible was recorded for a set of longitudinal tube electrodes, as shown in Figure 4-6. Current density was normalized to the 'wire-along' arrangement for comparison purposes as this was the previously used configuration.

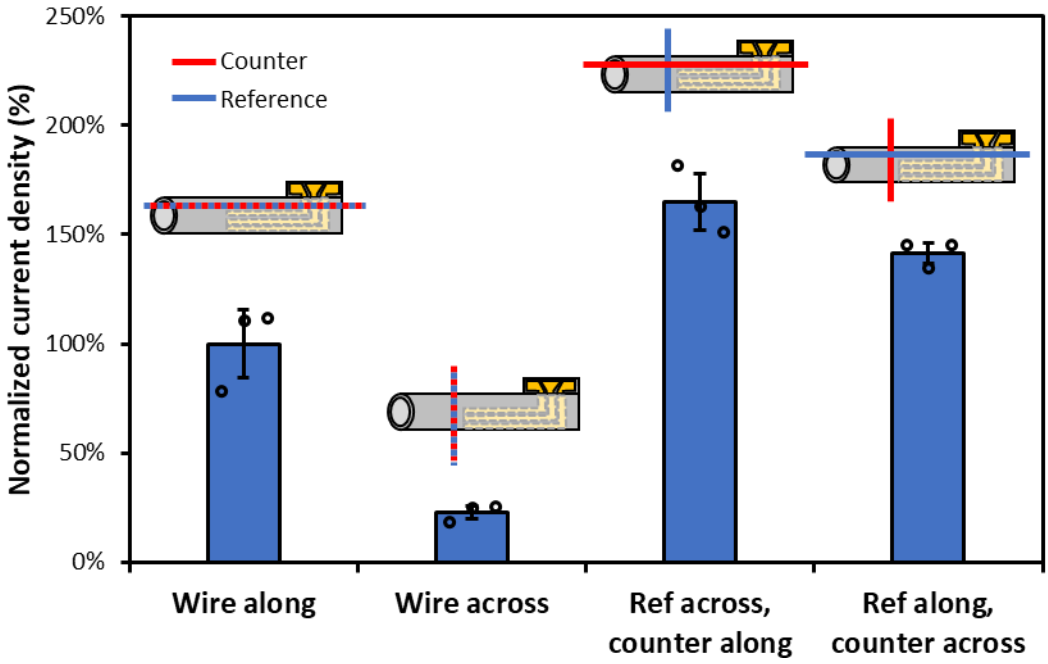

Figure 4-6. Comparison of various Ag/AgCl wire reference & counter electrode arrangements inside the LIT device. *A tube containing 3 longitudinal working electrodes functionalized with capture ssDNA (4.5 µM overnight, followed by 100 mM MCH for 10 minutes) was incubated for 20 minutes with 500 µL of 100 nM reporter ssDNA recirculating at 50 µL/min for hybridization. Square-wave voltammetry was performed in a solution containing 25 mM phosphate buffer solution with 25 mM NaCl while connecting different combinations of Ag/AgCl wire as either*

reference, counter, or both. All measurements and hybridization steps were conducted at room temperature. Plotted current density was normalized to the results of the previously used status quo 'wire-along' arrangement acting as both counter and reference. Abbreviation – Ref: Reference.

The 'wire-across' orientation resulted in significantly lower signal at 23% of the 'wire-along' value. This result is believed to be due in part to the non-ideal placement of the wire, increasing the ohmic drop due to the greater distance between the bulk of the working electrode area and the wire [107]. Both configurations using dedicated reference and counter electrodes resulted in higher signal with a 165% increase for the 'reference across, counter along' and 141% increase for the 'reference along, counter across' orientations. This result is believed to be due to the more ideal 3-electrode setup allowing for better measurement of the redox reaction occurring at the surface of the working electrodes through dedicated reference and counter electrodes [29]. As such, the 'reference across, counter along' arrangement was used as the optimal placement within the LIT device as shown in Figure 4-7.

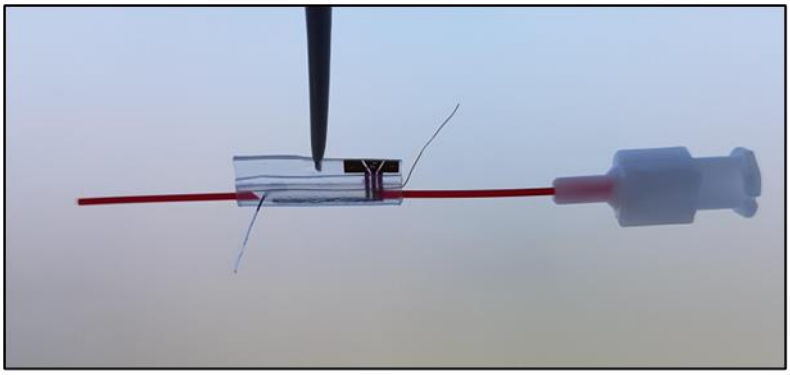

Figure 4-7. Sample image of a LIT device in a 3-electrode cell configuration with 'reference across, counter along' wire placement. *A counter electrode is placed along the top of the channel. The reference electrode can be seen piercing the tube, positioned such that it is located near the end of the working electrodes.*

4.2.3 Silver/Silver-Chloride Reference Electrode

The Ag/AgCl reference is the most commonly used electrode due to its simplicity, reproducibility, lack of toxic components, and simple fabrication methods [27], [35]. These attributes also make it a good candidate for use in low cost, disposable, POC sensors and was therefore used in the LIT device. The references electrodes were prepared according to methods outlined by Zoski et al. [27] and is described in Section 3.2.2.

As the reference electrode is in contact with the solution flowing through the device, the concentration of ions surrounding the Ag/AgCl electrode will vary with the composition of the solution. Due to this variability in ion composition (particularly chloride and silver), the Ag/AgCl wire is polarizable and acts as a pseudo (or quasi) reference electrode [108]. To minimize the effect of chloride ion concentration on the electrode's potential, ssDNA capture experiments were conducted with a consistent 25mM NaCl concentration [86].

The Ag/AgCl electrode is incorporated into the final 3-electrode electrochemical system by piercing the sidewall of the tube and inserted perpendicular to the direction of flow. From the results in Section 4.2.2, the 'reference across, counter along' orientation displayed the highest resultant signal. Piercing through the sidewall of the tubing allowed for consistent positioning while avoiding shorting issues with either the inserted counter electrode wire or working electrodes. Furthermore, this method of keeping the reference electrode physically separated from the system until after the functionalization of the working electrodes prevented unwanted deposition/contamination. As only a small section of the Ag/AgCl wire is exposed however, overall surface area is comparatively low, potentially negatively affecting the reference electrode's long term stability [109].

4.2.4 Nanostructured Gold Counter Electrode

A nanostructured gold wire is used as counter electrode within the final 3-electrode LIT system. As the counter electrode acts as the current/sink of the electrons within the system, the surface area must be kept higher than that of the working electrode to not be a limiting factor in the reaction taking place at the working electrode surface [35]. The nanostructuring was performed to increase the surface area of the bare gold wire greater than that of the wrinkled working electrodes. The wire is inserted into the tube and is positioned in the 'tip' of the teardrop-like shape of the tube (Figure 4-1 (c)). This arrangement was used to keep a consistent distance to the working electrode. Fabrication details are described in Section 3.2.2.

4.3 Preliminary flow testing

4.3.1 Numerical approximation of device behavior under flow

Numerical modelling was used to gain a more intuitive understanding of the effect of flow rate on biosensor performance. Values presented here are not intended to be fully accurate representations of the system's behavior. Rather, they are approximations meant to provide a better understanding of potential outcomes. Many of the values used in this section are estimates meant to approximate the result within 1-2 orders of magnitude.

The parameters listed in Table 3 encompass the geometric dimensions of the device (width and length for both the electrode and channel) as well as a diffusion coefficient and binding site density appropriate for bound and free-floating ssDNA. Approximate association and dissociation coefficients were obtained from similar ssDNA systems [110]. An analyte concentration of 100 nM was used as an intermediate between typical LOD and saturation values.

Table 3. Parameters used for numerical modeling.

Parameter	Value	Unit	Reference
Electrode width	600	μm	
Electrode length	4000	μm	
Channel width	700	μm	
Channel height	700	μm	
Initial concentration	1.00E-07	M	
Density of water	1000	Kg m^{-3}	[111]
Viscosity of water	1.00E-03	Pa s	[112]
Diffusion coefficient	100	μm^2 s^{-1}	[113]
Binding site density	4.50E+12	cm^{-2}	[114]
Association constant	2.40E+04	M^{-1} s^{-1}	[110]
Dissociation constant	2.00E-02	s^{-1}	[110]

First, the Reynolds number was estimated to verify if the flow regime was laminar. Using Equation (3), a Reynolds number of 48 was obtained for a volumetric flow rate of 2000 μL/min. As the

value of $\mathrm{Re} \ll 2300$, the system remains well within a laminar flow regime for the expected flow rates. Only approaching flow rates on the order of 96600 µL/min would result in turbulent flow. The system can therefore be modelled without the influence of turbulence or chaotic behavior.

Next, the impact of flow rates ranging from 1 µL/min to 10000 µL/min on the crucial operational characteristics identified in Section 2.3.3 is evaluated.

Both channel and shear Peclet values were much greater than 1 for all flow rates examined (Figure 4-8 (a)). The high channel Peclet indicates that a depletion zone smaller than the height of the channel is created (Figure 4-8 (b)), while the high shear Peclet suggests that the depletion zone is thin relative to the electrode length [81]. This can be imagined as a small region of low-concentration directly above the electrode as a result of binding depleting the local analyte faster than it can be replenished through mass-transport. Only the analyte within the height of the depletion zone has the possibility of interacting with the electrode, as this height corresponds to the same amount of time needed to reach the electrode via diffusion as it would for the analyte to convect past the electrode due to flow. As mass transport of analyte to the electrode surface is inversely related to the height of the depletion layer, it is advantageous to increase flow rates to decrease the time needed for capture (until the limits of reaction kinetics are reached). Conversely however, high flow rates result in poor overall capture efficiency. Even at the low flow rate of 1 µL/min, only the solution within 110 µm of the electrode out of the 700 µm tall channel has a chance to be captured while the remaining analyte is carried downstream. It should be noted that the Peclet number and depletion zone depend only on system dimensions and the diffusivity of the target analyte and are therefore indicative only of mass-transport related effects.

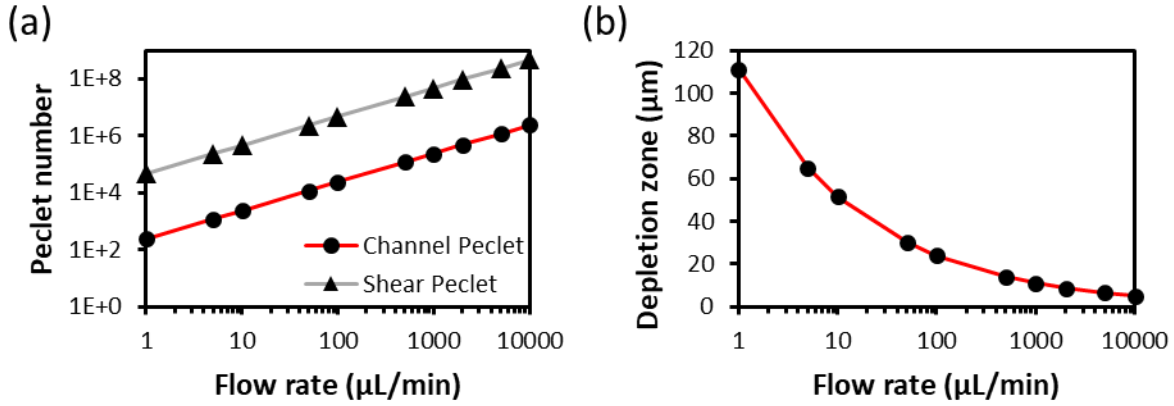

Figure 4-8. Numerical modeling of mass transport effects. *Dependence on flow rate is shown for (a) Channel and shear Peclet numbers, and (b) Depletion zone thickness.*

The effect of flow rate on capture kinetics of the system is shown in Figure 4-9. Collection rate increases with flow rate, however only weakly: a 10-fold increase in collection rate necessitates a 1000-fold increase in flow rate. The collection rate signifies the mass transport brought to the electrode surface and is therefore the upper limit for the electrode binding rate.

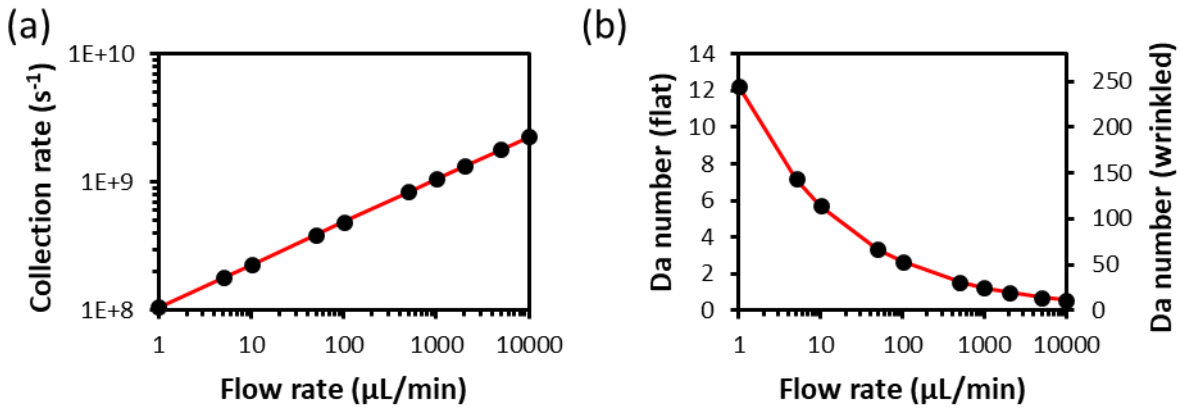

Figure 4-9. Numerical modeling of capture kinetics. *Dependence on flow rate is shown for (a) Upper limit of the collection rate, and (b) Damkohler number. Abbreviation – Da: Damkohler*

The Damkohler number, representing the ratio of the reaction rate to the mass transport rate, decreases with flow and indicates that the system is becoming a reaction limited regime when $\mathrm{Da} \approx 1$. Two sets of Damkohler numbers were obtained depending on the binding site density, with values corresponding to a planar electrode plotted on the primary vertical axis and the values for a wrinkled electrode plotted on the secondary vertical axis. The planar electrode

system is shown to reach a reaction limited regime ($\mathrm{Da} \approx 1$) at approximately 2000 µL/min after which increasing flow would no longer increase binding kinetics. The wrinkled electrode system however does not reach a reaction limited regime for the given flow rates and would benefit from further increases. The wrinkled electrode system would necessitate flow rates greater than 100000 µL/min to become reaction limited, at which point the system would be turbulent and the mathematical model would no longer apply.

The number and density of available binding sites, along with the association and dissociation constants, significantly influence the predicted behaviour of the system. For the flat electrode, the density of ssDNA probes used a value previously observed for thiol-bonded ssDNA [114]. In order to account for the 20x increased electrode surface area of the wrinkled electrode in the same geometric footprint as the flat electrode (as later discussed in Section 5.1.2), the binding site density for the wrinkled electrode was similarly increased by a factor of 20. It should be noted that the true flow behaviour of the system is likely to differ as a result of the 3-dimensional wrinkles. Additionally, the rate constants used were that of a 20 base pair strand under similar conditions however real-world behavior could deviate substantially [110]. Rate constants for DNA hybridization are difficult to predict and depend highly on factors such as binding site density, temperature, and presence of ionic species [115]–[117].

Overall, the results of the numerical modeling suggests that increasing the flow rate would increase mass-transport, leading the faster capture kinetics. For flat electrodes, an estimated optimal flow rate of 2000 µL/min was obtained. For wrinkled electrodes with a greater number of available binding sites, even higher flow rates are likely optimal.

4.3.2 Flow enhancement of ssDNA capture

To confirm the predicted increase in capture due to increased mass transport, LIT devices were subjected to flow of target solution. Tubes with 2 working electrodes were functionalized as described in Section 3.3.7 however using a modified 3 µM capture probe and 10 mM MCH concentration. SWV measurements were conducted according to Section 3.3.9 using a combination Ag/AgCl wire reference/counter electrode. At the time of the experiment, no adequate adhesive was found for sealing so the system was not able to support high flow rates.

As such, three flow rates were investigated as a proof-of-concept: 0 µL/min, 5 µL/min, and 50 µL/min. The experiment was performed at room temperature with an incubation time of 20 minutes, after which the current was measured. The current was normalized to the no flow case and the results are shown in Figure 4-10.

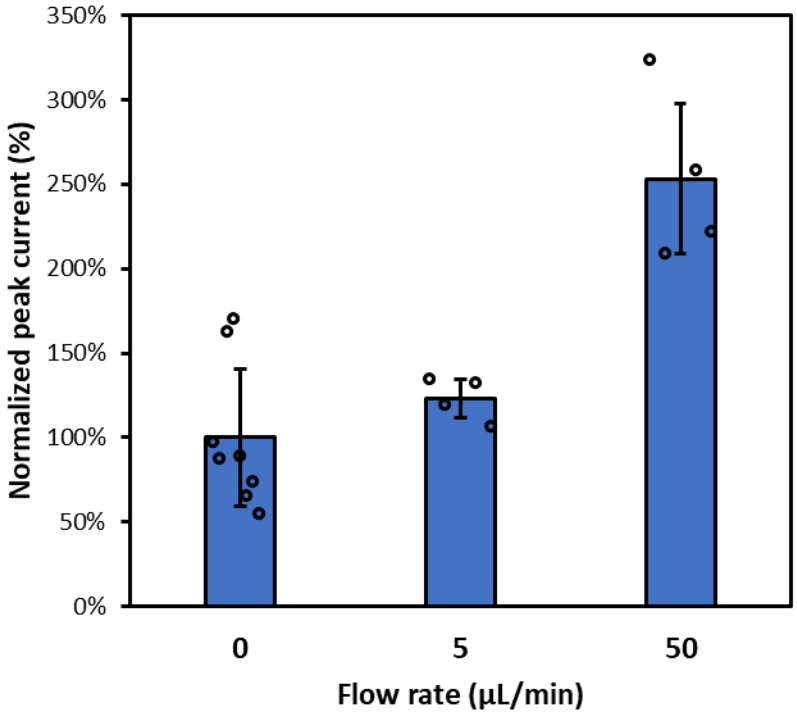

Figure 4-10. Flow enhancement of peak signal due to flow. *Tubes with two working electrodes functionalized with capture ssDNA (3 µM overnight, followed 10 mM MCH for 10 minutes) were incubated for 20 minutes with 100 nM reporter ssDNA at the given flow rate (non-recirculating). Square-wave voltammetry was performed in a solution containing 25 mM phosphate buffer solution with 25 mM NaCl versus a Ag/AgCl wire connected as both reference/counter electrode. All measurements and hybridization steps were conducted at room temperature. Current values were normalized to the average peak value of the no-flow measurements.*

The use of 50 µL/min flow resulted in a significant increase in peak current of 253% compared to the static case. This increase is attributed to the increased mass transport to the electrode surface. Without flow, the surface-bound capture probe relies on diffusion alone to bring the target ssDNA into sufficiently close proximity for hybridization. From equation (8), it can be estimated that only analyte within approximately 0.5 mm of the electrode surface could diffuse to the surface in the incubation time of 20 minutes, suggesting that a significant volume inside the 0.7 mm diameter tube did not have a chance to be captured.

Interestingly however, the 5 µL/min flow case was not statistically significantly different to the no flow case. The increased mass transport may have been insufficient to be distinguishable from the static scenario. It is possible that the effect would be perceptible at either low target concentrations (lowering the LOD) or high target concentrations (increasing the measured signal) however more investigation on the system's behaviour is required.

4.3.3 Optimization of capture probe concentration

The capture probe concentration was investigated to better obtain information on the system performance in subsequent experiments. Due to the high total surface area of the 3 electrodes inside of the tube and the limited volume of the enclosed space, relatively high ssDNA concentrations compared to prior work on screen printed electrodes were utilized to achieve proper coverage [118], [119]. A total of 3 capture probe concentrations were investigated: 4.5 µM, 6 µM, and 7.5 µM. These values were obtained from scaling similar ssDNA functionalization efforts on nanostructured planar electrodes, maintaining the amount of moles of ssDNA per square centimeter of electrode area [114]. Tubes were functionalized as described in Section 3.3.7, differing only in the deposited concentration of capture probe, and the results are shown in Figure 4-11.

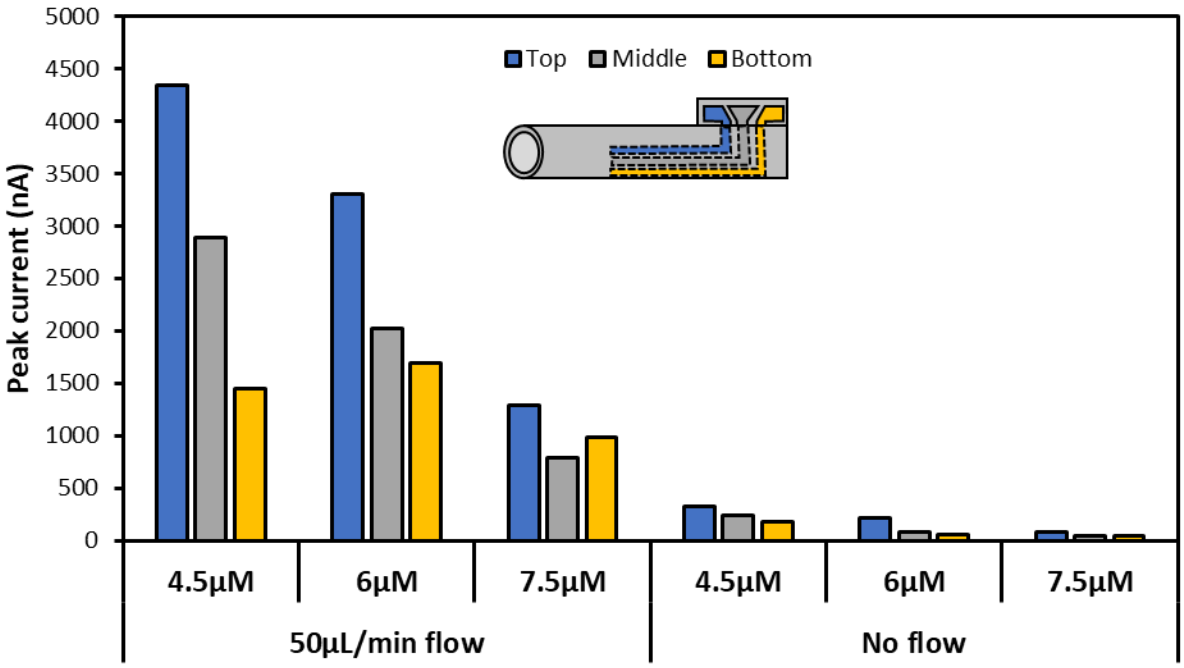

Figure 4-11. Comparison of capture probe concentration on measured peak current for 50 µL/min and no flow conditions. *LIT devices were functionalized with the given capture ssDNA concentration overnight and passivated with 100 mM MCH for 20 minutes. 130 nM reporter was introduced to the device at the specified flow rate. SWV was performed versus a Ag/AgCl wire connected as both reference/counter electrode. All measurements and hybridization steps were conducted at room temperature.*

The 4.5 µM concentration produced the highest peak current, followed in decreasing order by the 6 µM and 7.5 µM concentrations. This trend was applicable to both the 50 µL/min flow case as well as the static case. These results suggest that at the higher capture probe concentrations, fewer barcodes can hybridize with the capture probe, thereby producing less current. A likely explanation would be due to the steric hinderance and electrostatic repulsion caused by an overly dense capture probe layer. High amounts of capture probe immobilized on the surface would prevent barcode hybridization due to insufficient room caused by closely packed arrangement [75]. Further testing of device operation under flow was carried out using the 4.5 µM concentration as it resulted in the highest measured signal. Continued optimization using lower capture probe concentrations could further increase the degree of hybridization, but efforts were focused on assessing overall device performance under flow, as discussed in the next chapter.

Overall, testing and iterative design of the LIT device resulted of a flow-capable platform for use as a biosensor. Heat-shrink polyolefin substrates allowed for an 80% reduction in device size. Longitudinal working electrodes embedded in the tubing wall, combined with an inserted Ag/AgCl wire as reference and nanostructured gold wire as counter electrode, allows for the successful electrochemical detection of a flowing analyte. Numerical modelling suggests flow would result in increased capture of target nucleic acid sequences using flow rates up to several millilitres per minute, and preliminary testing of the device at 50 µL/min confirmed the enhancement due to mass transport.

5 Biosensor characterization and evaluation under flow

This chapter builds on the knowledge gained in the previous section and examines the biosensor's physical characteristics, electrochemical response, and biochemical capture performance under flow conditions. Physical characterization includes examination of the surface morphology by SEM, evaluation of the electro-active surface area, and assessment of electrode wettability. The electrochemical response of the bare sensor was investigated using Ferrocyanide/Ferricyanide redox couple solution and dopamine was used to evaluate sensor response for continuous monitoring applications. Finally, capture performance of ssDNA as a function of time and volume was investigated, under both pump-driven and vacuum-driven flow conditions. All electrochemical studies use the 3-electrode cell configuration with Ag/AgCl reference and nanostructured gold counter electrode as shown in Figure 5-1 unless otherwise specified.

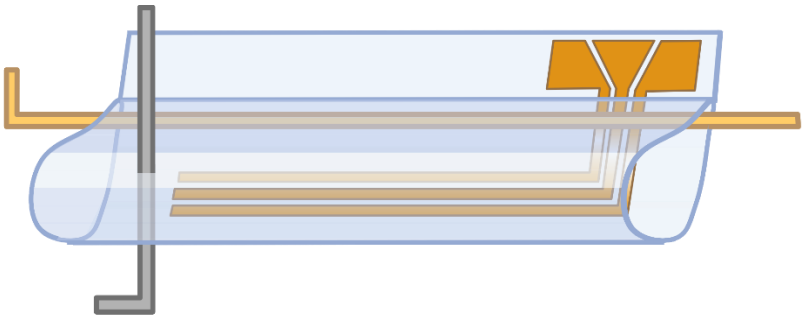

Figure 5-1. Primary LIT design used for characterization and performance evaluation. *The design consists of three longitudinal working electrodes, a Ag/AgCl reference electrode pierced through the tubing, and a nanostructured gold counter electrode inserted along the top of the tube parallel to the working electrodes.*

5.1 Physical characterization of the wrinkled electrodes

Physical characterization of the electrode was performed to obtain a better understanding the material properties and surface effects that influence biosensor performance. Capture and transport of biomolecules within a biosensor are influenced by the surface features of the electrode, while the surface area dictates the amount of material available for reaction, potentially leading to higher reaction rates and greater efficiency.

5.1.1 Scanning electron microscopy

The electrodes were first examined using SEM to gain qualitative insight on the surface topography. Imaging was conducted as described in Section 3.3.1. The working electrode images (Figure 5-2) show the expected hierarchical wrinkling pattern of metal thin-film buckling similar to the effect previously reported on heat-shrinkable polystyrene substrates [120], [121]. The wrinkled gold on polyolefin exhibits bi-axial wrinkling within the bulk of the electrode surface. The wrinkling effect can be observed spanning several orders of magnitude ranging from <1 µm to 100 µm features.

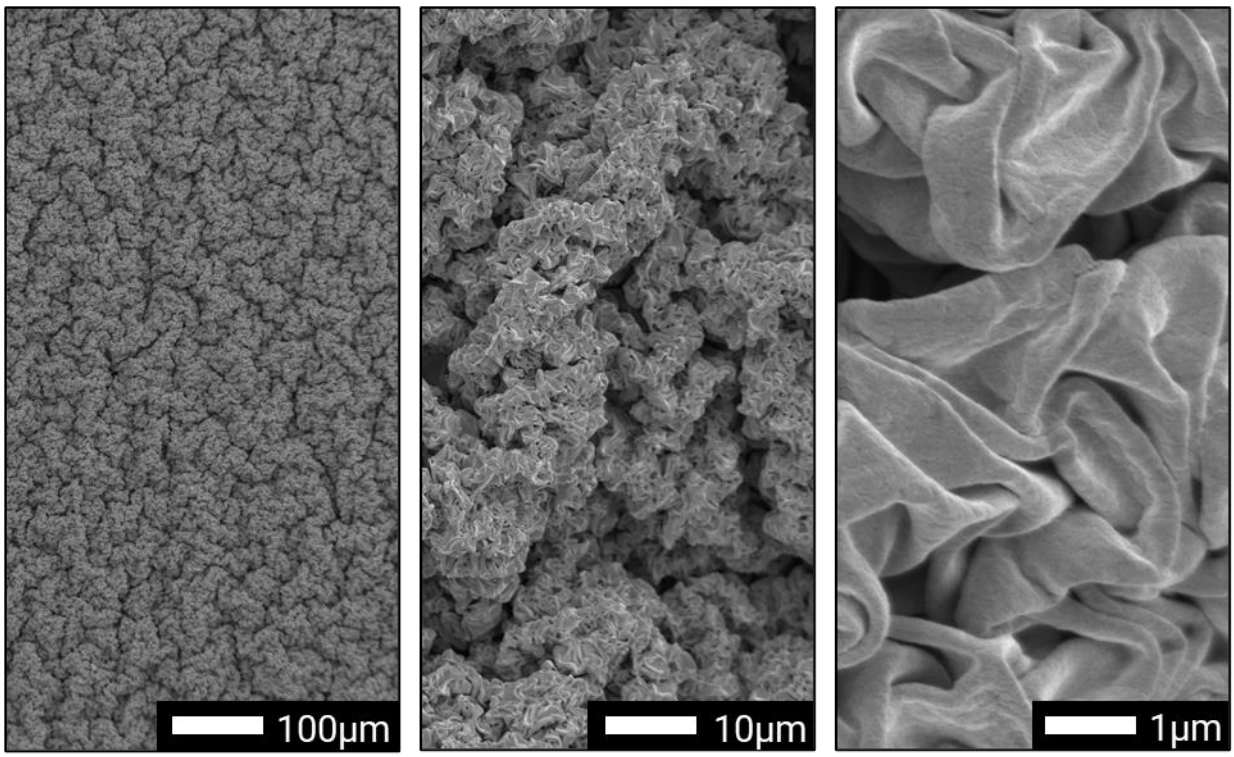

Figure 5-2. SEM images of the hierarchically wrinkled electrode morphology. *Electrodes consisting of a 40 nm gold layer on polyolefin buckle upon shrinking, resulting in wrinkles that span many orders of magnitude in size. From left to right, magnification is 100x, 1000x, and 10000x.*

Images of the prepared gold wire counter electrode reveals the surface area enhancing nanostructures (Figure 5-3). The electrodeposition parameters chosen (-0.2 V, 10 mM $HAuCl_4$) resulted in jagged, spike-like structures perpendicular to the wire surface. Previous studies have described the effects of deposition parameters on the nanostructure morphology [122]. The

coverage and size of the nanostructures provided an increased surface area without fragile, high-aspect-ratio features that would often break off during wire insertion into the LIT device.

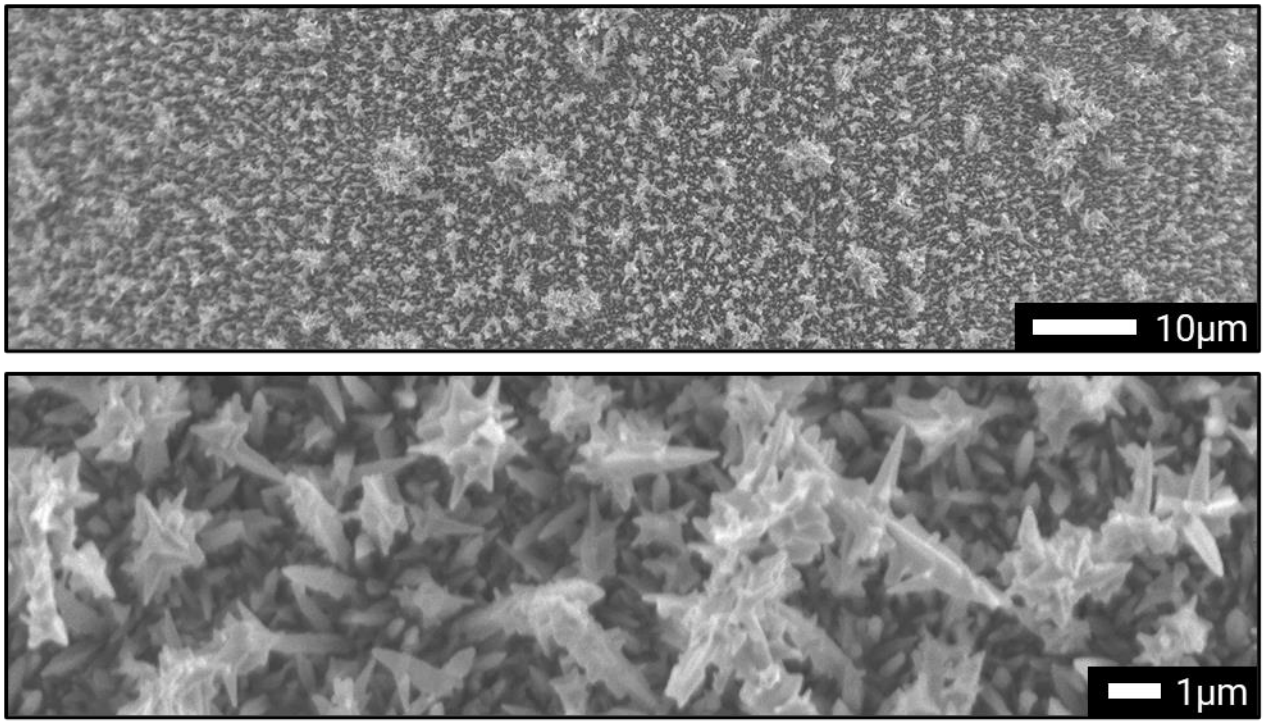

Figure 5-3. SEM images of nanostructured gold wire displaying high surface area features. *Surface modification was achieved by applying a constant -0.2 V potential in a solution containing 10 mM $HAuCl_4$ and 0.5M HCl. Image magnification is 1000x (top) and 10000x (bottom).*

The Ag/AgCl wire, used as reference electrode, displays a roughened texture with globular clusters on the wire surface (Figure 5-4). The electrochemical anodization of pure silver in a KCl bath resulted in a layer of approximately 1 µm silver chloride particles on the wire surface. Similar morphology has been observed when creating Ag/AgCl electrodes using a commonly employed bleach exposure technique [123].

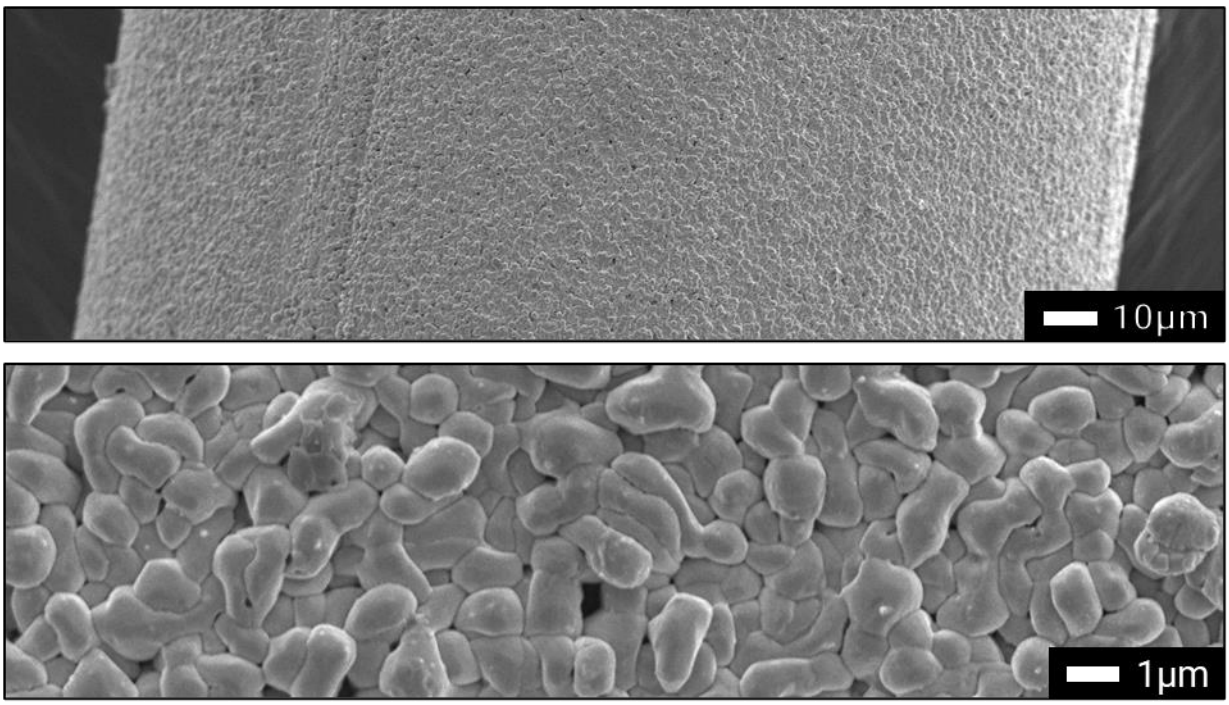

Figure 5-4. SEM images of the silver/silver-chloride wire showing globular silver chloride particles. *Surface modification was the result of a constant application of 25 µA·cm^{-2} in a solution of 1M KCl, allowing the chloride ions to interact with the silver surface. Image magnification of the vertically oriented wire is 500x (top) and 5000x (bottom).*

Considerable research has been conducted on understanding and controlling thin film buckling on elastomeric materials [124]–[127]. Amongst the simplest modifications can be achieved by changing the thickness of the deposited gold, altering the characteristic wavelength of the wrinkled surface [128]. Tunable electrode surface properties show promise to improve biosensor performance as morphology and porosity have a screening effect on biological molecules. Small pores can increase sensor performance *versus* large, non-specific targets by acting as a filter for particles larger than the pore opening [129].

In microfluidic systems, wall roughness can have a significant impact on the behavior of the fluid flow; however, optimization is complicated by inconsistent and contradictory results reported in literature [130]. Understanding the effects within microfluidic biosensors interacting with complex biological media is further complicated due to non-Newtonian behaviour of samples such as whole blood [131]. Optimization of wrinkle size would be beneficial on a per-target basis in complex media under well-established flow conditions.

5.1.2 Electro-active surface area

Cyclic voltammetry scans were performed to determine the electroactive surface area according to the method outlined in Section 3.3.3 and a representative sample scan of the 3 electrodes is shown in Figure 5-5. The electrodes display well-defined current peaks due to the oxidation of gold in the potential region of +1.0 V to +1.5 V and a reduction peak around +0.75 V. Differences in signal magnitude can be observed due to the varying electrode area within the tube, with the smallest area corresponding to the top electrode, and the largest area with the bottom electrode.

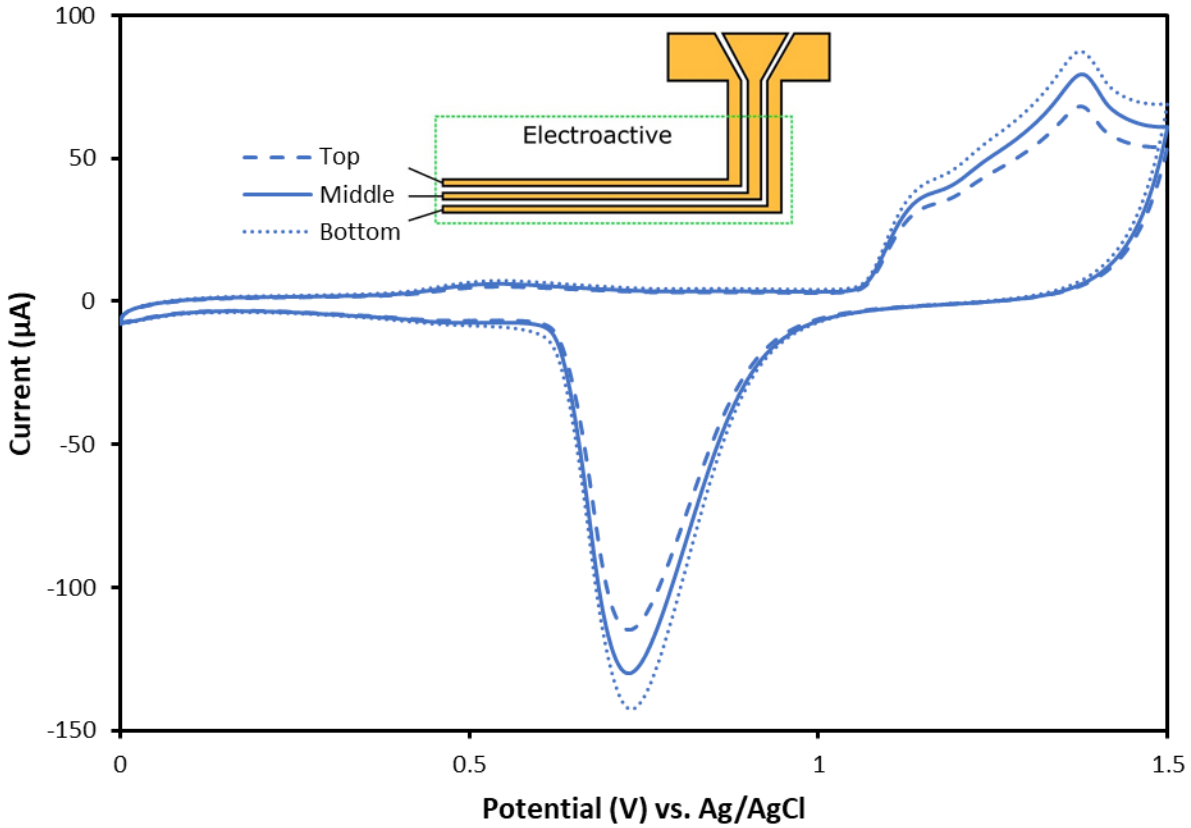

Figure 5-5. Representative cyclic voltammetry scans of the LIT electrodes in 0.1 M H_2SO_4 for determination of the electroactive surface area. *Peaks in the potential region of +1.0 V to +1.5 V signify the oxidation of gold while the peak around +0.75 V is the subsequent reduction of the surface. The area under the reduction curve was used for determination of the electroactive surface area. All measurements were conducted at room temperature.*

The electroactive surface area was calculated and compared to the geometric footprint to assess area enhancement. The area of the bottom electrode was chosen for comparison purposes and is shown in Figure 5-6. The geometric surface area of the before-shrinking electrode design was

0.797cm^2. Upon shrinking, the polyolefin film experiences an approximately 80% shrink in both dimensions, as confirmed using both manual caliper measurements of the entire device and electrode measurements on scale-calibrated optical microscope images. The resultant after-shrinking geometric footprint can therefore be estimated as $(1-0.8)^2 * 0.797 \approx 0.032$ cm^2, while the electroactive area was found to be 0.687 ± 0.049 cm^2. The surface area enhancement when comparing the electroactive surface area to the geometric footprint is $0.687/0.032 = 21.5$. Comparing the original before-shrinking footprint to the electroactive area, $0.687/0.797 = 0.86$, a 14% decrease is observed. This decrease in surface area can be attributed to the wrinkling process causing certain areas ('pockets') to be inaccessible to oxidation reaction, as previously described [120]. These calculations assume that the gold film is flat and uniform, however deposition conditions and underlying surface properties affect the roughness of the sputtered gold film [132]–[134].

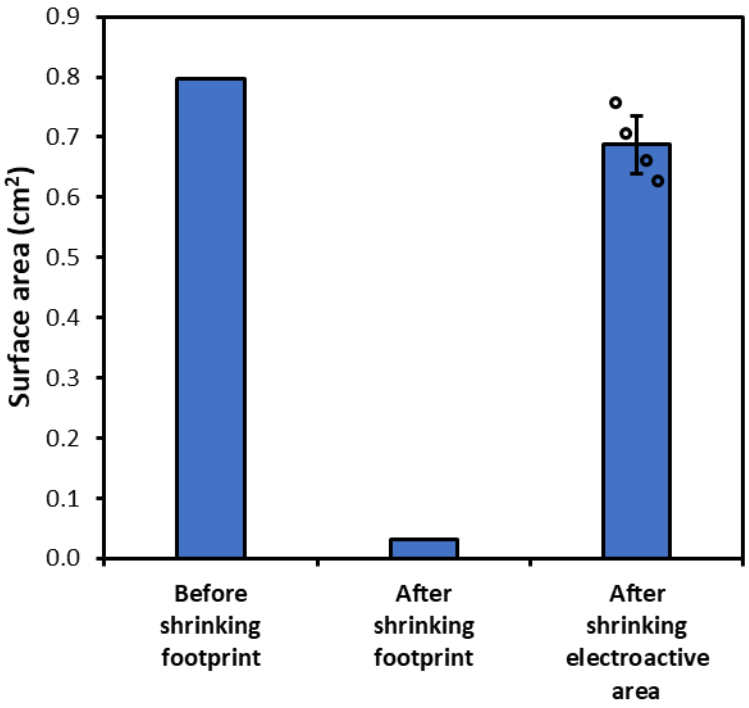

Figure 5-6. Comparison of geometric and electroactive surface area of the LIT electrodes. *The before shrinking footprint size is dictated by the chosen electrode geometry during the mask fabrication stage. Upon heat-shrinking of the substrate, electrode dimensions are reduced by approximately 80% as measured by optical microscopy. The electroactive area, calculated by integrating the area under the gold oxide reduction peaks during cyclic voltammetry, remains*

comparable to the original size, with a slight decrease attributed to inaccessible regions between wrinkles.

The use of a shrinkable substrate allows for a simple and effective method to fabricate high-surface area electrodes. The technique can be used to miniaturize feature dimensions beyond the that of the mask's fabrication technique limits. The shrink ratio is dependant on the polyolefin shrink properties, and the resultant wrinkle structure can be controlled by film thickness. Further enhancement of surface area can be achieved by techniques such as nanostructuring [135] or electrochemical roughening [94].

5.1.3 Electrode wettability

The rough morphology induced by the surface wrinkling alters the electrode wettability, potentially impacting its ability to interact with liquid samples. The degree of wettability is determined by the contact angle, which is the angle formed between the tangent line to the liquid-solid interface and the solid surface. A small contact angle indicates good wettability (hydrophilicity), where the liquid spreads over the surface and forms a thin film. A large contact angle indicates poor wettability (hydrophobicity), where the liquid forms droplets or beads on the surface and does not spread [136]. Figure 5-7 displays the hydrophobicity of a water droplet placed on a wrinkled gold surface.

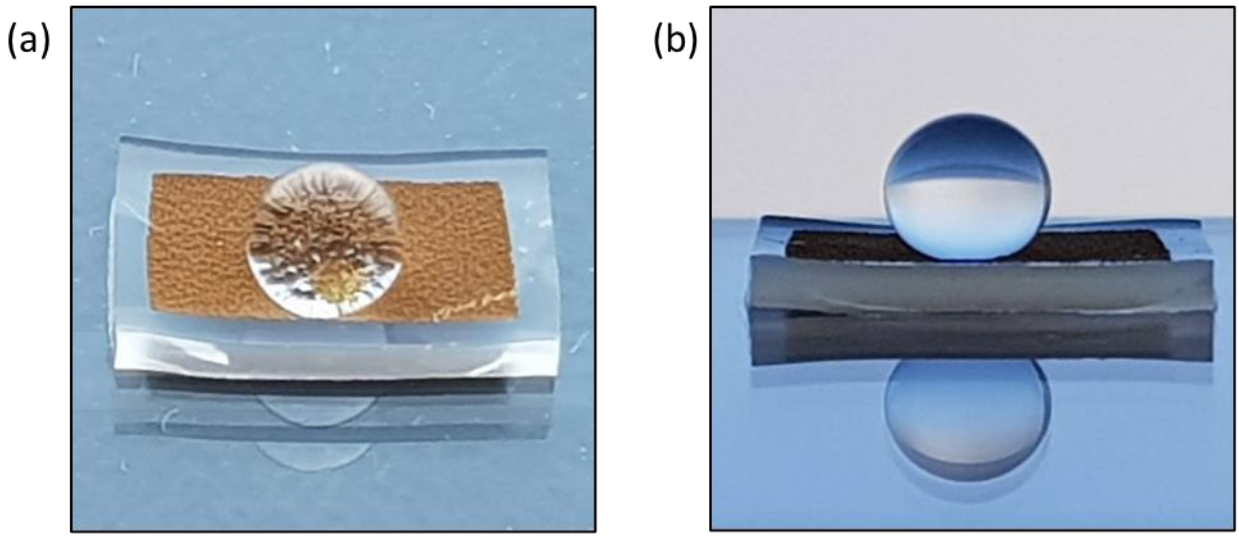

Figure 5-7. Sample images displaying high hydrophobicity of the surface using a water droplet placed on wrinkled gold without surface modification. *(a) 45-degree angle top-view, where the*

small area in contact with the surface can be seen through the liquid, (b) Side- view displaying the large contact angle.

To characterize the wettability, contact angle measurements of water droplets on the gold film were obtained as described in Section 3.3.2 at the various stages of electrode functionalization using both planar (non-shrunk) and wrinkled electrodes and the results are summarized in Figure 5-8.

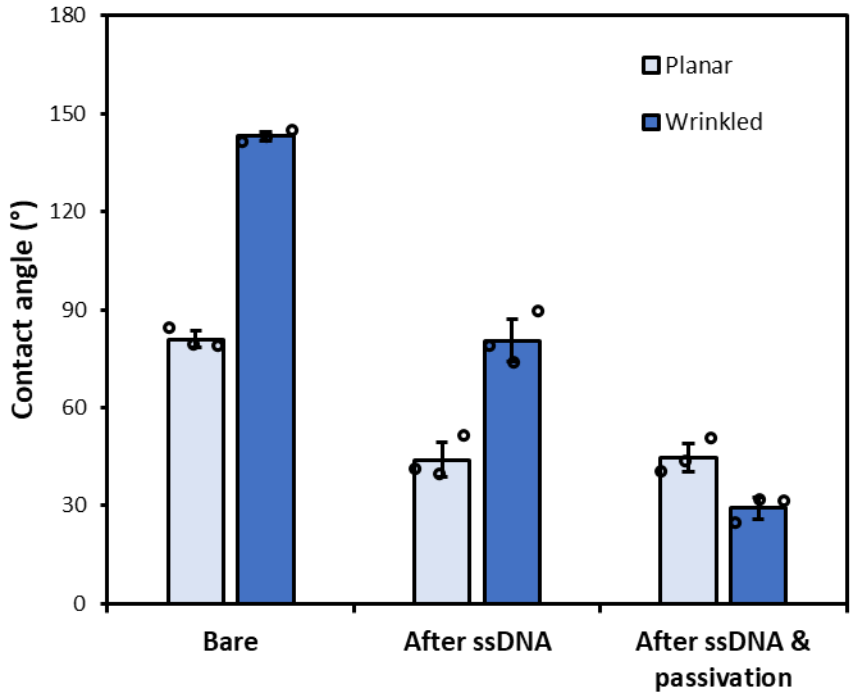

Figure 5-8. Evaluation of electrode surface wettability using water contact angle measurements performed at various stages of the biosensors functionalization for both planar (unwrinkled) and wrinkled electrodes. *Measurements were conducted at three stages relevant to the device fabrication process: after cleaning of the bare (unfunctionalized) electrodes, after the surface was modified overnight with 2.5 µM, 20 base pair capture ssDNA via thiol bonding, and after passivation of any remaining exposed surface using 10 mM MCH for 10 minutes.*

The increased hydrophobicity due to wrinkling is evident from the 143° contact angle obtained from the wrinkled surface versus the 81° observed on the planar surface. The effect is believed to be due to the inaccessible pockets of air trapped between the ridges of the wrinkles, as described by Cassie−Baxter or mixed Cassie-Wenzel models of wetting [137], [138].

Upon functionalization with the capture ssDNA, both surfaces become increasingly hydrophilic, with contact angles of 44° and 81°, for the planar and wrinkled surfaces, respectively. Following

passivation, the wettability of the planar electrodes does not change significantly. This is in contrast to the wrinkled surface which displays a further increase in hydrophobicity with a contact angle of 29°. SAM formation has been used to modify surface properties to control solvent-substrate interactions through a combination of end groups and changes in the nanoscale roughness of the surface [139], [140]. The SAM formed by ssDNA on the planar gold surface may have had a sufficient packing density to be unaffected by the addition of the smaller MCH whereas the wrinkled electrode experienced further increase in hydrophilicity from the addition of MCH.

These results indicate that the wrinkling of the electrode surface significantly increases hydrophobicity, to the potential detriment of a biosensor reliant on solvent-substrate interactions for efficient detection. Functionalization of the electrode surface however resulted in increased hydrophilicity, showing increased wettability over the non-wrinkled surface with the same surface modifications. Further investigation and optimization of the wrinkle structure and SAM formation should be pursued to improve biosensor performance, particularly for complex media necessitating anti-fouling properties. In particular, exploration of robust SAMs for continuous monitoring is needed such as through the incorporation of zwitterionic head groups to reduce baseline drift and increase system stability [141].

5.2 Electrochemical response under flow

Electrochemical characterization of the bare (non-functionalized) wrinkled electrodes was performed to better understand how the electrode morphology and flow of solution impact its ability to participate in electrochemical reactions. This information can then be used to understand and better control the biosensor's performance.

5.2.1 Ferrocyanide/Ferricyanide redox couple flow characterization

The effect of diffusion of redox species under static and flow conditions was assessed using Ferrocyanide/Ferricyanide redox couple solution. The electrodes were immersed in a solution containing 2 mM $K_3Fe(CN)_6$, 2 mM $K_4Fe(CN)_6$, and 25 mM Phosphate buffer, and cyclic voltammetry was performed from -0.3 V to 0.5 V while varying scan rate from 10 mV/s to 200

mV/s and flow rate from 0 µL/min to 100 µL/min. A subset of the study results is shown in Figure 5-9.

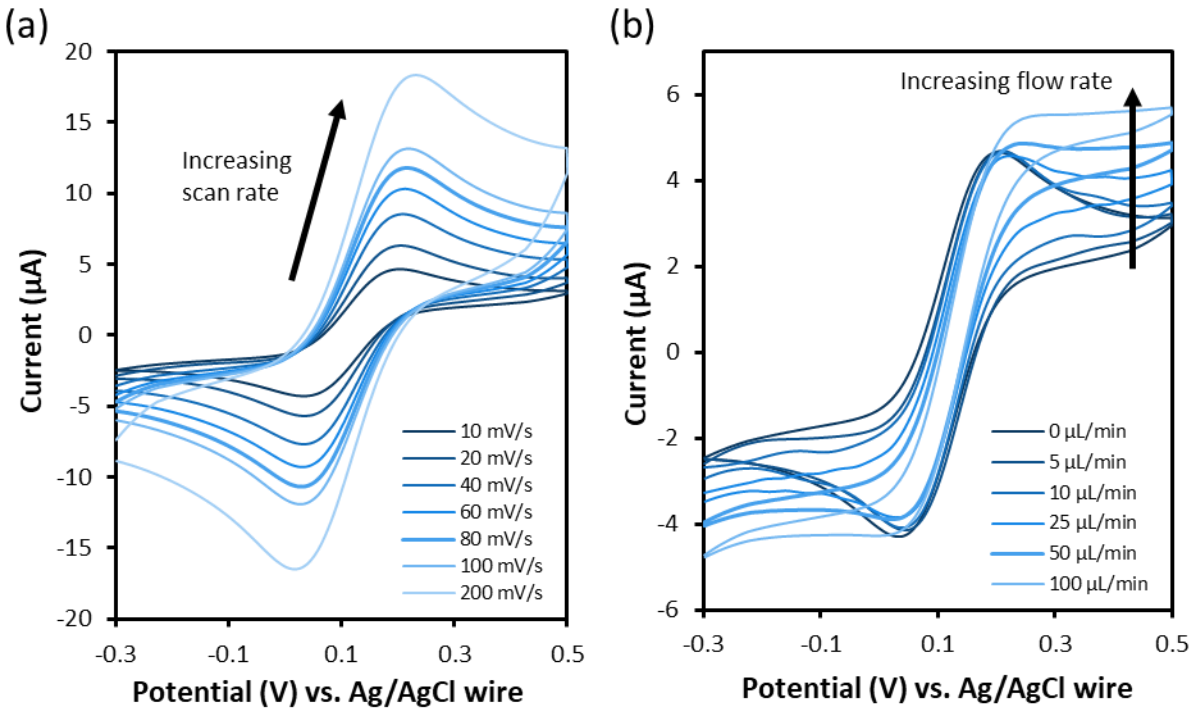

Figure 5-9. Cyclic voltammetry curves of bare (unfunctionalized) electrode surfaces to assess electron transfer rates under flow conditions. *A redox capable solution consisting of 2 mM $K_3Fe(CN)_6$, 2 mM $K_4Fe(CN)_6$, in 25 mM Phosphate Buffer was used to for (a) No flow (0 µL/min) scan rate study, (b) Flow rate study at 10 mV/s scan rate. All measurements were conducted at room temperature.*

The cyclic voltammetry scans in Figure 5-9 (a) show the expected 'duck-like' oxidation and reduction peaks resultant of the electron transfer of the Ferrocyanide/Ferricyanide solution [30]. A peak-to-peak separation of approximately 150mV was obtained, whereas the theoretical value for a single-electron transfer at 25°C is 57-59mV [27], [30]. The lack of adequate ions in the supporting electrolyte could induce ohmic drop, resulting in increased peak-to-peak separation [35], [142]. Addition of sufficient electrolyte (such as of 100mM NaCl or KCl) would decrease the solution resistance and bring the experimental results closer to the theoretical value.

The peak magnitude is shown to vary with scan rate, as indicated by the Randles-Sevcik equation [30].

$$i_p = 0.446nFAC_{bulk}\left(\frac{nFvD}{RT}\right)^{\frac{1}{2}} \quad (18)$$

Where i_p is the peak current (A), n is the number of electrons transferred during the redox event, F is the Faraday constant (C·mol^{-1}), A is the electroactive surface area (cm^2), C_{bulk} is the bulk concentration of the analyte (mol·cm^{-3}), v is the scan rate (V·s^{-1}), D is the diffusion coefficient (cm^2·s^{-1}), R is the gas constant (J·K·mol^{-1}), and T is the temperature (K).

For a planar diffusion case (no flow), the Randles–Sevcik equation indicates that the peak current should be linearly proportional to the square root of the scan rate [30]. This linear dependence indicates that the system is under a diffusion-controlled regime. Plotting the peak current versus the square root of the scan rate in Figure 5-10, a linear relationship for both the anodic (R^2=0.997) and cathodic (R^2=0.983) peaks was observed, suggesting the system is diffusion limited under no-flow conditions.

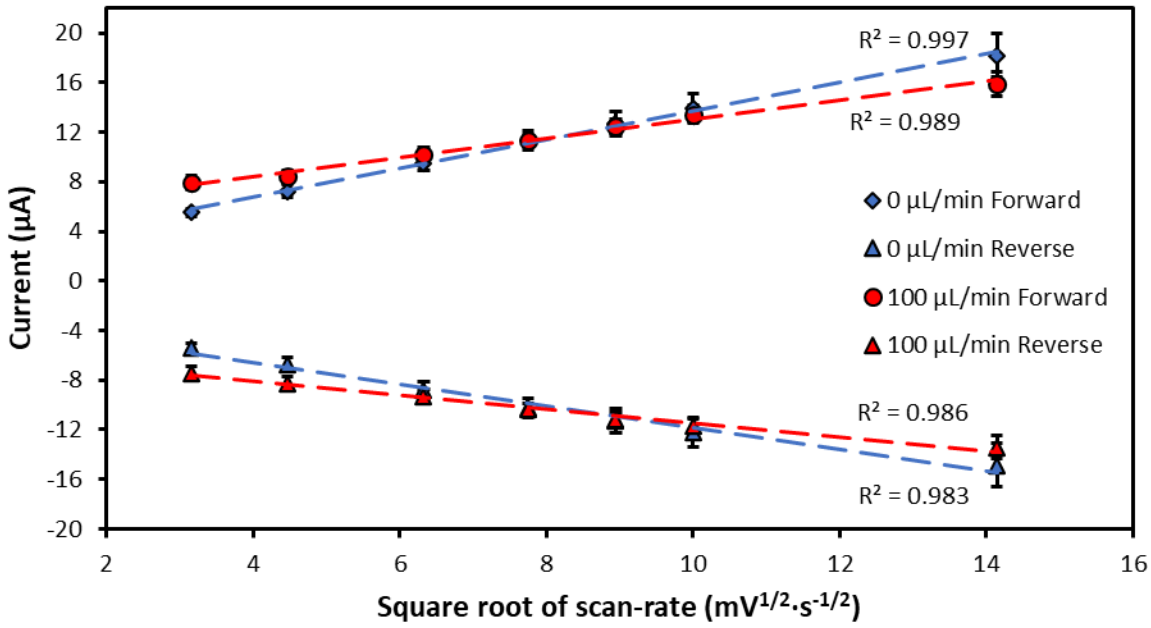

Figure 5-10. Plot of peak current vs. square root of scan rate to assess electron transfer regime according to the Randles–Sevcik equation. *Both forward and reverse peak magnitudes for the 0 µL/min and 100 µL/min flow rates were highly linear, suggesting a diffusion limited regime.*

The Randles-Sevcik equation assumes linear diffusion ('freely diffusing') which is only applicable for non-flow applications [29]. Under hydrodynamic conditions, the current can be better explained by the Levich equation, which describes the limiting current of an oxidation/reduction reaction at a rectangular electrode inside a flowing channel [143][144].

$$\boldsymbol{I_{\mathrm{LIM}} = 0.925nFC_{bulk}D^{2/3}V_f^{1/3}(h^2d)^{-1/3}wx_e^{2/3}}$$

(19)

Where I_{LIM} is the limiting current (A), V_f is the volumetric flow rate ($cm^3 \cdot s^{-1}$), h is the half the channel height (cm), d is the width of the channel (cm), w is the width of the electrode perpendicular to the direction of flow (cm), and $x_e$is the length of the electrode in the direction of flow (cm).

Figure 5-9 (b) shows the current response of the FOCN/FICN couple under flow conditions ranging from 0 µL/min to 100 µL/min. As flow increases, the distinct reduction/oxidation peaks become less pronounced and instead the curve approaches a sigmoidal shape. This is particularly apparent for the 100 µL/min flow case, where the peak is effectively eliminated. The Levich equation does not describe the phenomena that occurs at low flow rates where natural convection within the solution is an appreciable fraction of forced convection due to flow [143]. Interestingly however, plotting the results of the 100 µL/min flow in Figure 5-10 still results in a linear relationship for both the anodic (R^2 = 0.989) and cathodic (R^2 = 0.986) peaks. As the LIT system was operated under low-flow conditions not defined by either the Randles-Sevcik or Levich equations, proper interpretation is difficult and may be more suitably explained by simulation.

Due to the periodic nature of the peristaltic pump used to circulate the solution, oscillations could be observed in the resultant measurement signal (Figure 5-11). A custom MATLAB script utilizing a Savitzky–Golay filter was written to smooth the data and extract the peak information. Improvements could be made to obtain more reliable data by refining implementation of the signal processing algorithm or simply the use of a larger volume of the (inexpensive) solution injected by a syringe pump to avoid the oscillations in flow.

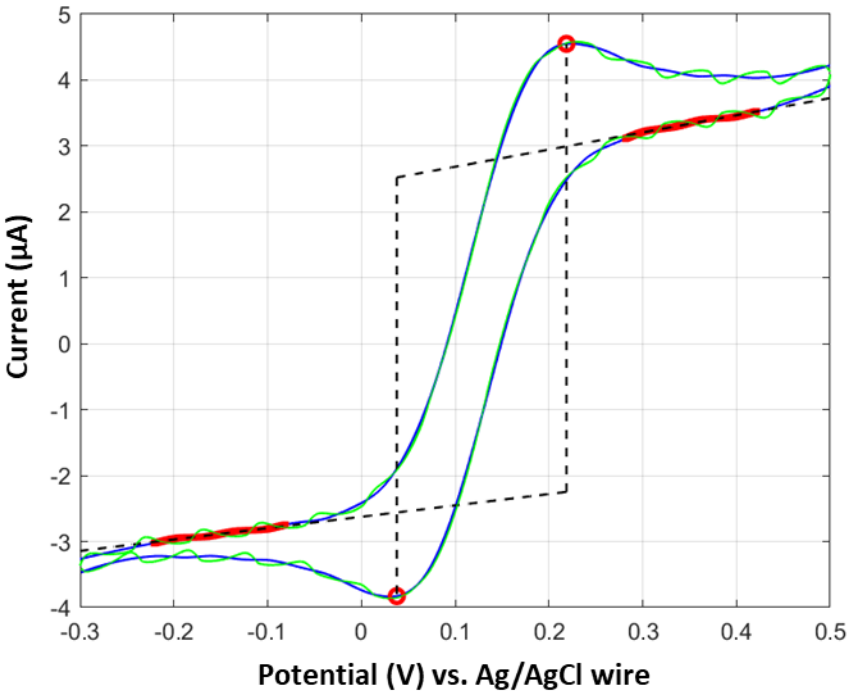

Figure 5-11. Sample cyclic voltammetry measurement during flow demonstrating periodic oscillations due to peristaltic pump. *The original curve (green) shows fluctuations, particularly in horizontal areas. Savitzky–Golay filtering was applied to remove the oscillations (blue curve), allowing for baseline region extraction (red curve) and subsequent identification of peaks (red circles).*

The results of the ferrocyanide/ferricyanide redox couple flow characterization suggest that the system operates under a diffusion-controlled regime at low flow rates. Approaching 100 µL/min, the system appears to transition towards a transport-limited regime better explained by the Levich equation, where the current response is related to the volumetric flow rate. Repeating the experiment with higher flow rates would allow for a better understanding of the transition between diffusion-limited and transport-limited flow regimes, and therefore better optimization of the system. By modifying the inner diameter of the system, it is possible to achieve different flow velocities for the same volumetric flow rate, allowing control over the desired regime depending on the desired application.

5.2.2 Electrochemical detection of dopamine

Dopamine, a neurotransmitter frequently studied for its role in motor function, motivation, and response-reward stimulus [145], was used as a target for a continuous monitoring system using

the LIT device. Dopamine is capable of reducing and oxidising without the use of additional redox couples or enzymes [146]. As such, the detection can be carried out directly from a bare (unfunctionalized) electrode surface.

A sample chronoamperometry scan for the detection of dopamine is shown Figure 5-12 using the protocol described in section 3.3.4. Each injection of solution results in a spike in current, which quickly decays to a baseline value. The value of the decayed current increases with the dopamine concentration and returns to its original baseline upon removal of the target.

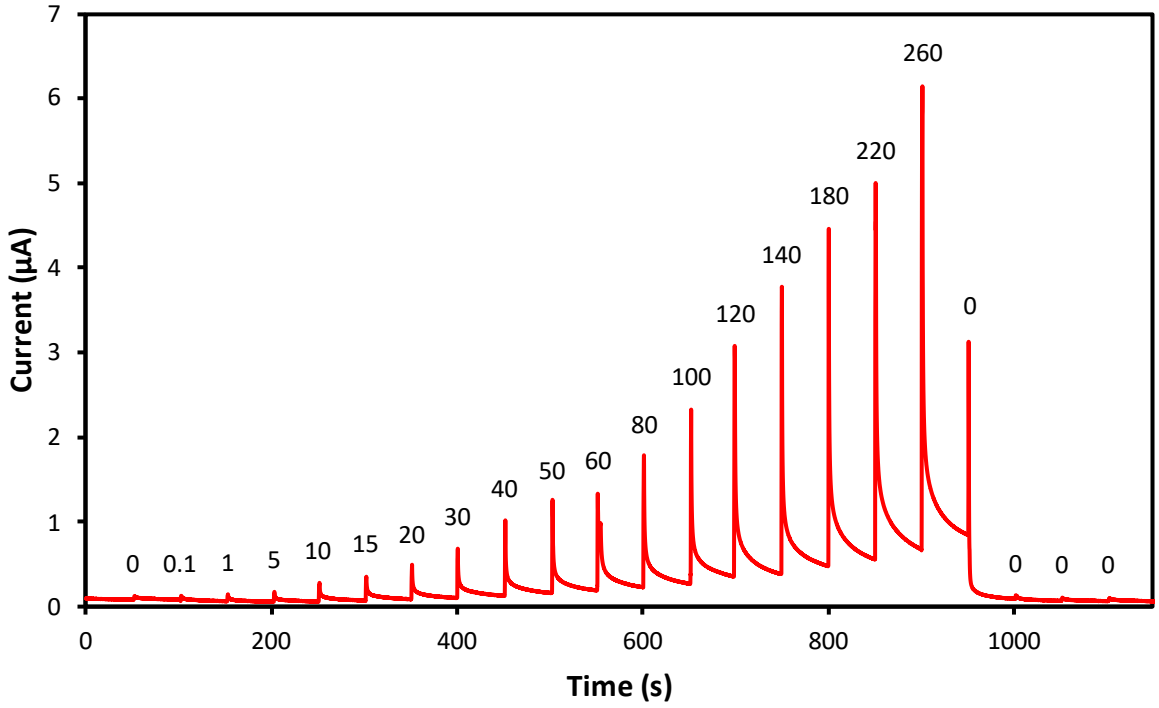

Figure 5-12. Sample chronoamperometry signal response of bare electrodes with serial injections of 0 to 260 µM concentration of dopamine. *A constant potential of 0.3 V vs. Ag/AgCl wire acting as both reference and counter electrode was maintained while 50 µL of varying concentrations of dopamine was injected using a pipette at 50 second intervals. The oxidation of dopamine resulted in a measurable increase in current, proportional to the injected concentration. All measurements were conducted at room temperature.*

Even in the blank solution, a slight spike can be observed before the current decays back to the baseline. This is believed to be the result of the sudden flow of injected solution momentarily increasing mass transport of ions to the electrode. Additionally, the Ag/AgCl wire may have been disturbed during injection from the physical contact of the pipette tip, contributing a noise-like

spike in current. A volume of 50 µL was used to ensure a complete exchange of solution within the 10 µL volume of the LIT device.

In order to avoid any influence of the solution velocity from the manual injection, current values after 50 seconds were taken for measurement. The process was repeated using all 3 electrodes inside a tube and the results are shown in Figure 5-13.

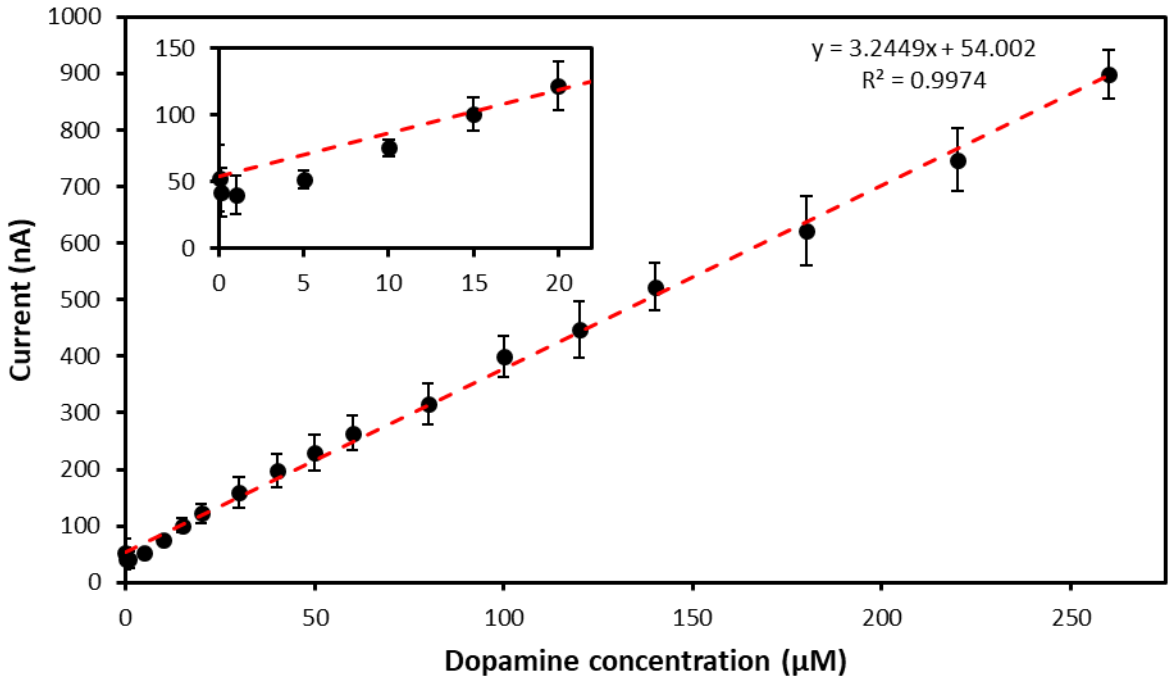

Figure 5-13. Calibration curve from sequential injection of 50 µL of dopamine into the LIT device. *A linear correlation between dopamine concentration (0 - 260 µM) and the measured current after 50 seconds is obtained. Inset: magnified view of the lower concentration range (0 - 20 µM). All measurements were conducted at room temperature.*

A highly linear correlation was obtained within the tested range of 0-260 µM ($y = 3.2449x+54.002$, $R^2 = 0.9974$) with a LOD of 18.76 µM, using the method described in Section 3.4. Physiological dopamine concentration varies depending on the region of the body, with circulating dopamine found in concentrations ranging from 10 pM to 10 nM [147]. As such, the LIT device would need further improvement for use as a biosensor for circulating dopamine. However, this detection limit obtained is in the same order of magnitude as the work by authors Kim et al. who demonstrated a LOD of 5.83 µM using cylindrical gold nanoelectrodes [146].

Concentrations in the nanomolar range were achieved by Kagie et al. with a 530 nM LOD using tube-based implantable biosensor [93], while Atta et al. attained a detection limit of 0.6 nM with an electrode modified with an ion-selective synthetic polymer and gold nanoparticles [148].

These results show promise of the LIT device as a continuous or pulsed monitoring biosensor. Additional enhancement would be obtained by minimizing the surface fouling of the electrode as a result of the oxidation and subsequent adsorption of dopamine [148]. The use of biological fluids introduces interference, particularly from ascorbic acid and uric acid due to overlapping detection signals from the similar redox characteristics [148]. Furthermore, the use of chronoamperometry for detection in complex media may not be advisable due to its constant potential. Instead, techniques that involve varying the potential could be used to help repel adsorbed species between measurements.

5.3 Affinity-based biosensing using DNA:DNA systems

This section reports the LIT's ability to capture and detect a ssDNA strand as a target analyte. As affinity-based biosensors are the key to developing highly sensitive and specific devices for continuous monitoring, such an approach provides a simplified system to assess performance over more complex samples. The results of capture kinetics under flow, evaluation of biosensor response under fixed volume and time constraints, and assessment of limit-of-detection as well as repeatability are presented. These results contribute to a better understanding of the working principles of the affinity-based biosensor operated inside the LIT system and its potential as a reliable tool for the detection and quantification of analytes.

5.3.1 Capture kinetics of ssDNA under flow

In order to assess the feasibility of device operation for a wide variety of medical tubing applications, compatibility with high flow rates as well as both short- and long-duration assays were evaluated. Preliminary flow experiments in Section 4.2.3 using the initial device design showed promise of increased capture for flow compared to static conditions. The sealing of the LIT device allowed for operation at higher flow rates without leaks or bubble formation, supporting the ability to conduct longer assays under high flow conditions.

A 500 µL sample of 100 nM target ssDNA was made to recirculate at 2000 µL/min using a peristaltic pump as described in Section 3.3.5. Initial measurements were conducted in non-flowing solution containing 25 mM phosphate buffer and 25 mM NaCl, and upon introduction of the target, measurements were performed at 5-minute intervals in the flowing target solution.

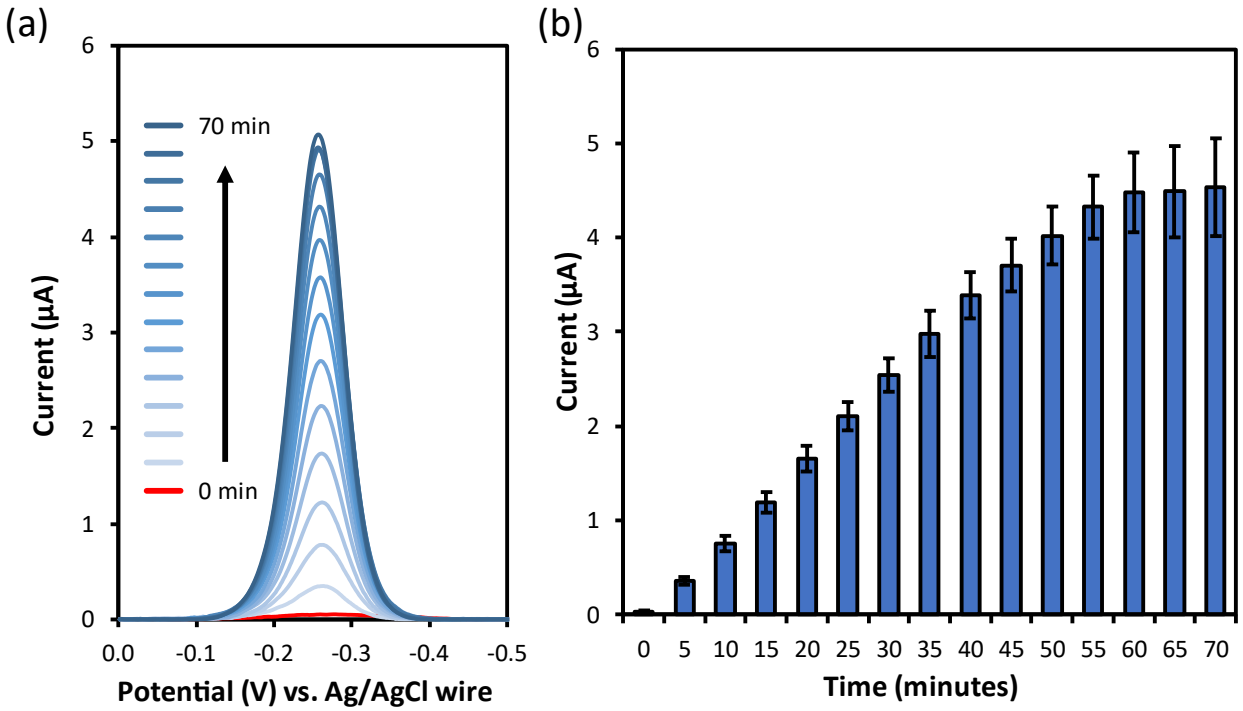

Figure 5-14. Capture kinetics of ssDNA under recirculatory flow. *A volume of 500 µL of 100 nM reporter ssDNA was recirculated at 2000 µL/min. (a) Representative square wave voltammetry response of hybridized ssDNA with methylene blue redox label. Signal processing included background subtraction and smoothing to remove noise. (b) Corresponding magnitude of peak current for each measurement time-point. All incubations and measurements steps were conducted at room temperature.*

The results of the high-flow testing are shown in Figure 5-14. The LIT device withstood the duration of the experiment (70 minutes) without leak in either the polyolefin seal-line or at the inlet/outlet connections. The measured current shows a near linear increase with time till approximately 60 minutes, after which the signal plateaus. As the signal after 5 minutes (363±40 nA) was significantly higher than the pre-target current (29±19 nA), this suggests that the device is capable of detection at lower-concentration and/or shorter-duration at the tested flow rate of

2000 µL/min. Modification of the capture probe packing density could be done to achieve faster capture (discussed in Section 2.2.4).

5.3.2 Effect of flow rate on device performance under fixed time and fixed volume constraints

Next, the influence of flow rate on the LIT device is examined to determine the effect of flow rate for capture of ssDNA. As flow allows for higher volumes of target (and therefore, higher number of target molecules) to interact with the sensor surface over a given time, it is difficult to determine the role of each factor on the resultant signal. For this purpose, two experiments were conducted to examine the significance of flow rate on device performance. The first involves performing a measurement after a fixed time, allowing varying amounts of solution volume to pass the electrode surface. The second experiment involves flowing a fixed volume of target solution and measuring the signal. For both tests, flow rates of 10, 100, 500, and 2000 µL/min were evaluated using 500 µL of recirculating 100 nM target ssDNA as described in Section 3.3.5. Solution flow was paused during the measurements to reduce the impact of additional target solution on sequential measurements.

In addition, polyT ssDNA with methylene blue and the same number of bases was used as non-complementary sequences to verify non-specific adsorption and the influence of in-solution redox events for both the low (10 µL/min) and high (2000 µL/min) flow rates. The proximity of methylene blue in solution near the surface or temporarily adsorbed during measurements could participate in the redox reaction (described in sections 2.1.2 and 2.2.3) and incorrectly be attributed to hybridization.

Signal enhancement was observed with increasing flow rate for the 20 minute fixed time trial, as shown in Figure 5-15. All flow rate measurements showed successful capture of the target ssDNA, as shown by a signal increase versus the averaged pre-target signal (calculation described in Section 3.4.1). Compared to the 10 µL/min flow rate, there is a 3.81-, 20.64-, and 31.25-fold change for the 100, 500, and 2000 µL/min flow rates, respectively. For the non-complementary target, a non-statistically significant signal decrease was observed for the at 10 µL/min flow rate. This may be in part due to surface contaminants present in the pre-target measurement, which were partially removed during flow. The 2000 µL/min, non-complementary condition

experienced a signal increase compared to the pre-target measurement, however the resultant signal magnitude was approximately 5% that of the complementary target at the same flow rate. The effects of non-specific adsorption or the increased mass-transport of flowing, non-hybridized target near the electrode surface could explain the slight signal increase observed at the 2000 µL/min flow rate. Overall, however, the comparatively small signal of the non-complementary target at both the low and high flow rates suggests that increased hybridization of the target due to flow is responsible for signal enhancement.

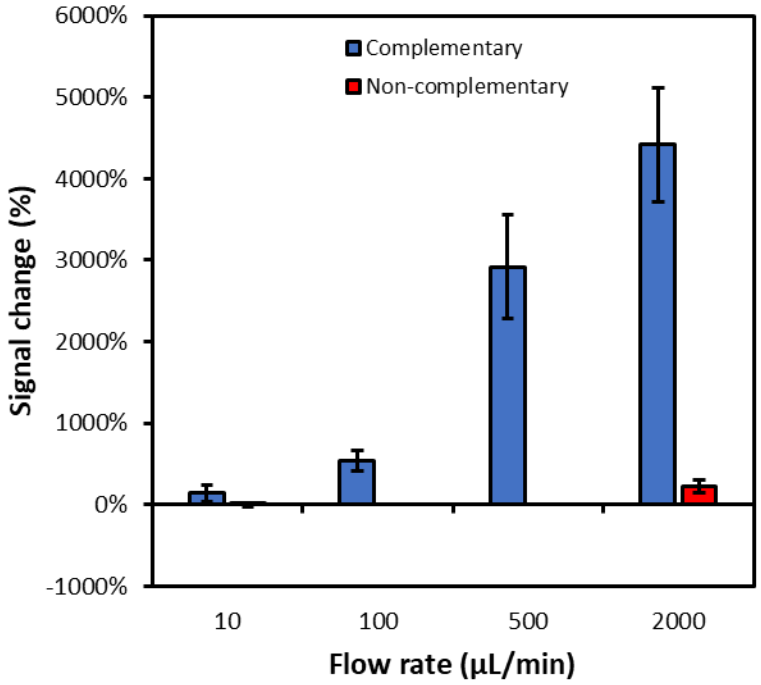

Figure 5-15. Effect of flow rate on signal for fixed time constraint. *A volume of 500 µL of 100 nM ssDNA was recirculated at the specified flow rate for 20 minutes. A SWV measurement was then performed in the target solution to determine the amount of hybridization that occured for different flow rates. To assess the influence of the unbound ssDNA in solution on the resultant signal, both complementary (all flow rates) and non-complementary (10 and 2000 µL/min flow rates) sequences were tested. All incubations and measurements steps were conducted at room temperature. Signal change was calculated as the difference of the pre-target and post-target measurements, divided by the original pre-target value.*

To verify the if the signal enhancement was due to the increased volume of target solution, measurements were performed after 500 µL of target flowed through the device and the results are shown in Figure 5-16. Despite the experiment duration spanning orders of magnitude from 50 minutes to 15 seconds, the signal change compared to the average pre-target signal did not

significantly differ between the tested flow rates. These results suggest that the increase in volume, and therefore number of target molecules, passing through the device is largely responsible for the signal enhancement. Similar to the fixed-time study, the presence of target in solution near the electrode surface or non-specifically adsorbed did not appreciably contribute to the measured signal, as a slight decrease in signal was observed with the non-complementary sample at both the 10 and 2000 µL/min flow rates.

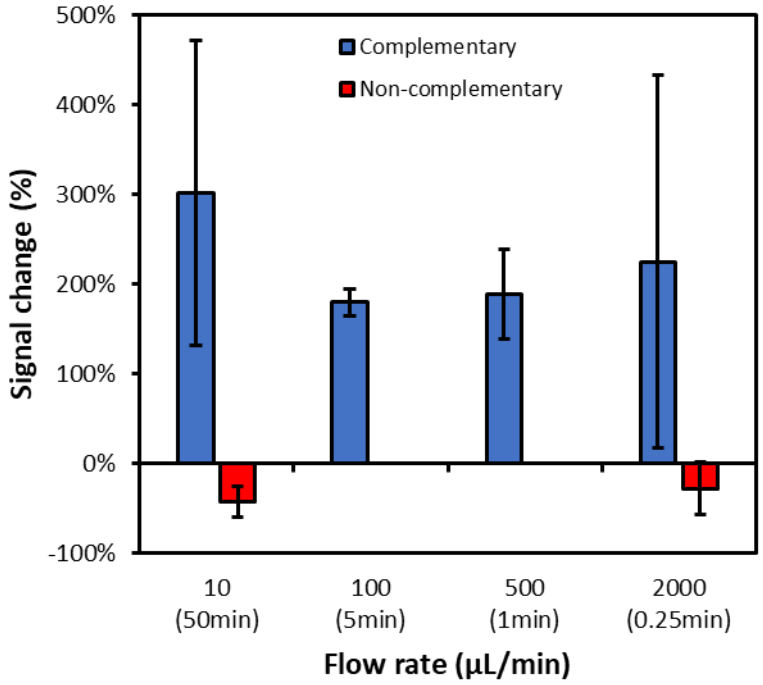

Figure 5-16. Effect of flow rate on signal for fixed volume constraint. *A volume of 500 µL of 100 nM ssDNA was made to flow at the specified flow rate until the entire volume passed through the device. A SWV measurement was then performed in the target solution to determine the amount of hybridization that occurred for different flow rates. To assess the influence of the unbound ssDNA in solution on the resultant signal, both complementary (all flow rates) and non-complementary (10 and 2000 µL/min flow rates) sequences were tested. All incubations and measurements steps were conducted at room temperature. Signal change was calculated as the difference of the pre-target and post-target measurements, divided by the original pre-target value.*

The large standard deviations present at both the 10 and 2000 µL/min flow rates make it difficult to draw further conclusions without further investigation or statistical analysis. Repeating this experiment would aid in conclusively determining the role of sample volume and flow rate.

5.3.3 Blood collection tube limit-of-detection and repeatability

The use of a blood collection tube utilizes existing, low-cost equipment to generate flow instead of a pump. This solution is particularly attractive as an option for point-of-care diagnostics due to its compatibility with well-established blood collection techniques. To test the LIT device with a blood collection tube under such conditions, the system must handle high flow rates of several millilitres per minute while maintaining diagnostic ability at clinically relevant concentrations.

A combination study was utilized to test both the system's limit-of-detection and repeatability under blood collection tube-induced flow conditions. A 6 mL solution of ssDNA target, sufficient to fill the blood collection tube, was prepared for each of the following concentrations: 0.1 nM, 1 nM, 10 nM, and 3 sets of 100 nM. The system was configured and operated as described in Section 3.3.6, with an average flow rate of 2000 µL/min over the course of the 3-minute aspiration. The results of the blood collection tube aspiration is shown in Figure 5-17.

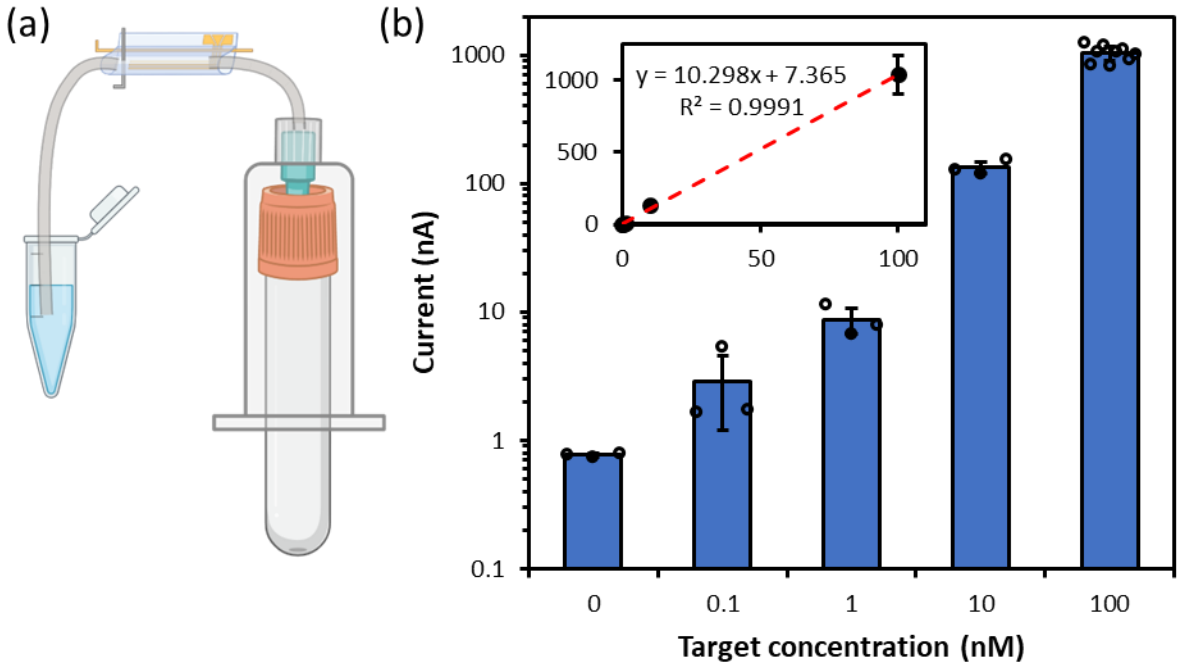

Figure 5-17. Study of LIT system operation using blood collection tubes for pressure-driven flow. *A 6mL sample of reporter ssDNA at the specified concentration was allowed to flow through the device into the blood collection tube (a), taking approximately 3 minutes. (b) Peak currents obtained from SWV measurements in 25 mM NaCl and 25 mM Phosphate buffer in response to*

various concentrations of reporter ssDNA. Inset: calibration curve with linear trend. All incubations and measurements steps were conducted at room temperature.

Utilizing the blood collection tube for flow, the system demonstrated a highly linear correlation between resultant signal and tested concentration ($y = 10.298x+7.365$, $R^2 = 0.9991$) with a LOD of 0.54 nM, using the method described in Section 3.4.

Despite the fast test conditions, device to device variability remained low, as shown by the results from individual electrodes within the tubes challenged with 100 nM target (Figure 5-18). The average current across all electrodes was 1035 nA with a standard deviation of 135 nA, resulting in a Relative Standard Deviation (RSD) of 135/1035=13.1%. When comparing across electrodes sharing the same position however, the top position exhibited a RSD of 4.0% (1186±47 nA), the middle electrode 5.4% (871±47 nA), and bottom 2.1% (1048±22 nA). The low variability between electrodes in the same position indicates that the devices have highly reproducible responses under fast flow. These results are very promising for incorporation into existing medical tubing such as with blood collection tubes (10-100 mL/min) [149] or dialysis (100-1000 mL/min) [150], [151].

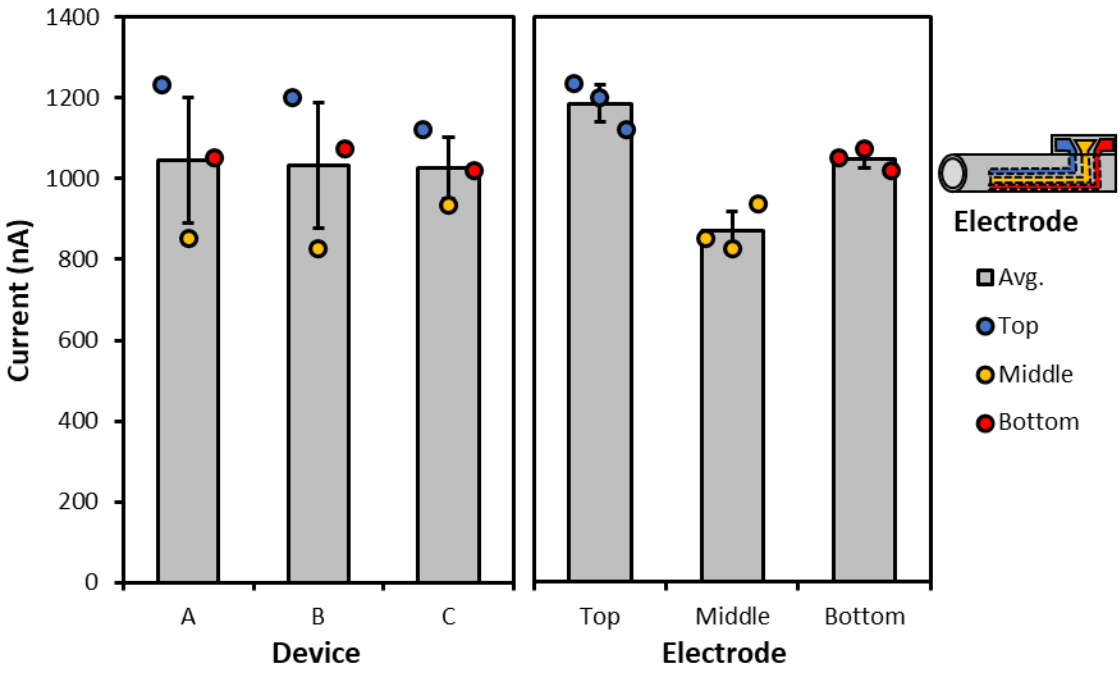

Figure 5-18. LIT device repeatability test under the blood collection tubing operation*. The peak current obtained from SWV of 3 devices exposed to 6 mL of 100 nM reporter ssDNA, are plotted by device (left) and by electrode position (right), demonstrating high repeatability. SWV measurements were conducted in 25 mM NaCl and 25 mM Phosphate buffer. All incubations and measurements steps were conducted at room temperature.*

6 Conclusions, key findings, and future work

6.1 Thesis summary and key findings

This thesis demonstrates the development of a flow-capable electrochemical biosensing platform that utilizes simple and scalable fabrication techniques. Through a roll-seal-shrink methodology, tubular devices with integrated electrodes were achieved. Due to the thin-film buckling experienced during shrinking, the electrodes exhibited a hierarchically wrinkled morphology allowing for increased interaction with flowing analyte. Coupling the sensing electrodes with modified wires allowed the creation of a 3-electrode electrochemical cell, enabling stable and sensitive measurement of reactions at the electrode surface. We conducted characterization of the device's innate properties and verified effect of flow on capture performance using DNA as the analyte. In the course of this project, considerable obstacles had to be overcome to create a novel platform capable of rapid analysis and continuous monitoring.

In Chapter 1, an overview and context for the development of biosensors for POC diagnostics is provided, with emphasis on the benefits of incorporating microfluidics. It highlights the growing need for rapid, accurate, and cost-effective POC diagnostic devices for improving patient outcomes. The section also discusses some of the challenges associated with biosensor development and outlines the motivation and approach used for this research.

In Chapter 2, a background is provided on the fundamental principles and techniques related to electrochemistry, biosensing, and microfluidics, and the current state of the art is explored. The various components of electrochemical systems are introduced, along with the fundamentals of reduction and oxidation reactions and relevant electrochemical analysis techniques. Biosensing is discussed with an emphasis on biorecognition techniques, DNA biosensors, redox reporters, and sensor surface preparation. The section also highlights the role of microfluidics for biosensing applications and the importance of flow phenomena such as turbulence, Poiseuille flow, and mass-transport/reaction limited regimes. This background information serves as a foundation for the development of biosensors for flow-based point-of-care diagnostics.

In Chapter 3, a detailed description of device fabrication and experimental methods employed is provided. Fabrication processes for both the device and wires is given, including necessary

materials. The protocols used for device characterization are presented, along with electrode functionalization, data collection, and analysis.

In Chapter 4, initial design considerations and decisions were discussed, and rationale was provided for strategies utilized. Certain parameters were optimized during development and key findings are as follows:

- Fabrication of flow-compatible devices was enabled through the use of heat-shrinkable polyolefin film. An 80% reduction on device size is achieved upon heating, causing the electrode patterns deposited on the film to undergo buckling. Shrinking enables the miniaturization of features, allowing for the design of features at a larger scale using benchtop techniques, thus simplifying the fabrication process. Electrodes situated inside the tube are accessible to the exterior surface for interfacing with detection equipment via contact pads that cross the heat-sealed region. Given the hydrophobicity of the wrinkled surface, longitudinal strip electrodes were found to allow for easier functionalization compared to circumferential designs. Interfacing to other fluidic equipment necessitated adding tubbing connections and sealing using viscous adhesives formulated for low-surface energy applications, enabling leak-free operation.
- Addition of wires into the flow region allowed for selective functionalization of the working electrode without affecting the reference/counter. In a 2-electrode system configuration, device response was highly dependant on both the positioning and properties of added reference/counter electrode. It was shown that the wire electrode should be placed in close proximity to the working electrode as distance between electrodes was inversely proportional to the resultant signal. Furthermore, the choice of wire surface structure and positioning in the 2-electrode system greatly influenced measured current. The wires featuring surface modifications that increased the exposed surface all performed similarly, suggesting a dependence on electroactive area. By inserting a wire through the side-wall of the device, perpendicular to the direction of flow, more optimal positioning of a 3-electrode system with dedicated counter and reference electrodes could be achieved without shorting.

- Preliminary flow results suggested improved biosensor performance under flowing analyte. Given the system dimensions, flow is expected to remain laminar and until approximately 96600 μL/min. Additionally, numerical modelling of mass-transport and binding kinetics suggest that the system benefits from increasing flow rate until the system becomes turbulent and the assumptions are no longer valid. Initial testing showed improved ssDNA capture under flow compared to static conditions. Basic optimization of the deposited capture probe concentration was done for the flowing system prior to further testing.

In Chapter 5, characterization of the lab-in-a-tube biosensor is performed, focusing on the physical characteristics, electrochemical response, and biochemical capture performance under flow conditions. Key findings are summarized as follows:

- Shrinking of the polymer substrate results in the creation of wrinkled gold electrodes with morphological features spanning several orders of magnitude, as shown by SEM. The heat-induced wrinkling allows for a 20-fold increase in surface area electrodes for a given geometric footprint, enabling the creation of high surface area electrodes in the small form factors necessary for POC diagnostics. A potential hinderance of the wrinkled electrodes is the increase of hydrophobicity compared to planar electrodes. Measurement of the water contact angle was 143° after wrinkling, however was reduced to 81° upon functionalization with ssDNA and 29° upon passivation of the electrode surface with MCH.
- Electrochemical characterization of the bare electrode indicates that the surface reaction behavior of the system remains predominantly diffusion-controlled until at least 100 μL/min when interrogated with a flowing ferrocyanide/ferricyanide redox couple. Further characterization of hydrodynamic properties is required however to understand the role of mass-transport to the wrinkled electrode surface. Device performance under pulsed addition of dopamine is promising for continuous monitoring applications when combined with antifouling techniques.

- The lab-in-a-tube device displayed fast capture kinetics of 100 nM ssDNA under 2000 µL/min recirculating flow conditions. Both the heat-seal that defines the tubular shape and the inlet/outlet adhesive showed no signs of leaking throughout the 70-minute of flow. It was determined that for a fixed time duration, increasing the flow rate resulted in higher detection signal. The relationship was shown to be strongly dependant on the volume of sample passing through the device. Furthermore, it was shown that the wrinkled electrode surface did not result in appreciable non-specific adsorption of mismatched ssDNA. Interestingly, results from a fixed sample volume were shown to yield similar signal magnitudes despite orders of magnitude faster analysis times by proportionally increasing the flow rate. This rapid sample processing was demonstrated with low-cost blood collection tubes to induce flow, showing great promise for incorporation into existing medical tubing.

6.2 Future work

In order to create a truly simple POC biosensor platform, further development should focus on addressing a number of challenges that impede usability and performance.

One of the first areas interest is improving the manufacturability of the device to facilitate further research. Currently, development is limited by the fabrication yield despite the rapid (<1 day) fabrication time. The current limiting factor is the working area of the available the sputter deposition equipment as it is ill-suited for lab-in-a-tube fabrication due to the (relatively) large initial size of devices before shrinking. Use of equipment with larger deposition areas would greatly increase device production. Specialized sputtering equipment with features such as airlocks for sample interchanging or roll-to-roll sample processing could also address this problem. Alternatively, exploring alternative electrode fabrication methods such as screen-printing or solution-processing techniques is desirable. The use of wires as counter and reference electrodes could be eliminated, further simplifying the fabrication process.

Further research should be done on understanding the effect of the wrinkled surface on biosensing. Currently, little is known about the flow profile as it interacts with the 3-dimensional electrode surface. Furthermore, it is not clear how analytes in solution interact with the wrinkled

geometry. Diffusion from the outer extremities of the electrode into the depths of the folds may have considerable influence on mass-transport properties. Similarly, it remains unknown to what degree the electrode functionalization is uniform. Deposition of biorecognition elements may be distributed in a gradient within the depth of the wrinkles, leading to different capture kinetics that vary with the morphological features.

An additional avenue worth investigating is the use of computational modeling and simulations to better understand sensor characteristics and to optimize performance. By conducting computational fluid dynamics simulations, insight into the behavior of mass transport into the wrinkled electrode could be obtained. Simulations could also be used to predict sensor performance under different flow conditions, aiding to optimize the design for improved sensitivity and specificity.

Both the electrode and contact pad shape could be optimized to better suit their purpose. Biosensor performance could be enhanced by tailoring the electrode geometry to the specific assay type and flow rates expected of the system. For example, an assay featuring electrodes that release a marker upon interaction with a specific analyte could have capture electrodes placed in an optimal location for downstream collection. The contact pads could be designed alongside an external unit to interface with a portable potentiostat to enable real-time analysis and remote monitoring at the patient's bedside.

Future work could explore the integration of sample processing elements to improve functionality and handling of complex samples. For example, the biosensor could be combined with microfluidic components that perform cell lysis, purify the sample, or add reagents to improve detection capability.

Finally, validation of the platform's performance using clinical samples is imperative. Although the sensor has shown great promise using spiked samples, real-world samples may contain interfering substances that could impede biosensor function. By using clinical samples, researchers can evaluate the interaction between device and sample and further developments could be made to minimize unwanted effects.

7 Bibliography

[1] E. Fu, P. Yager, P. N. Floriano, N. Christodoulides, and J. T. McDevitt, "Perspective on Diagnostics for Global Health," *IEEE Pulse*, vol. 2, no. 6, pp. 40–50, Nov. 2011.

[2] M. L. Sin, K. E. Mach, P. K. Wong, and J. C. Liao, "Advances and challenges in biosensor-based diagnosis of infectious diseases," *Expert Rev. Mol. Diagn.*, vol. 14, no. 2, pp. 225–244, 2014.

[3] N. Bhalla, P. Jolly, N. Formisano, and P. Estrela, "Introduction to biosensors," *Essays Biochem.*, vol. 60, no. 1, pp. 1–8, Jun. 2016.

[4] C. D. Chin, V. Linder, and S. K. Sia, "Commercialization of microfluidic point-of-care diagnostic devices," *Lab on a Chip*, vol. 12, no. 12. pp. 2118–2134, 2012.

[5] S. Vigneshvar, C. C. Sudhakumari, B. Senthilkumaran, and H. Prakash, "Recent advances in biosensor technology for potential applications - an overview," *Front. Bioeng. Biotechnol.*, vol. 4, no. FEB, pp. 1–9, 2016.

[6] P. Yager, G. J. Domingo, and J. Gerdes, "Point-of-care diagnostics for global health," *Annu. Rev. Biomed. Eng.*, vol. 10, pp. 107–144, 2008.

[7] S. A. Soper *et al.*, "Point-of-care biosensor systems for cancer diagnostics/prognostics," *Biosens. Bioelectron.*, vol. 21, no. 10, pp. 1932–1942, 2006.

[8] M. Zarei, "Portable biosensing devices for point-of-care diagnostics: Recent developments and applications," *TrAC - Trends Anal. Chem.*, vol. 91, pp. 26–41, 2017.

[9] B. S. Ferguson *et al.*, "Real-time, aptamer-based tracking of circulating therapeutic agents in living animals," *Sci. Transl. Med.*, vol. 5, no. 213, 2013.

[10] J. R. Mejía-Salazar, K. R. Cruz, E. M. M. Vásques, and O. N. de Oliveira, "Microfluidic point-of-care devices: New trends and future prospects for ehealth diagnostics," *Sensors (Switzerland)*, vol. 20, no. 7, pp. 1–19, 2020.

[11] S. Choi, M. Goryll, L. Y. M. Sin, P. K. Wong, and J. Chae, "Microfluidic-based biosensors

toward point-of-care detection of nucleic acids and proteins," *Microfluid. Nanofluidics*, vol. 10, no. 2, pp. 231–247, 2011.

[12] M. I. H. Ansari, S. Hassan, A. Qurashi, and F. A. Khanday, "Microfluidic-integrated DNA nanobiosensors," *Biosens. Bioelectron.*, vol. 85, pp. 247–260, 2016.

[13] J. Castillo-leon, *Lab-on-a-Chip Devices and Micro-Total Analysis Systems*, no. November. Cham: Springer International Publishing, 2015.

[14] M. Selmi, M. H. Gazzah, and H. Belmabrouk, "Optimization of microfluidic biosensor efficiency by means of fluid flow engineering," *Sci. Rep.*, vol. 7, no. 1, p. 5721, Dec. 2017.

[15] A. P. F. Turner, "Biosensors: Sense and sensibility," *Chem. Soc. Rev.*, vol. 42, no. 8, pp. 3184–3196, 2013.

[16] H. Kettler, K. White, and S. Hawkes, "Mapping the landscape of diagnostics for sexually transmitted infections: Key findings and recommandations," *Unicef/Undp/World Bank/Who*, pp. 1–44, 2004.

[17] N. P. Pai, C. Vadnais, C. Denkinger, N. Engel, and M. Pai, "Point-of-Care Testing for Infectious Diseases: Diversity, Complexity, and Barriers in Low- And Middle-Income Countries," *PLoS Med.*, vol. 9, no. 9, 2012.

[18] A. C. Carpenter, I. T. Paulsen, and T. C. Williams, "Blueprints for biosensors: Design, limitations, and applications," *Genes (Basel).*, vol. 9, no. 8, 2018.

[19] P. Panjan, V. Virtanen, and A. M. Sesay, "Determination of stability characteristics for electrochemical biosensors via thermally accelerated ageing," *Talanta*, vol. 170, no. December 2016, pp. 331–336, 2017.

[20] J. H. T. Luong, K. B. Male, and J. D. Glennon, "Biosensor technology: Technology push versus market pull," *Biotechnol. Adv.*, vol. 26, no. 5, pp. 492–500, Sep. 2008.

[21] H. H. Lee and J. P. Allain, "Improving blood safety in resource-poor settings," *Vox Sang.*, vol. 87, no. s2, pp. 176–179, Jul. 2004.

[22] M. Ritzi-Lehnert, "Development of chip-compatible sample preparation for diagnosis of infectious diseases," *Expert Rev. Mol. Diagn.*, vol. 12, no. 2, pp. 189–206, Mar. 2012.

[23] N. Wisniewski and M. Reichert, "Methods for reducing biosensor membrane biofouling," *Colloids Surfaces B Biointerfaces*, vol. 18, no. 3–4, pp. 197–219, 2000.

[24] H. Vaisocherová, E. Brynda, and J. Homola, "Functionalizable low-fouling coatings for label-free biosensing in complex biological media: advances and applications," *Anal. Bioanal. Chem.*, vol. 407, no. 14, pp. 3927–3953, 2015.

[25] N. Bunyakul and A. Baeumner, "Combining Electrochemical Sensors with Miniaturized Sample Preparation for Rapid Detection in Clinical Samples," *Sensors*, vol. 15, no. 1, pp. 547–564, Dec. 2014.

[26] J. Park, D. H. Han, and J.-K. Park, "Towards practical sample preparation in point-of-care testing: user-friendly microfluidic devices," *Lab Chip*, vol. 20, no. 7, pp. 1191–1203, 2020.

[27] C. G. Zoski, *Handbook of Electrochemistry*. Elsevier, 2007.

[28] D. Grieshaber, R. MacKenzie, J. Vörös, and E. Reimhult, "Electrochemical biosensors - Sensor principles and architectures," *Sensors*, vol. 8, no. 3. pp. 1400–1458, 2008.

[29] A. J. Bard, *ELECTROCHEMICAL METHODS Fundamentals and Applications*. Elsevier, 2001.

[30] N. Elgrishi, K. J. Rountree, B. D. McCarthy, E. S. Rountree, T. T. Eisenhart, and J. L. Dempsey, "A Practical Beginner's Guide to Cyclic Voltammetry," *J. Chem. Educ.*, vol. 95, no. 2, pp. 197–206, 2018.

[31] N. J. Ronkainen, H. B. Halsall, and W. R. Heineman, "Electrochemical biosensors," *Chem. Soc. Rev.*, vol. 39, no. 5, pp. 1747–1763, 2010.

[32] F. Xia, X. Zhang, X. Lou, and Q. Yuan, *Biosensors based on sandwich assays*. 2018.

[33] J. L. Hammond, N. Formisano, P. Estrela, S. Carrara, and J. Tkac, "Electrochemical biosensors and nanobiosensors," *Essays Biochem.*, vol. 60, no. 1, pp. 69–80, 2016.

[34] J. S. Daniels and N. Pourmand, "Label-free impedance biosensors: Opportunities and

challenges," *Electroanalysis*, vol. 19, no. 12. NIH Public Access, pp. 1239–1257, Jun-2007.

[35] A. M. Bond *et al.*, *Electroanalytical Methods, Guide to Experiments and Applications 2nd, revised and extended edition*. 2009.

[36] R. Lao *et al.*, "Electrochemical interrogation of DNA monolayers on gold surfaces," *Anal. Chem.*, vol. 77, no. 19, pp. 6475–6480, 2005.

[37] X. Liu, P. A. Duckworth, and D. K. Y. Wong, "Square wave voltammetry versus electrochemical impedance spectroscopy as a rapid detection technique at electrochemical immunosensors," *Biosens. Bioelectron.*, vol. 25, no. 6, pp. 1467–1473, 2010.

[38] S. J. Cobb and J. V. Macpherson, "Enhancing Square Wave Voltammetry Measurements via Electrochemical Analysis of the Non-Faradaic Potential Window," *Anal. Chem.*, vol. 91, no. 12, pp. 7935–7942, 2019.

[39] J. P. Chambers, B. P. Arulanandam, L. L. Matta, A. Weis, and J. J. Valdes, "Biosensor Recognition Elements," *Curr. Issues Mol. Biol.*, pp. 1–12, 2008.

[40] M. A. Morales and J. M. Halpern, "Guide to Selecting a Biorecognition Element for Biosensors," *Bioconjug. Chem.*, vol. 29, no. 10, pp. 3231–3239, Oct. 2018.

[41] S. Liu, L. Fang, Y. Wang, and L. Wang, "Universal Dynamic DNA Assembly-Programmed Surface Hybridization Effect for Single-Step, Reusable, and Amplified Electrochemical Nucleic Acid Biosensing," *Anal. Chem.*, vol. 89, no. 5, pp. 3108–3115, 2017.

[42] V. Ruiz-Valdepenas Montiel *et al.*, "Comparison of Different Strategies for the Development of Highly Sensitive Electrochemical Nucleic Acid Biosensors Using Neither Nanomaterials nor Nucleic Acid Amplification," *ACS Sensors*, vol. 3, no. 1, pp. 211–221, 2018.

[43] J. Wang, "Electrochemical nucleic acid biosensors," *Anal. Chim. Acta*, vol. 469, no. 1, pp. 63–71, 2002.

[44] J. Labuda *et al.*, "Electrochemical nucleic acid-based biosensors: Concepts, terms, and

methodology (IUPAC Technical Report)," *Pure Appl. Chem.*, vol. 82, no. 5, pp. 1161–1187, 2010.

[45] I. Willner and M. Zayats, "Electronic aptamer-based sensors," *Angew. Chemie - Int. Ed.*, vol. 46, no. 34, pp. 6408–6418, 2007.

[46] M. H. Ali, M. E. Elsherbiny, and M. Emara, "Updates on aptamer research," *International Journal of Molecular Sciences*, vol. 20, no. 10. pp. 1–23, 2019.

[47] N. de-los-Santos-Álvarez, M. J. Lobo-Castañón, A. J. Miranda-Ordieres, and P. Tuñón-Blanco, "Aptamers as recognition elements for label-free analytical devices," *TrAC - Trends Anal. Chem.*, vol. 27, no. 5, pp. 437–446, 2008.

[48] A. V. Lakhin, V. Z. Tarantul, and L. V. Gening, "Aptamers: Problems, solutions and prospects," *Acta Naturae*, vol. 5, no. 19. Russian Federation Agency for Science and Innovation, pp. 34–43, 2013.

[49] T. Monteiro and M. G. Almeida, "Electrochemical Enzyme Biosensors Revisited: Old Solutions for New Problems," *Crit. Rev. Anal. Chem.*, vol. 49, no. 1, pp. 44–66, 2019.

[50] S. Kurbanoglu, C. Erkmen, and B. Uslu, "Frontiers in electrochemical enzyme based biosensors for food and drug analysis," *TrAC - Trends Anal. Chem.*, vol. 124, p. 115809, 2020.

[51] S. Jeong, J. Park, D. Pathania, C. M. Castro, R. Weissleder, and H. Lee, "Integrated Magneto-Electrochemical Sensor for Exosome Analysis," *ACS Nano*, vol. 10, no. 2, pp. 1802–1809, 2016.

[52] J. Park *et al.*, "Integrated Kidney Exosome Analysis for the Detection of Kidney Transplant Rejection," *ACS Nano*, vol. 11, no. 11, pp. 11041–11046, 2017.

[53] J. Park *et al.*, "An integrated magneto-electrochemical device for the rapid profiling of tumour extracellular vesicles from blood plasma," *Nat. Biomed. Eng.*, vol. 5, no. 7, pp. 678–689, 2021.

[54] G. Li, W. Tang, and F. Yang, "Cancer Liquid Biopsy Using Integrated Microfluidic Exosome

Analysis Platforms," *Biotechnol. J.*, vol. 15, no. 5, p. 1900225, May 2020.

[55] V. C. Diculescu, A. M. Chiorcea-Paquim, and A. M. Oliveira-Brett, "Applications of a DNA-electrochemical biosensor," *TrAC - Trends Anal. Chem.*, vol. 79, pp. 23–36, 2016.

[56] V. V. Demidov, *DNA beyond genes: From data storage and computing to nanobots, nanomedicine, and nanoelectronics*. 2020.

[57] M. A. Pellitero, A. Shaver, and N. Arroyo-Currás, "Critical Review—Approaches for the Electrochemical Interrogation of DNA-Based Sensors: A Critical Review," *J. Electrochem. Soc.*, vol. 167, no. 3, p. 037529, 2020.

[58] M. Trotter, N. Borst, R. Thewes, and F. von Stetten, "Review: Electrochemical DNA sensing – Principles, commercial systems, and applications," *Biosens. Bioelectron.*, vol. 154, no. February, 2020.

[59] A. M. Oliveira-Brett, J. A. P. Piedade, L. A. Silva, and V. C. Diculescu, "Voltammetric determination of all DNA nucleotides," *Anal. Biochem.*, vol. 332, no. 2, pp. 321–329, 2004.

[60] V. Tsouti, C. Boutopoulos, I. Zergioti, and S. Chatzandroulis, "Capacitive microsystems for biological sensing," *Biosens. Bioelectron.*, vol. 27, no. 1, pp. 1–11, 2011.

[61] S. D. Keighley, P. Li, P. Estrela, and P. Migliorato, "Optimization of DNA immobilization on gold electrodes for label-free detection by electrochemical impedance spectroscopy," *Biosens. Bioelectron.*, vol. 23, no. 8, pp. 1291–1297, 2008.

[62] J. Kafka, O. Pänke, B. Abendroth, and F. Lisdat, "A label-free DNA sensor based on impedance spectroscopy," *Electrochim. Acta*, vol. 53, no. 25, pp. 7467–7474, 2008.

[63] A. Bogomolova *et al.*, "Challenges of Electrochemical Impedance Spectroscopy in Protein Biosensing," *Anal. Chem.*, vol. 81, no. 10, pp. 3944–3949, May 2009.

[64] P. Dauphin-Ducharme and K. W. Plaxco, "Maximizing the Signal Gain of Electrochemical-DNA Sensors," *Anal. Chem.*, vol. 88, no. 23, pp. 11654–11662, Dec. 2016.

[65] L. Fabbrizzi, "The ferrocenium/ferrocene couple: a versatile redox switch," *ChemTexts*, vol.

6, no. 4, pp. 1–20, 2020.

[66] C. G. Pheeney and J. K. Barton, "DNA electrochemistry with tethered methylene blue," *Langmuir*, vol. 28, no. 17, pp. 7063–7070, 2012.

[67] K. Han, Z. Liang, and N. Zhou, "Design strategies for aptamer-based biosensors," *Sensors*, vol. 10, no. 5, pp. 4541–4557, 2010.

[68] A. Sassolas, B. D. Leca-Bouvier, and L. J. Blum, "DNA biosensors and microarrays," *Chem. Rev.*, vol. 108, no. 1, pp. 109–139, 2008.

[69] J. I. A. Rashid and N. A. Yusof, "The strategies of DNA immobilization and hybridization detection mechanism in the construction of electrochemical DNA sensor: A review," *Sens. Bio-Sensing Res.*, vol. 16, no. April, pp. 19–31, 2017.

[70] H. T. Rong *et al.*, "On the importance of the headgroup substrate bond in thiol monolayers: A study of biphenyl-based thiols on gold and silver," *Langmuir*, vol. 17, no. 5, pp. 1582–1593, 2001.

[71] M. Yüce and H. Kurt, "How to make nanobiosensors: Surface modification and characterisation of nanomaterials for biosensing applications," *RSC Adv.*, vol. 7, no. 78, pp. 49386–49403, 2017.

[72] N. Patel *et al.*, "Immobilization of protein molecules onto homogeneous and mixed carboxylate-terminated self-assembled monolayers," *Langmuir*, vol. 13, no. 24, pp. 6485–6490, 1997.

[73] A. Makaraviciute, X. Xu, L. Nyholm, and Z. Zhang, "Systematic Approach to the Development of Microfabricated Biosensors: Relationship between Gold Surface Pretreatment and Thiolated Molecule Binding," *ACS Appl. Mater. Interfaces*, vol. 9, no. 31, pp. 26610–26621, 2017.

[74] R. M. West, "Review—Electrical Manipulation of DNA Self-Assembled Monolayers: Electrochemical Melting of Surface-Bound DNA," *J. Electrochem. Soc.*, vol. 167, no. 3, p. 037544, 2020.

[75] F. Ricci, R. Y. Lai, A. J. Heeger, K. W. Plaxco, and J. J. Sumner, "Effect of molecular crowding on the response of an electrochemical DNA sensor," *Langmuir*, vol. 23, no. 12, pp. 6827–6834, 2007.

[76] X. Xu *et al.*, "Structural Changes of Mercaptohexanol Self-Assembled Monolayers on Gold and Their Influence on Impedimetric Aptamer Sensors," *Anal. Chem.*, 2019.

[77] J. A. Lee, S. Hwang, J. Kwak, S. Il Park, S. S. Lee, and K. C. Lee, "An electrochemical impedance biosensor with aptamer-modified pyrolyzed carbon electrode for label-free protein detection," *Sensors Actuators, B Chem.*, vol. 129, no. 1, pp. 372–379, 2008.

[78] J. T. Kirk, N. D. Brault, T. Baehr-Jones, M. Hochberg, S. Jiang, and D. M. Ratner, "Zwitterionic polymer-modified silicon microring resonators for label-free biosensing in undiluted human plasma," *Biosens. Bioelectron.*, vol. 42, no. 1, pp. 100–105, 2013.

[79] D. J. Beebe, G. A. Mensing, and G. M. Walker, "Physics and applications of microfluidics in biology," *Annu. Rev. Biomed. Eng.*, vol. 4, pp. 261–286, 2002.

[80] J. Berthier and P. Silberzan, *Microfluidics for Biotechnology, Second Edition*. Artech House, 2010.

[81] T. M. Squires, R. J. Messinger, and S. R. Manalis, "Making it stick: Convection, reaction and diffusion in surface-based biosensors," *Nat. Biotechnol.*, vol. 26, no. 4, pp. 417–426, 2008.

[82] I. Pereiro, A. Fomitcheva-Khartchenko, and G. V. Kaigala, "Shake It or Shrink It: Mass Transport and Kinetics in Surface Bioassays Using Agitation and Microfluidics," *Anal. Chem.*, vol. 92, no. 15, pp. 10187–10195, 2020.

[83] D. Mark, S. Haeberle, G. Roth, F. von Stetten, and R. Zengerle, "Microfluidic lab-on-a-chip platforms: requirements, characteristics and applications," *Chem. Soc. Rev.*, vol. 39, no. 3, p. 1153, 2010.

[84] Y. Uludag *et al.*, "An integrated lab-on-a-chip-based electrochemical biosensor for rapid and sensitive detection of cancer biomarkers," *Anal. Bioanal. Chem.*, vol. 408, no. 27, pp. 7775–7783, 2016.

[85] I. Moser and G. Jobst, "Pre-Calibrated Biosensors for Single-Use Applications," *Chemie Ing. Tech.*, vol. 85, no. 1–2, pp. 172–178, Feb. 2013.

[86] K. Pontius, D. Semenova, Y. E. Silina, K. V. Gernaey, and H. Junicke, "Automated Electrochemical Glucose Biosensor Platform as an Efficient Tool Toward On-Line Fermentation Monitoring: Novel Application Approaches and Insights," *Front. Bioeng. Biotechnol.*, vol. 8, no. May, pp. 1–15, 2020.

[87] S. N. Tan, L. Ge, H. Y. Tan, W. K. Loke, J. Gao, and W. Wang, "Paper-based enzyme immobilization for flow injection electrochemical biosensor integrated with reagent-loaded cartridge toward portable modular device," *Anal. Chem.*, vol. 84, no. 22, pp. 10071–10076, 2012.

[88] C. S. Martinez-Cisneros, S. Sanchez, W. Xi, and O. G. Schmidt, "Ultracompact three-dimensional tubular conductivity microsensors for ionic and biosensing applications," *Nano Lett.*, vol. 14, no. 4, pp. 2219–2224, 2014.

[89] Y. Liu *et al.*, "Reciprocating-flowing on-a-chip enables ultra-fast immunobinding for multiplexed rapid ELISA detection of SARS-CoV-2 antibody," *Biosens. Bioelectron.*, vol. 176, no. January, p. 112920, Mar. 2021.

[90] C. Li, P. M. Wu, J. Han, and C. H. Ahn, "A flexible polymer tube lab-chip integrated with microsensors for smart microcatheter," *Biomed. Microdevices*, vol. 10, no. 5, pp. 671–679, 2008.

[91] C. Li, L. A. Shutter, P. M. Wu, C. H. Ahn, and R. K. Narayan, "Potential of a simple lab-on-a-tube for point-of-care measurements of multiple analytes," *Lab Chip*, vol. 10, no. 11, pp. 1476–1479, 2010.

[92] J. Park *et al.*, "Microscale Biosensor Array Based on Flexible Polymeric Platform toward Lab-on-a-Needle: Real-Time Multiparameter Biomedical Assays on Curved Needle Surfaces," *ACS Sensors*, vol. 5, no. 5, pp. 1363–1373, 2020.

[93] A. Kagie *et al.*, "Flexible Rolled Thick-Film Miniaturized Flow-Cell for Minimally Invasive

Amperometric Sensing," *Electroanalysis*, vol. 20, no. 14, pp. 1610–1614, Jul. 2008.

[94] N. Arroyo-Currás, K. Scida, K. L. Ploense, T. E. Kippin, and K. W. Plaxco, "High Surface Area Electrodes Generated via Electrochemical Roughening Improve the Signaling of Electrochemical Aptamer-Based Biosensors," *Anal. Chem.*, vol. 89, no. 22, pp. 12185–12191, 2017.

[95] P. Dauphin-Ducharme *et al.*, "Electrochemical Aptamer-Based Sensors for Improved Therapeutic Drug Monitoring and High-Precision, Feedback-Controlled Drug Delivery," *ACS Sensors*, vol. 4, no. 10, pp. 2832–2837, 2019.

[96] A. Chamorro-Garcia *et al.*, "Real-Time, Seconds-Resolved Measurements of Plasma Methotrexate In Situ in the Living Body," *ACS Sensors*, vol. 8, no. 1, pp. 150–157, Jan. 2023.

[97] K. K. Leung *et al.*, "A tight squeeze: geometric effects on the performance of three-electrode electrochemical-aptamer based sensors in constrained, in-vivo placements," *Analyst*, 2023.

[98] D. S. Jin, E. L. Brightbill, and E. M. Vogel, "General model for mass transport to planar and nanowire biosensor surfaces," *J. Appl. Phys.*, vol. 125, no. 11, 2019.

[99] A. Shrivastava and V. Gupta, "Methods for the determination of limit of detection and limit of quantitation of the analytical methods," *Chronicles Young Sci.*, vol. 2, no. 1, p. 21, 2011.

[100] S. Chattopadhyay, T. K. Chaki, and A. K. Bhowmick, "Heat shrinkability of electron-beam-modified thermoplastic elastomeric films from blends of ethylene-vinylacetate copolymer and polyethylene," *Radiat. Phys. Chem.*, vol. 59, no. 5–6, pp. 501–510, 2000.

[101] M. Trojanowicz, M. Szewczynska, and M. Wcislo, "Electroanalytical Flow Measurements-Recent Advances," *Electroanalysis*, vol. 15, no. 5–6, pp. 347–365, Apr. 2003.

[102] A. C. Fisher and R. G. Compton, "Double-channel electrodes: Homogeneous kinetics and collection efficiency measurements," *J. Appl. Electrochem.*, vol. 21, no. 3, pp. 208–212, 1991.

[103] M. A. Alma, *Polyolefin Compounds and Materials*. Cham: Springer International Publishing,

2016.

[104] E. M. Petrie, *Handbook of Adhesives and Sealants*, 2nd ed. New York: McGraw-Hill, 2000.

[105] A. Ferrario, M. Scaramuzza, E. Pasqualotto, A. De Toni, and A. Paccagnella, "Development of a disposable gold electrodes-based sensor for electrochemical measurements of cDNA hybridization," *Procedia Chem.*, vol. 6, pp. 36–45, 2012.

[106] N. S. Mazlan *et al.*, "Interdigitated electrodes as impedance and capacitance biosensors: A review," *AIP Conf. Proc.*, vol. 1885, 2017.

[107] J. Liu, L. Peng, Y. Zhou, J. Qiao, and J. Jung, " Influence of Electrode Distance on the Electrochemical Reduction of CO 2 in Aqueous Solution ," *ECS Meet. Abstr.*, vol. MA2019-02, no. 40, pp. 1828–1828, 2019.

[108] M. Sophocleous and J. K. Atkinson, "A review of screen-printed silver/silver chloride (Ag/AgCl) reference electrodes potentially suitable for environmental potentiometric sensors," *Sensors Actuators, A Phys.*, vol. 267, pp. 106–120, 2017.

[109] M. Waleed Shinwari, D. Zhitomirsky, I. A. Deen, P. R. Selvaganapathy, M. Jamal Deen, and D. Landheer, "Microfabricated reference electrodes and their biosensing applications," *Sensors*, vol. 10, no. 3, pp. 1679–1715, 2010.

[110] Y. Okahata, M. Kawase, K. Niikura, F. Ohtake, H. Furusawa, and Y. Ebara, "Kinetic Measurements of DNA Hybridization on an Oligonucleotide-Immobilized 27-MHz Quartz Crystal Microbalance," *Anal. Chem.*, vol. 70, no. 7, pp. 1288–1291, 1998.

[111] P. H. Bigg, "Density of water in SI units over the range 0-40°C," *Br. J. Appl. Phys.*, vol. 18, no. 4, pp. 521–525, 1967.

[112] L. Korson, W. Drost-Hansen, and F. J. Millero, "Viscosity of water at various temperatures," *J. Phys. Chem.*, vol. 73, no. 1, pp. 34–39, 1969.

[113] V. Chan, D. J. Graves, and S. E. McKenzie, "The biophysics of DNA hybridization with immobilized oligonucleotide probes," *Biophys. J.*, vol. 69, no. 6, pp. 2243–2255, Dec. 1995.

[114] R. Pandey, D. Chang, M. Smieja, T. Hoare, Y. Li, and L. Soleymani, "Integrating programmable DNAzymes with electrical readout for rapid and culture-free bacterial detection using a handheld platform," *Nat. Chem.*, pp. 1–7, Jun. 2021.

[115] J. X. Zhang *et al.*, "Predicting DNA hybridization kinetics from sequence," *Nat. Chem.*, vol. 10, no. 1, pp. 91–98, 2018.

[116] D. Erickson, D. Li, and U. J. Krull, "Modeling of DNA hybridization kinetics for spatially resolved biochips," *Anal. Biochem.*, vol. 317, no. 2, pp. 186–200, 2003.

[117] S. E. Halford, "An end to 40 years of mistakes in DNA-protein association kinetics?," *Biochem. Soc. Trans.*, vol. 37, no. 2, pp. 343–348, 2009.

[118] G. Carpini, F. Lucarelli, G. Marrazza, and M. Mascini, "Oligonucleotide-modified screen-printed gold electrodes for enzyme-amplified sensing of nucleic acids," *Biosens. Bioelectron.*, vol. 20, no. 2, pp. 167–175, 2004.

[119] F. Lucarelli, G. Marrazza, and M. Mascini, "Enzyme-based impedimetric detection of PCR products using oligonucleotide-modified screen-printed gold electrodes," in *Biosensors and Bioelectronics*, 2005, vol. 20, no. 10 SPEC. ISS., pp. 2001–2009.

[120] C. M. Gabardo, Y. Zhu, L. Soleymani, and J. M. Moran-Mirabal, "Bench-top fabrication of hierarchically structured high-surface-area electrodes," *Adv. Funct. Mater.*, vol. 23, no. 24, pp. 3030–3039, 2013.

[121] S. M. Woo, C. M. Gabardo, and L. Soleymani, "Prototyping of wrinkled nano-/microstructured electrodes for electrochemical DNA detection," *Anal. Chem.*, vol. 86, no. 24, pp. 12341–12347, 2014.

[122] Y. Tian, H. Liu, G. Zhao, and T. Tatsuma, "Shape-controlled electrodeposition of gold nanostructures," *J. Phys. Chem. B*, vol. 110, no. 46, pp. 23478–23481, 2006.

[123] N. Rohaizad, C. C. Mayorga-Martinez, F. Novotný, R. D. Webster, and M. Pumera, "3D-printed Ag/AgCl pseudo-reference electrodes," *Electrochem. commun.*, vol. 103, no. May, pp. 104–108, 2019.

[124] J. Y. Chung, A. J. Nolte, and C. M. Stafford, "Surface Wrinkling: A Versatile Platform for Measuring Thin-Film Properties," *Adv. Mater.*, vol. 23, no. 3, pp. 349–368, Jan. 2011.

[125] J. Groenewold, "Wrinkling of plates coupled with soft elastic media," *Physica A*, vol. 298, pp. 32–45, 2001.

[126] Z. Huang, W. Hong, and Z. Suo, "Evolution of wrinkles in hard films on soft substrates," *Phys. Rev. E - Stat. Physics, Plasmas, Fluids, Relat. Interdiscip. Top.*, vol. 70, no. 3, p. 4, 2004.

[127] S. K. Saha, "Sensitivity of the mode locking phenomenon to geometric imperfections during wrinkling of supported thin films," *Int. J. Solids Struct.*, vol. 109, pp. 166–179, 2017.

[128] C. C. Fu *et al.*, "Tunable nanowrinkles on shape memory polymer sheets," *Adv. Mater.*, vol. 21, no. 44, pp. 4472–4476, 2009.

[129] Z. Matharu, P. Daggumati, L. Wang, T. S. Dorofeeva, Z. Li, and E. Seker, "Nanoporous-Gold-Based Electrode Morphology Libraries for Investigating Structure-Property Relationships in Nucleic Acid Based Electrochemical Biosensors," *ACS Appl. Mater. Interfaces*, vol. 9, no. 15, pp. 12959–12966, 2017.

[130] T. Bayraktar and S. B. Pidugu, "Characterization of liquid flows in microfluidic systems," *Int. J. Heat Mass Transf.*, vol. 49, no. 5–6, pp. 815–824, 2006.

[131] S. Prentner, D. M. Allen, L. Larcombe, S. Marson, K. Jenkins, and M. Saumer, "Effects of channel surface finish on blood flow in microfluidic devices," *Microsyst. Technol.*, vol. 16, no. 7, pp. 1091–1096, 2010.

[132] V. Švorčík, Z. Kolská, T. Luxbacher, and J. Mistrík, "Properties of Au nanolayer sputtered on polyethyleneterephthalate," *Mater. Lett.*, vol. 64, no. 5, pp. 611–613, 2010.

[133] Y. Golan, L. Margulis, and I. Rubinstein, "Vacuum-deposited gold films," *Surf. Sci.*, vol. 264, no. 3, pp. 312–326, Mar. 1992.

[134] J. Siegel, O. Lyutakov, V. Rybka, Z. Kolská, and V. Švorčík, "Properties of gold nanostructures sputtered on glass," *Nanoscale Res. Lett.*, vol. 6, no. 1, pp. 1–9, 2011.

[135] X. Bin, E. H. Sargent, and S. O. Kelley, "Nanostructuring of Sensors Determines the Efficiency of Biomolecular Capture," *Anal. Chem.*, vol. 82, no. 14, pp. 5928–5931, Jul. 2010.

[136] K.-Y. Law, "Definitions for Hydrophilicity, Hydrophobicity, and Superhydrophobicity: Getting the Basics Right," *J. Phys. Chem. Lett.*, vol. 5, no. 4, pp. 686–688, Feb. 2014.

[137] A. Shahraz, A. Borhan, and K. A. Fichthorn, "A theory for the morphological dependence of wetting on a physically patterned solid surface," *Langmuir*, vol. 28, no. 40, pp. 14227–14237, 2012.

[138] H. Yildirim Erbil and C. Elif Cansoy, "Range of applicability of the wenzel and cassie-baxter equations for superhydrophobic surfaces," *Langmuir*, vol. 25, no. 24, pp. 14135–14145, 2009.

[139] D. Janssen, R. De Palma, S. Verlaak, P. Heremans, and W. Dehaen, "Static solvent contact angle measurements, surface free energy and wettability determination of various self-assembled monolayers on silicon dioxide," *Thin Solid Films*, vol. 515, no. 4, pp. 1433–1438, 2006.

[140] Y. Hao, D. M. Soolaman, and H. Z. Yu, "Controlled wetting on electrodeposited oxide thin films: From hydrophilic to superhydrophobic," *J. Phys. Chem. C*, vol. 117, no. 15, pp. 7736–7743, 2013.

[141] S. Li, Y. Wang, Z. Zhang, Y. Wang, H. Li, and F. Xia, "Exploring End-Group Effect of Alkanethiol Self-Assembled Monolayers on Electrochemical Aptamer-Based Sensors in Biological Fluids," *Anal. Chem.*, vol. 93, no. 14, pp. 5849–5855, 2021.

[142] B. J. Adesokan, X. Quan, A. Evgrafov, A. Heiskanen, A. Boisen, and M. P. Sørensen, "Experimentation and numerical modeling of cyclic voltammetry for electrochemical micro-sized sensors under the influence of electrolyte flow," *J. Electroanal. Chem.*, vol. 763, pp. 141–148, 2016.

[143] R. G. Compton and P. R. Unwin, "Channel and tubular electrodes," *J. Electroanal. Chem. Interfacial Electrochem.*, vol. 205, no. 1–2, pp. 1–20, 1986.

[144] J. A. Cooper and R. G. Compton, "Channel Electrodes - A Review," *Electroanalysis*, vol. 10, no. 3, pp. 141–155, 1998.

[145] R. A. Wise, "Dopamine, learning and motivation," *Nature Reviews Neuroscience*, vol. 5, no. 6. pp. 483–494, 2004.

[146] D. S. Kim *et al.*, "Electrochemical detection of dopamine using periodic cylindrical gold nanoelectrode arrays," *Sci. Rep.*, vol. 8, no. 1, p. 14049, 2018.

[147] S. M. Matt and P. J. Gaskill, "Where Is Dopamine and how do Immune Cells See it?: Dopamine-Mediated Immune Cell Function in Health and Disease," *Journal of Neuroimmune Pharmacology*, vol. 15, no. 1. pp. 114–164, 2020.

[148] N. F. Atta, A. Galal, and D. M. El-Said, "Novel Design of a Layered Electrochemical Dopamine Sensor in Real Samples Based on Gold Nanoparticles/β-Cyclodextrin/Nafion-Modified Gold Electrode," *ACS Omega*, vol. 4, no. 19, pp. 17947–17955, 2019.

[149] G. A. Goossens, M. Vrebos, I. De Wever, and M. Stas, "Vacutainer® filling time through subcutaneous venous access devices," *J. Vasc. Access*, vol. 5, no. 4, pp. 154–160, 2004.

[150] M. Albalate *et al.*, "Is it useful to increase dialysate flow rate to improve the delivered Kt?," *BMC Nephrol.*, vol. 16, no. 1, pp. 1–6, 2015.

[151] D. R. M. Hassell, F. M. Van der Sande, J. P. Kooman, J. P. Tordoir, and K. M. L. Leunissen, "Optimizing dialysis dose by increasing blood flow rate in patients with reduced vascular-access flow rate," *Am. J. Kidney Dis.*, vol. 38, no. 5, pp. 948–955, 2001.